A cooler Penning trap to cool highly charged radioactive ions and mass measurement of ^{24}Al

by

Usman Chowdhury

A thesis submitted to the Faculty of Graduate Studies of
The University of Manitoba
in partial fulfillment of the requirements for the degree of

DOCTOR OF PHILOSOPHY

Department of Physics and Astronomy

University of Manitoba

Winnipeg

Abstract

Penning trap mass spectrometry (PTMS) can be used to test the Standard Model (SM) and to answer the questions related to the origin and abundance of the elements in the universe. There are several facilities worldwide specialized in PTMS and some of them can measure the masses of isotopes with half-lives in the range of milliseconds. TRIUMF's ion trap for atomic and nuclear science (TITAN) is one such facility. In mass measurement the precision is linearly proportional to the charge state of the ion of interest. To increase the charge state, ions are charge-bred using an electron beam ion trap (EBIT) at TITAN. However, the charge breeding process introduces an energy spread among the ions which adversely affects the precision of the mass measurement. To overcome this problem a cooler Penning trap (CPET) was designed, assembled and is now being tested off-line. This thesis presents the first systematic test results of CPET. We also present the result of the first Penning trap mass measurement of the isotope ^{24}Al, which is five times more precise than the previous atomic mass evaluation (AME2012) value. The precise and accurate mass of ^{24}Al is important for both astrophysics and for test of the standard model (SM). The resonance energy (E_r) calculated for the ^{23}Mg$(p,\gamma)^{24}$Al reaction using the ground state mass of ^{24}Al reported in this thesis shows a 2σ deviation from the direct measurement. On the other hand, tests of the SM by evaluating ft values using isospin $T = 1$ nuclides have reached a high precision level. Effort is now shifting towards the $T = 2$ nuclides, which are far from stability compared to their $T = 1$ counterparts. For this reason, the ground state masses of $T = 2$ nuclides and of their decay products are required to be known with high precision. ^{24}Al is the daughter of one such nucleus, ^{24}Si. The ground state mass of ^{24}Al reported in this thesis will be useful to test the SM.

Preface

Most of the experiments in modern physics require multi-disciplinary expertise which naturally involves a large number of people. This is particularly true in the case of the physics of radioisotopes. Experiments at TITAN are no exception. The CPET project enjoyed the support from the TRIUMF machine shop whenever needed. The electronics and data acquisition groups were instrumental in the development of the control system. Also, the TITAN team members were always there to share their experience and skill. In this large team-effort my major contributions could be summarized as follows:

I was leading the CPET project since spring 2012. This includes various developments, modifications, the planning and execution of systematic tests, performing experiments, and data analysis. As part of my PhD project I have:

- Developed the baking system of CPET which is very important to ensure a high vacuum. Without a satisfactory (in the range of 10^{-10} Torr) level of vacuum, the highly-charged ions (HCIs) will undergo recombination which will render them unusable for mass measurement. The pumping rate of the CPET chamber is increased by activating the non-evaporable getter (NEG) coating on it. Due to severe space constraints in the magnet bore, I decided to follow a unconventional insulation and baking method for the activation of the NEG. The effectiveness of that method was tested and is reported in this thesis.

- Developed the control system of CPET. This involves the control of the high voltage (HV) power supplies, detectors and detector position control, vacuum and temperature monitor and the crucial interlock to save the system in case of any vacuum failure or pressure burst

inside the vacuum. The CPET control system has also reduced the effort of preparing and tuning the system significantly. It is facilitating successful off-line tests to date.

- Calculated and implemented the detector requirements and their positions. The position, number and size of the detectors are very important. Although it is desirable to have as many detectors as possible in the system, the space and economic constraints require a careful calculation and planning to optimize this demand. The initial design and plan of detector had a few limitations. By performing systematic tests, I was able to propose the best possible position and specifications of the detectors, and successfully implemented the changes.

- Successfully confined dense electron plasmas with large numbers of electrons for more than 2 minutes. While the HCI cooling process should not take more than few hundred milliseconds, the simulations show that the denser and larger the electron number, the faster the cooling process. The demonstration of dense ($\approx 10^{14}$ m^{-3}) electron plasma accumulation with up to $\approx 10^8$ electrons is a very promising sign and shows that the progress is in the right direction. Being able to confine the plasma for longer times is very helpful as this indicates that many cooling cycles can be completed without reloading the trap with electrons. This will have a positive impact on precision of the mass measurement.

- During the offline tests I observed the damping of the $m = 1$ plasma oscillation mode. The existence of this mode can have a negative influence on the effectiveness of the cooling. As a result, it is important that this mode damps away before ions are brought in for cooling. Careful analysis showed that we are observing the damping in a new parameter regime. A manuscript reporting these findings is in preparation.

We have routinely reported our progress on the CPET project to the scientific community through a number of publications. The following two conference proceedings contain the most up-to-date status of the CPET project:

- U. Chowdhury et al. A Cooler Penning Trap to cool highly-charged and short-lived isotopes at TITAN, Proceedings of COOL2013, 206-209 (2013).

- U. Chowdhury et al. A cooler Penning trap for the TITAN mass measurement facility, AIP Conference Proceedings 1640, 120-123 (2015).

Besides my contribution and responsibilities in the CPET project, I was routinely contributing to the TITAN mass measurement experiments. Some of my contributions in TITAN mass measurement experiments are:

- I was involved in preparing the system for the experiments since fall 2010 and have been doing the online data analysis during the beam times since 2012.

- I have done the online and also the final analysis of the mass measurement of the ^{24}Al isotope, and prepared the draft for the article which is a part of this thesis. This work on ^{24}Al was published in Physical Review C: U. Chowdhury et al., *First direct mass measurement of the neutron-deficient nucleus* ^{24}*Al*, Physical Review C 92, 045803 (2015).

Contents

Abstract i

Preface ii

List of Tables ix

List of Figures x

Acknowledgments xv

1 Introduction 1

2 Ion traps and the TITAN experimental facility 5

2.1 Penning traps 6

2.1.1 Ion motion inside the Penning trap 9

2.2 TRIUMF's ion trap for atomic and nuclear science (TITAN) 11

2.2.1 The Radio-Frequency Quadrupole (RFQ) Cooler and Buncher 12

2.2.2 Electron Beam Ion Trap (EBIT) 13

2.2.3 TITAN's Measurement Penning trap (MPET) 15

3 Cooling of charged particles 19

3.1 Ion temperature 21

3.2 Cooling of ions 23

3.2.1 Resistive cooling . . . 24
3.2.2 Sympathetic cooling . . . 25
3.2.3 Buffer-gas cooling . . . 26
3.2.4 Sideband cooling by buffer gas . . . 26
3.2.5 Sympathetic cooling by means of charged particles . . . 27
3.2.6 Rotating wall compression . . . 28
3.2.7 Stochastic cooling . . . 29
3.2.8 Evaporative cooling . . . 30
3.2.9 Optical cooling . . . 32
3.2.10 Doppler cooling . . . 33
3.2.11 Sub-Doppler cooling . . . 34
3.2.12 Cooling with a polarization gradient . . . 36
3.3 Conclusion . . . 37

4 TITAN's cooler Penning trap **39**
4.1 Introduction . . . 39
4.2 Sympathetic cooling and the working principles of CPET . . . 40
4.3 Trap structure . . . 43
4.3.1 Alignment . . . 44
4.4 Electron and ion sources . . . 47
4.5 CPET ultra-high vacuum and the baking facility . . . 48
4.6 Detectors . . . 52
4.7 CPET control system . . . 53
4.7.1 Programmable Pulse Generator . . . 53
4.7.2 Voltage control, system monitor and interlock . . . 54

5 Systematic studies of CPET **58**
5.1 Electron source and transmission efficiency . . . 58

5.2 CPET detectors and the calibration . . . 64
5.2.1 Micro channel plates . . . 64
5.2.2 Imaging devices: phosphor screen and CCD camera . . . 65
5.2.3 Faraday cup and Phosphor screen and their calibration . . . 65
5.3 Choosing the detector position and size . . . 68
5.3.1 CPET detector position and size comparison with other facilities . . . 73
5.4 Possible improvement of the detection method and detectors . . . 75
5.4.1 Short-term solution for the offline tests . . . 76
5.4.2 Long term solution for the online-operation . . . 80
5.5 Electron plasma requirements for CPET . . . 82
5.6 Systematic tests of CPET . . . 82
5.6.1 Loading the trap with electrons . . . 83
5.6.2 Trapping for different electron current . . . 85
5.6.3 Electron trapping for different potential depths . . . 85
5.6.4 Analysis of CPET electron plasma properties . . . 86
5.6.5 Electron number for varying trapping time . . . 89
5.6.6 Debye length of the CPET plasma . . . 90
5.6.7 Plasma intensity for varying trapping time . . . 91
5.7 Conclusion . . . 92

6 Damping of the $m = 1$ plasma oscillation mode **94**
6.1 $m = 1$ mode of plasma oscillation . . . 95
6.2 Setup details . . . 99
6.3 Data analysis and results . . . 101
6.4 Summary . . . 103

7 Mass measurement of ^{24}Al **104**
7.1 Astrophysical importance of ^{24}Al . . . 105

7.2 The standard model importance of ^{24}Al 108
7.3 Experimental procedure 111
7.4 ^{24}Al mass measurement and result 112
7.5 The effect of the ^{24}Al mass on the ^{23}Mg$(p,\gamma)^{24}$Al reaction rate 114
7.6 Conclusion 117

8 Summary and outlook **118**

Bibliography **121**

A Standard tune for CPET **138**

A.1 Potential setting 138
A.2 Programmable Pulse Generator (PPG) setting 139
A.3 Camera setting 140

List of Tables

5.1 Area covered by detectors at different facilities. 74

6.1 Times represent the duration of trapping in the trap. 102

7.1 Resonance energy derivation methods for the ^{23}Mg(p,γ) ^{24}Al reaction. 108

7.2 Summary of the ^{24}Al mass measurement. 115

A.1 CPET tune values. The negative values are highlighted with green and the positives with red. 139

A.2 Programmable Pulse Generator (PPG) setting details. At present, three major components are controlled by the PPG for precision timing. 140

List of Figures

2.1 The two most common types of ion traps. 6

2.2 Two categories of Penning traps. 7

2.3 3D saddle-shaped qudrupolar electric potential field inside a Penning trap. 8

2.4 A hyperbolic Penning trap and the ion trajectory inside the trap. 10

2.5 The TITAN beam-line and all the currently operational traps. 12

2.6 Schematics of ISAC experimental halls. 13

2.7 The beamline of ISAC facility and the target station. 14

2.8 Schematics of trapping in the RFQ. 15

2.9 Schematic of EBIT electrodes and a cartoon of the axial and radial potential. 16

2.10 Time of flight spectrum of ions after boosting the charge state in the EBIT. 17

3.1 Mass dependence of the Maxwell-Boltzmann velocity distribution for different mass numbers (A). 21

3.2 Temperature scale of different experiments. 23

3.3 Resistive cooling methods for ions in a trap. 24

3.4 Coolant and ions in a MRT. 28

3.5 Rotating wall cooling is performed by means segmented electrodes. 29

3.6 Two different methods of stochastic cooling. 30

3.7 Evaporative cooling. 31

3.8 Laser cooling. 33

3.9 Sideband cooling of ions in a trap with harmonic potential. 35
3.10 Laser cooling taking advantage of the polarization gradient. 36
3.11 Sisyphus cooling. 37

4.1 Electron cooling of the highly-charged ions. 40
4.2 Simulation results for electron cooling. 42
4.3 Left: The trap assembly with rods and ceramic support parts. Right: Three types of gold plated electrodes. 43
4.4 Dipole cleaning of the ions. 44
4.5 CPET offline test layout. 45
4.6 Extrapolation of the magnetic axis to both faces of the magnet bore from the half magnetic field values. 46
4.8 MPET alignment procedure. 46
4.7 Extrapolated values from the uniform and strong field region to the magnet bore openings. 47
4.9 CPET electron source and ion source. 48
4.10 Ceramic blanket on CPET. 49
4.11 CPET's flexible heaters. 50
4.12 Offline baking setup for CPET. 51
4.13 Temperatures on the magnet bore and on the trap housing. 51
4.14 Partial pressures before and after baking. A residual gas analyzer (RGA) was used to study the partial pressures of individual gas species. 52
4.15 CPET control system schematic. 53
4.16 CPET PPG cycles 54
4.17 A LabVIEW program sets the electrode potentials, which are interlocked with the vacuum readout. 55
4.18 Major components of CPET DAQ and control system. 56

5.1 Magnetic field gradient responsible for mirror effect. 59
5.2 LabView program was used to condition the FET and to measure the transmission efficiency. 60
5.3 A LabView program was used to condition the FET. 61
5.4 Transmission efficiency test of CPET with FET. 62
5.5 Images of field emission tips (FETs). 62
5.6 A CCD image of the electron pulse direct from the source. 63
5.7 Transmission efficiency test result. 64
5.8 Area generated by the signal of DC pulses of different time length. 66
5.9 Amplifier circuit for electron number detection. 67
5.10 Calibration graph. 67
5.11 Magnetic field on-axis and the corresponding diameter of a plasma of unit radius. . 69
5.12 Effect of plasma expansion for a perfect trap alignment. 69
5.13 Effect of plasma expansion for an imperfect trap alignment. 70
5.14 SIMION simulations for plasma detection. 70
5.15 When triggered, the diocotron mode drives the plasma away from the trap axis. . . 71
5.16 A plasma of 0.1 mm diameter after extraction at the detector of 25 mm diameter. . 72
5.17 High voltage and dipole frequency coupling electronics. 72
5.18 Success rate of detection for different trapping times with the MCP at its original position. 73
5.19 Effective detector area comparison. 75
5.20 CPET phosphor screen/FC. 76
5.21 First proof that $m = 1$ mode of plasma oscillation is in action. 77
5.22 20 seconds to 2 min 10 second plasma in CPET. 78
5.23 Difference between images produced by blocking and not blocking the light from the electron source using the electron injection-end FC. 78

5.24 Plasma image for 1 second confinement before and after replacing the aluminium holder with a Macor holder. 79
5.25 Phosphor screen on Macor holder and shielded biasing cable. 80
5.26 Noise and signal after phosphor screen isolation. 80
5.27 Effective detector area if the MCP is moved to the entrance (closer to the trap) of the feed-through-section. 81
5.28 Different loading schemes and the gate potentials. 84
5.29 Trapped electron number as a function of filament current. 85
5.30 Trapped electron number as a function of the trap depth (V_T-V_S). 86
5.31 2D projection of the radial intensity profile of the electron plasma for trapping times of 1 to 5 seconds. 87
5.32 Intensity slices generated by taking the radial values from Fig. (5.31). 87
5.33 A spheroid fit based on the intensity slice. 88
5.34 Phosphor screen size is related to the pixel width using this CCD image. 88
5.35 A circle is fitted by enhancing (5x) the CCD image to find the full radius of the plasma. 89
5.36 Electron number as a function of time in CPET. 90
5.37 The peak intensity as a function of time. 91

6.1 Oscillation modes of plasma in a Penning trap. 95
6.2 Two possible ways of perturbative fields generated by electron plasma. 98
6.3 Trap potential scheme. During loading the entrance gate is kept at -850V. During extraction the extraction gate is switched to 0 V or to a small positive potential. . . 100
6.4 Damping of the $m = 1$ plasma mode in CPET 100
6.5 Electron number and individual plasma radius as a function of time. 101
6.6 Momentum study and the $m = 1$ diocotron mode damping in CPET. 102

7.1 Isotopes in the Ne-Na (orange) and Mg-Al (purple) cycle. 106

7.2 Superallowed beta decay candidates. $T = 1$ and $T = 2$ nuclide. 109
7.3 Resonances for ^{23}Na and ^{24}Al measurements. 111
7.4 IG-LIS ion source schematic. 112
7.5 ^{39}K measurements for accuracy check. 113
7.6 ^{24}Al measurements. 114
7.7 Proton separation energy. 115
7.8 Comparison of the resonance value. 116

A.1 CPET beamline. Elements on the left of phosphor screens are not used as we need elements only up to the phosphor screen for plasma loading, trapping and detection cycles. 138
A.2 PPG setting for CPET. 140
A.3 CCD camera trigger and other settings for optimal image quality for recording electron plasma spots. 141

Acknowledgments

All praise is due to Allah, the almighty. First and foremost I thank Allah the almighty for enabling me to complete my research work and this thesis. Alhamdulillah! Research in general, and particularly in the field of nuclear physics, is hardly performed by any single individual. Most of the time it requires a team effort. I was blessed by Allah to have large number of excellent people as my colleagues, friends and family without whom this work would not be possible. The full list long and is impossible to complete. I owe my gratitude to all those people who have made this dissertation possible.

I am extremely thankful to Dr. Gerald Gwinner for supervising my work and his continuous support. I think everyone who came in touch with Gerald Gwinner, appreciates his knowledge and dedication to science. His friendly supervision and encouragement in difficult times made it easy to continue my work. Beside research, we had a lot of debate on religion, politics, culture and sports that I will miss.

Our team leader Dr. Jens Dilling has always lead the group in an excellent manner. My sincere thanks to Jens Dilling for supervising in a way that motivated all the group members to give their best effort to advance the projects. He took time to analyze and support any new idea that I wanted to implement. He encouraged me with his support to go for the conferences in different places in the world from where I have learned a lot.

Experimental physics is an expensive field of research. We are always pushing materials and technology to their limits to find something new or to develop some instrument that will help us better understand the nature. In this epic journey, sometimes we fail, sometimes the machine. We

try to minimize the expenditure but for the ongoing quest, it's necessary to learn from observation and mistakes. It was a wonderful opportunity for which I thank each and every Canadian for trusting us with their tax money.

There are a lot of technical details that are never published, or discussed that are taken care of by some very skilled people. Without the effort of a number of skilled technologists and technicians, our experiments would not be possible. TRIUMF has a group of highly skilled staffs who are instrumental to the success of all the experiments. I am grateful to all the TRIUMF staffs including Suzannah Deviel, Daryl Bishop, Hubert Hui, Leonid Kurchaninov, Alex Sorokin and the machinists in the machine shop who were extremely helpful. In TITAN, Mel was always the lead technologist during my program. He has known the TITAN system from the beginning, and without his skill it would not be possible to put all the sophisticated elements together. Thanks a lot Melvin Good.

Dr. Matthew Pearson is someone who was harassed probably more than anybody else outside the group. He patiently listened to my problems and extended his helping hand whenever he could. Whenever the work extended to weekends or evening, he was the person to approach for discussion and suggestions. A special thanks to Dr. Corina Andreoiu for her kind help on managing and expediting the machining work of the first in-drift-tube phosphors screen which was a very important step on our plasma detection.

I am thankful to all TITAN members with whom I had the pleasure to work with. Everyone became very good friend within a few days while maintaining a high level of professionalism. Among them are Dr. Brad Schultz, Dr. Aaron Gallant, Shail Sheeraji, Dr. Stephan Ettenauer, Dr. Ernesto Mane, Dr. Martin Simon, Dr. Ankur Choudhuri and Dr. Annika Lennerz. I cannot be redundant on acknowledging the help from Dr. Ania Kwiatkowski, Dr. Kyle Leach, Dr. Brad Barquest, and Brian Kootte. Their timely comments and feedback on my thesis were very important for me to reduce the typos, make it well organized, and to make sure each chapter, section and subsections were meaningful, and contained enough information and references. I owe them a lot. I would like to thank Dr. Ania Kwiatkowski particularly for her support on taking the last set of

data which gave us a very good understanding of CPET. A special thanks to Daniel Lasker, who joined TITAN when I was wrapping up my research, and did some very important modification which facilitated the electron number detection.

The quality of initial data from one of our detectors (phosphor screen) was not so good due to high noise and strong background. I owe to our family friend Mushfiqur Rouf Nasa, a Ph.D. student in the department of computer science at UBC, for his time and effort in making the primary data usable by showing me a robust image processing technique.

I was also blessed with an extraordinary family. My father who would be most happy on my completion is no more. However, my mother, who is the chief architect of our family is someone without whom me and my siblings would not be able to continue in the extremely competitive academic environment of Bangladesh, where I was born. Thanks a lot amma! She always supported us and allowed us to chase our dreams as we wished, when most parents were trying to convince their children to study the applied sciences. I must thank my uncle Syed Anwar Hussein from whom I first got the book of Arthur Beiser on Modern Physics. Without reading this book, probably I would not pursue to study physics. My second uncle Dr. Syed Miftah Uddin, my two sisters Baby Akter Chowdhury and Musharrafunnesa Chowdhury, and my brother Enaitur Rahman Chowdhury have encouraged me to stay focused and took care of my mother which made it easy for me to continue my research. My sincere gratitude and thanks to all of them for their unconditional support.

Finally, thanks to my wife Suhana who has made a lot of sacrifice during my writeup, especially after the birth of our son Abdullah. I can not thank her enough. Without her support it would have been very difficult to conclude this work.

Dedicated to my parents

Chapter 1

Introduction

The knowledge about elementary particles and their interactions is of great importance for our understanding of the nature. With the advancement of science and especially the development of higher energy accelerators, from the early twentieth century on, numerous elementary particles were discovered [1]. By the end of the twentieth century, the number of such particles reached a staggering 61 [1, 2], extending the known particles far beyond the well known electron, proton and neutron that had been known to exist at that time. Once many of them were discovered, a theory to explain the interactions between them and categorizing them into appropriate groups became necessary. In addition, theoretical physicists were able to find that some of the forces that were earlier thought to be independent and different from each other are in reality different manifestations of a single force. For example, earlier, James Clerk Maxwell was able to show that electricity and magnetism are two different manifestations of the same electromagnetic force, or field [3]. This gave an indication of the existence of a unified theory for the fundamental forces. Hence, with the newer discoveries, the demand for a new theory was enormous. It is this time, when scientists all over the world contributed to developing the theory which is now known as the standard model (SM). The SM is largely based on the mathematics of group theory [4]. The existence and breakdown of different group-symmetries in the SM requires the existence of the constituent particles and their interactions [5]. So far, the SM has been able to systematically categorize and predict the

properties of most of the known fundamental particles with few exceptions. In many cases the SM predicted the existence of new particles that are required by the gauge symmetry and were discovered later [2]. The most prominent of them is the Higgs boson [6, 7]. Although the SM is to date the most successful theory physicists have, the weaknesses of this theory have started to emerge. It was widely accepted that besides the failure to include gravity, the SM gives a complete theory for elementary particles and their interactions. However, experiments found that the neutrinos have non-zero masses, which is not acceptable within the current framework of the SM. The SM also does not explain the existence of the large amount of cold dark-matter (CDM) [8] in the universe. While some of the limitations of the SM are evident from the theory itself (i.e., absence of gravity, failure to incorporate the CDM etc.), some experiments can test the legitimacy of the SM by testing the predictions the SM offers. Unitarity of the Cabbibo-Kobayashi-Maskawa (CKM) quark mixing matrix, and the conserved vector current (CVC) hypothesis are two such predictions that can be tested through nuclear physics experiments.

In a different realm, astrophysicists and cosmologists are trying to understand the origin of different elements in the universe. They found clear evidence that stars and other celestial objects have different ratios of known elements. Also, there is more matter in our visible universe than anti-matter. It is important to know why such an imbalance is observed in nature. Besides being a question of fundamental human knowledge, this question is related to the very existence of our earth and hence to the origin of the human species. Nuclear reactions in stars and supernovae form a number of reaction cycles such as the carbon-nitrogen-oxygen (CNO) and sodium-magnesium (NaMg) cycles. Formation of elements and their isotopes depends on the binding energy of the nucleus. Almost all the elements we have around us in daily life are stable isotopes with halflives many orders of magnitude higher than that of the universe ($\sim 14 \times 10^9$ years). All the stable isotopes have specific numbers of protons and neutrons. Generally, the larger the difference between the numbers of protons and neutrons is, the more unstable the isotope. The origin of stable nuclides in the universe is not always a straightforward one. Most of the time the isotope generation follows a complex reaction network. The reactions themselves do not have any preference towards

the stable nuclides. However, the reaction networks produce radioactive nuclides which eventually decay towards the region of stability. The intermediate steps between a stable nuclide and a so-called seed nuclide are full of other radioactive nuclides, and the origin and abundance of any element depends largely on which reaction path they follow. With the development of new and powerful accelerators, it is now possible to produce a large number of short-lived isotopes and perform nuclear experiments that can help us understand the origin and abundance of the elements in the universe.

The atomic nucleus consists of two kinds of particles, protons and neutrons. Being the fundamental constituents of a nucleus, they are together known as nucleons. Nuclear mass is a manifestation of all the underlying interactions between its constituent particles, including the quarks and gluons that are the main ingredients of the nucleons themselves. As a result, the mass of an atomic nucleus can provide an insight into the physical interactions between the particles involved, as well as the intrinsic properties of them. From the above discussion it is clear that our knowledge of the origin of the elements, as well as the SM can be tested by means of radioactive nuclides. As mentioned earlier, most elements around us are stable. The challenge is then the availability of those isotopes that are short-lived. Halflives of the scientifically interesting isotopes for the experiments vary over a wide range. In addition, there is no technology available that can produce only one isotope at a time. In almost all cases, a large number of isotopes is produced. Producing those isotopes, and then separating a particular species requires very precise state-of-the-art technology. This requires isotope production facilities which are either nuclear reactors or accelerator-based research facilities such as ISOLDE at CERN, ISAC at TRIUMF, and ATLAS at Argonne National Laboratory.

Motivated by the importance of the precision mass measurement of short-lived isotopes, the TITAN experimental facility was established at TRIUMF in Vancouver, Canada. TITAN has so far successfully measured the masses of a number of isotopes with high importance in testing the SM [9, 10], nuclear models [11–13] and astrophysics [14]. A unique feature of the TITAN facility is the charge-breeding capability. This process can increase the precision of the mass measurement. The

charge boosting is done by bombarding the ions of interest with an intense electron beam inside an electron beam ion trap (EBIT). However, this process of charge breeding causes a large energy spread among ions which eventually adversely affects the mass measurement and partially reduces the benefits we would get from the charge-bred ions. To reduce the energy spread introduced during the charge breeding process, the cooler Penning trap (CPET) project was initiated.

In this thesis we discuss two major contributions. The development of CPET is the primary focus of this thesis. Hence, at first, we discuss the importance of ion cooling and report the systematic tests of CPET, which is currently being developed to reduce the energy spread introduced by the EBIT. Then we report the first Penning trap mass measurement of ^{24}Al and its importance in astrophysics and on testing the SM.

In the 2nd chapter we discuss the basics of ion traps and give a brief introduction of TITAN and its existing traps. The in-depth discussion and details of TITAN are available from numerous sources in the form of peer reviewed journals. As a result, this thesis discusses only the major components and their functions briefly.

CPET will be used to cool the charge-bred, highly-charged ions (HCIs), and we present a compact but broad discussion of ion cooling in the 3rd chapter. Some of the cooling methods discussed are used for neutral atoms as well. The discussion of neutral atoms appears because cold, neutral atoms are sometimes used to cool the ions.

A detailed description and working principles of CPET are discussed in chapter 4. In chapter 5 we give the details of the offline tests we performed. During our offline tests we observed the damping of the $m = 1$ diocotron plasma mode [15, 16]. This mode and its damping that we observed are presented in chapter 6. Our understanding is that we observed this damping in a new range of parameters.

Chapter 7 gives the details of the mass measurement of ^{24}Al [17] with the help of newly developed ion guide-laser ion source (IG-LIS) [18]. TITAN is a very well known experimental facility and the details are available from a number of sources, we have kept chapter 7 very compact.

We conclude the thesis with a summary and outlook.

Chapter 2

Ion traps and the TITAN experimental facility

Prior to the invention of ion and atom traps our knowledge of the microscopic particles was based on the statistical average of a system of a large number of particles. Although Rutherford's gold foil experiment [19] and the Davisson-Germer experiment [20] with electrons were giving some insight into individual particles, they would in general involve a large number of particles and an average outcome. As a result, the physical knowledge would describe the ensemble of the particles instead of individual particles or a small group of them. Low temperature study of single atoms and ions, mass spectrometry, anti-matter research, plasma physics, and most recently development of quantum computing, inevitably require the ions or atoms to be thermally isolated and suspended in space by means of electromagnetic fields instead of solid material walls. Through the revolutionary work of W. Paul, the scientific community first saw the suspension of ions in space by means of RF electric fields (the Paul trap) [21]. This facilitated the manipulation and observation of microscopic properties directly, with very little to no perturbation of the system. At about the same time, scientists also developed Penning traps, where the ions are radially confined by means of a magnetic field [22]. The basic principle of trapping is to apply a restoring force that prevents the ions from leaving the trap.

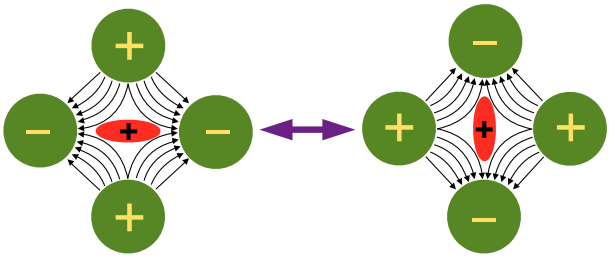

(a) Electrodes and field in Paul trap with alteration.

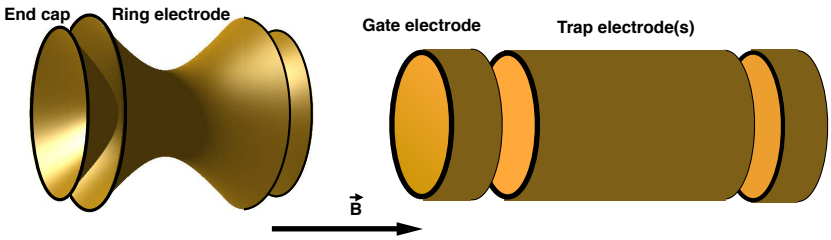

(b) Hyperbolic (left) and cylindrical (right) Penning traps.

Figure 2.1: The two most common types of ion traps. Ions are confined radially by means of an oscillating electric field, which is called a Paul trap, or by means of a magnetic field, which is called a Penning trap. Axially the ions are confined by means of static electric fields in both types of traps [23]. Whatever the trap geometry is, the principle of trapping is simple, applying a restoring force that pushes the particle back towards the centre of the trap whenever it wants to escape.

Fig. (2.1) shows the two most common types of ion traps. All the work reported in this thesis is related to Penning traps. Hence, in the next section we will discuss the working principles of a Penning trap.

2.1 Penning traps

Penning traps use a homogenous magnetic and a quadrupolar electric field to confine the charged particles in space [24]. Depending on their use, Penning traps can be made with two different geometries; the hyperbolic Penning trap and the cylindrical Penning trap. Fig. (2.2) shows both kinds of Penning traps with their corresponding characteristic parameters r_o and z_0. The hyperbolic Penning traps have electrodes which are hyperboloids of revolution. The ring electrode is a hyperboloid of revolution of one sheet while the end caps are hyperboloids of revolution of two sheets. Cylindrical Penning traps consist of two gate electrodes which are equivalent to the end caps of a

hyperbolic Penning trap, and there are one or more cylindrical ring electrodes between the two gate electrodes (the latter case is referred to as a multi-ring trap or MRT). In an MRT the trapping region can be adjusted depending on the use, and more than one species of charged particles with same or opposite charges can be trapped. For a hyperbolic Penning trap both of the characteristic parameters remain the same while in a cylindrical Penning trap z_0 changes with the adjustment of the trapping region. Irrespective to the geometry, the fundamental trapping mechanism for both types

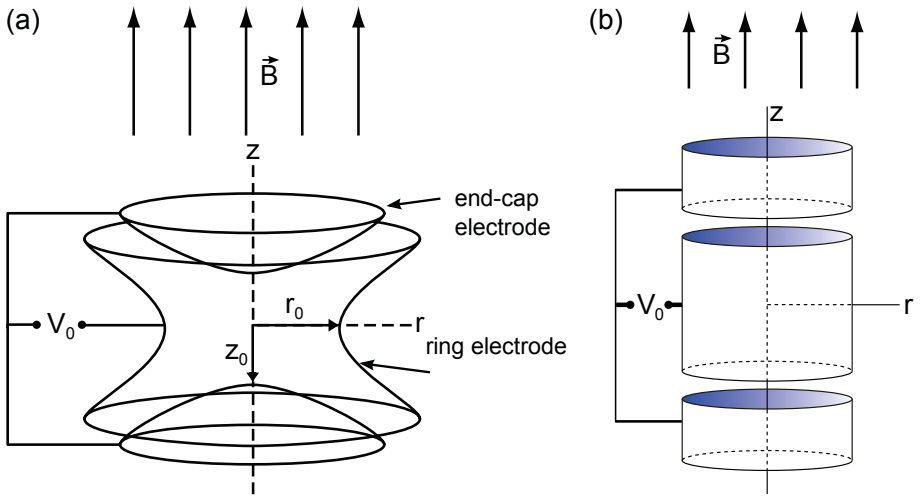

Figure 2.2: Two categories of Penning traps. A same-sign potential is applied on the end-caps and on the ring electrodes. The traps are housed in a magnetic field pointing along the axis of the trap. **(a)** A hyperbolic Penning trap is made of three basic components; two end caps which are two hyperboloid of revolution of two sheets, and a ring electrode which is a hyperboloid of revolution of one sheet (left). **(b)** The cylindrical Penning trap consists of cylindrical ring electrodes only. The same electrodes can function as the end-caps. Figure from [25].

of trap are the same. In a Penning trap the magnetic and electrical fields are superimposed and the resultant force on the ion is a Lorentz force ($F_{\text{Lorentz}} = F_B + F_E$). The homogenous strong magnetic field ($\vec{B}$) confines the particles of charge q and velocity $\vec{v}$ radially by means of the centripetal force ($\vec{F_B} = q\vec{v} \times \vec{B}$) giving the ions a circular cyclotron motion with a frequency $\omega_c = qB/m$, where m is the mass of the ion. The axial confinement is achieved by the static electric fields (V) which exert a restoring force $\vec{F_E} = -q\vec{\nabla}V$ on the ions and push them towards the centre of the trap. The two forces discussed above are geometry-independent general relations governing the interaction

between charged particle and a field of any shape and magnitude. To utilize these two forces to achieve the ion confinement, the geometry of the electrostatic potential has to be selected carefully. The most convenient electrostatic potential that can trap ions axially is quadrupolar [26], and of the form:

$$V = \frac{V_0(\alpha x^2 + \beta y^2 + \gamma z^2)}{r_0^2}, \tag{2.1}$$

where x, y, and z are the three-dimensional coordinates of the ion, α, β and γ are the constants that are derived from the applied potential, and r_0 is the characteristic trap size mentioned above. Although the purpose of the electrostatic field is to confine the particle along the z-axis, the x and y components enter the field to make sure that the Laplace equation ($\nabla^2 = 0$) is satisfied [27]. A typical spatial profile of such fields is shown in Fig. (2.3).

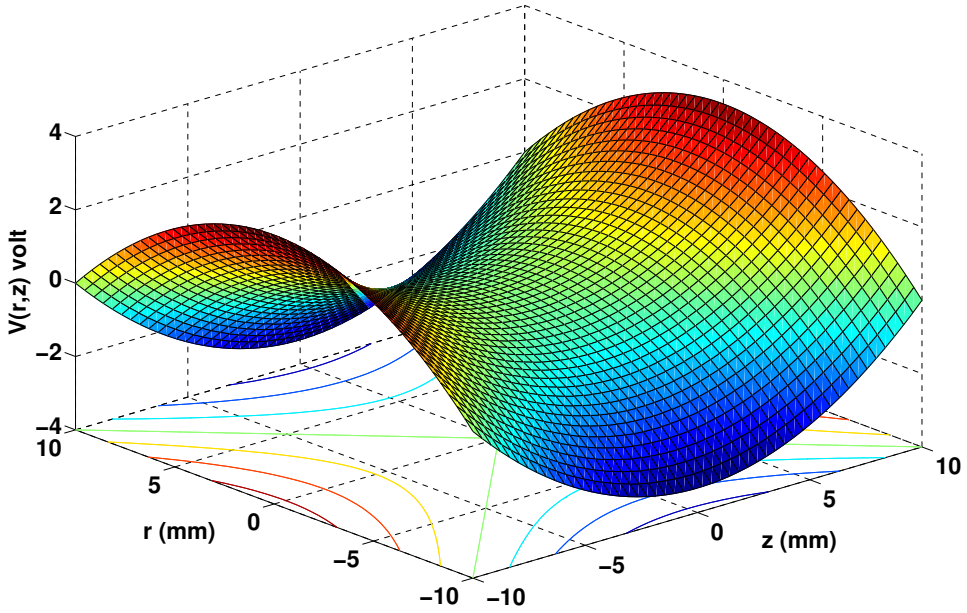

Figure 2.3: 3D saddle-shaped qudrupolar electric potential field inside a Penning trap. There is no local minimum except at the boundaries. For convenience we have switched to a cylindrical coordinate system where $x^2 + y^2 = r^2$. Figure generated using the relation 2.1, with $r = 10 = z$.

2.1.1 Ion motion inside the Penning trap

The ion motion inside a Penning trap is governed by the homogenous magnetic and the quadrupolar electric field. For a particular Penning trap Eq. (2.1) can be rewritten as:

$$V(r,z) = \frac{V_0}{2d_0^2}\left(z^2 - \frac{r^2}{2}\right), \tag{2.2}$$

where the characteristic trap dimension d_0 is given by:

$$d_0^2 = \frac{1}{2}\left(z_0^2 + \frac{r_0^2}{2}\right). \tag{2.3}$$

Now, the motion for a charged particle inside the Penning trap can be completely described by the following relations:

$$\frac{d^2x}{dt^2} = \omega_c \frac{dy}{dt} + \frac{1}{2}\omega_z^2 x \tag{2.4a}$$

$$\frac{d^2y}{dt^2} = -\omega_c \frac{dx}{dt} + \frac{1}{2}\omega_z^2 y \tag{2.4b}$$

$$\frac{d^2z}{dt^2} = -\omega_z^2 z. \tag{2.4c}$$

Here ω_z, the axial frequency is completely independent of the radial motion. This decoupled frequency is given by:

$$\omega_z = \sqrt{\frac{qV_0}{md_0^2}}. \tag{2.5}$$

The radial parts are solved to yield a solution in terms of two eigenfrequencies:

$$\omega_\pm = \frac{\omega_c}{2} \pm \sqrt{\frac{\omega_c^2}{4} - \frac{\omega_z^2}{2}}. \tag{2.6}$$

These two frequencies are called the magnetron (ω_-) and reduced cyclotron (ω_+) frequencies. Fig. (2.4) shows a hyperbolic Penning trap and the three ion motions. It can be shown that the three frequencies are related by:

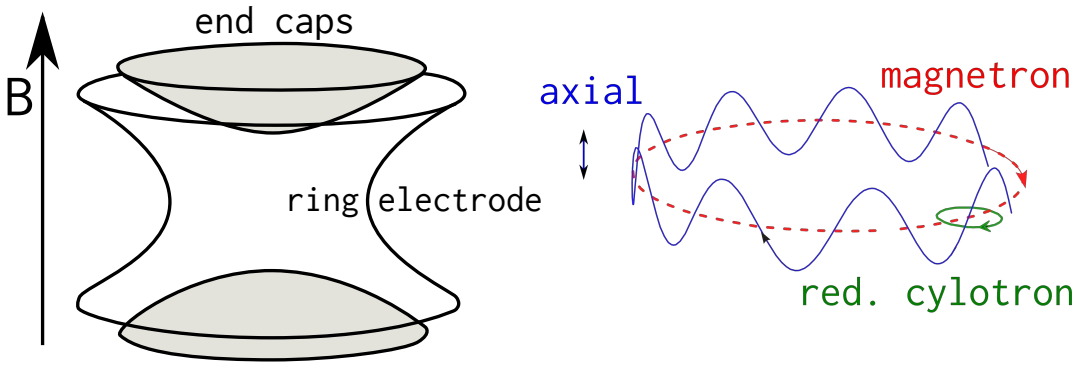

Figure 2.4: A hyperbolic Penning trap and the ion trajectory inside the trap. The uniform magnetic field and the quadratic electric field exert a Lorentz force on the ion and modify the motion and give rise to the three Eigen-motions (right).

$$\omega_c = \omega_+ + \omega_- \tag{2.7a}$$

$$\omega_c^2 = \omega_+^2 + \omega_-^2 + \omega_z^2 \tag{2.7b}$$

$$2\omega_+\omega_- = -\omega_z^2. \tag{2.7c}$$

The hyperbolic shape of the electrodes produces the most uniformly quadratic electric field achievable [28]. The electrodes are machined to the best possible tolerance to reduce the field imperfections. However, a practical Penning trap is far from the ideal one. The entry and exit holes for the ions causes a field distortion which is corrected by a combination of compensation electrodes. A careful alignment is also performed for the $\vec{E}$ and $\vec{B}$ fields. Hyperbolic Penning traps are used for precision nuclear mass spectrometry and the careful machining and alignment of trap electrodes reduce the systematic errors significantly. Usually, a cylindrical Penning trap is not used for precision measurement (for example, mass measurement of very short-lived isotopes) and thus the requirement for the high-quality quadrupole electric field is not very strict. However, naturally, the more precise the alignment and the field of the trap is, the better the particle confinement will be. Cylindrical Penning traps are widely used for non-neutral plasma physics research [29] and also to cool antiprotons at CERN [30]. Efforts are also underway to cool highly-charged-ions

(HCIs) where an electron plasma will be used to reduce the energy-spread [31, 32]. TITAN is one such facility where the cooler Penning trap is being developed to cool HCIs, which will be discussed in later chapters.

2.2 TRIUMF's ion trap for atomic and nuclear science (TITAN)

Because of the challenging task of radioactive beam production, there are only a handful of facilities worldwide that can measure the masses of short-lived isotopes in the range of millisecond halflives. ISOLTRAP [33] at CERN, CPT [34] at Argonne National Laboratory USA, JYFLTRAP [35] at the University of Jyväskylä, Finland, SHIPTRAP [36] at GSI Darmstadt, Germany, LEBIT [37] at Michigan State University in the USA and TITAN [38, 39] at TRIUMF are dedicated to the mass measurement of short-lived isotopes. Fig. (2.5) shows the TITAN beam line and the traps that are currently operational.

The TITAN experimental setup is located in the ISAC experimental hall at TRIUMF. TITAN specializes in the mass measurement of short-lived isotopes, with lifetime usually in the range of milliseconds. TRIUMF's ISAC radioactive beam facility provides rare isotopes by impinging a $\sim$480 MeV proton beam on a solid target [41]. Fig. (2.6) shows the schematics of the ISAC halls and the experimental facilities located inside the ISAC-I facility. The target and the extraction process varies depending on the ion of interest. For some ion species, a laser is used to selectively ionize the isotopes that are extracted from the target [43] while a repeller plate suppresses the remaining ions [18]. After extraction from the target, the ions are accelerated and a combination of dipole magnets selects the ion of interest with a maximum resolving power of $\delta m/m \simeq 1/3000$. The continuous beam of mass separated ions is then transported to TITAN for precision mass spectrometry or for in-trap decay spectroscopy. In the sections to follow, we will briefly discuss the three traps in the TITAN system. A more detail discussion of CPET will be presented in chapter 4.

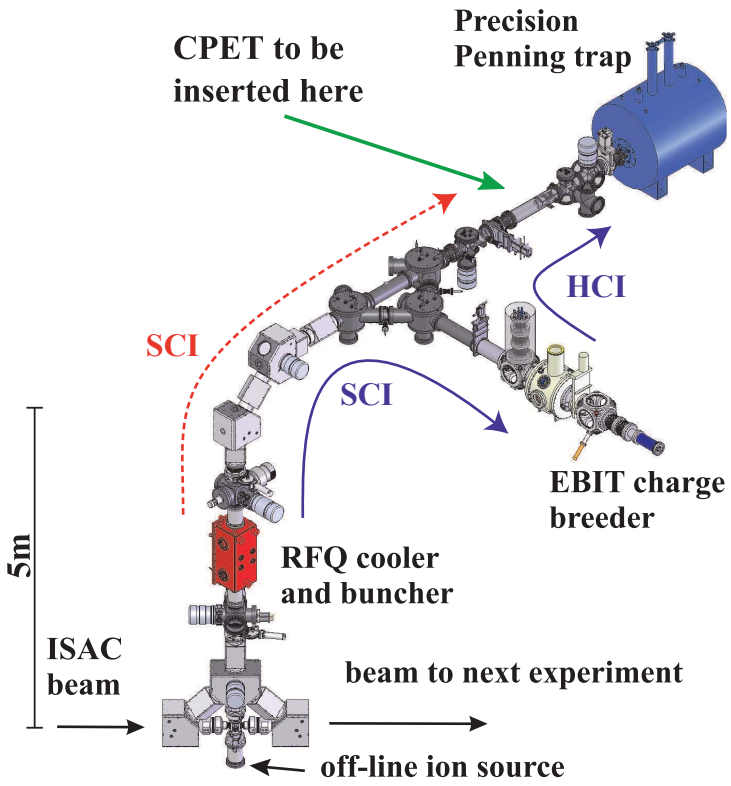

Figure 2.5: The TITAN beam-line and all the currently operational traps. Radioactive beam is delivered from ISAC and tuned into the Radio-Frequency Quadrupole (RFQ) ion trap for accumulation, cooling, and bunching. The singly charged ions (SCI) can either be transported to the Measurement Penning Trap (MPET) or to the Electron Beam Ion Trap (EBIT) for charge state boosting. CPET will be inserted right before MPET [40].

2.2.1 The Radio-Frequency Quadrupole (RFQ) Cooler and Buncher

The RFQ is the first trap on the path of ions delivered from ISAC. It is a linear Paul trap that uses sympathetic cooling (discussed in chapter 3) to reduce the energy spread among the singly charged ions using a He gas [44]. Its 24 axial segments facilitate the generation of a potential slope and well where ions undergo collision with the buffer gas and are accumulated to bunch the beam. The continuous and high emittance radioactive beams are accumulated and cooled to $\simeq$ 10 eV at TITAN's RFQ [44]. The whole RFQ assembly sits at a DC potential of $\simeq$20 kV to accept the $\simeq$20 keV beam from ISAC. A pulsed drift-tube is used to reduce the energy once the pulsed beams are extracted from the RFQ.

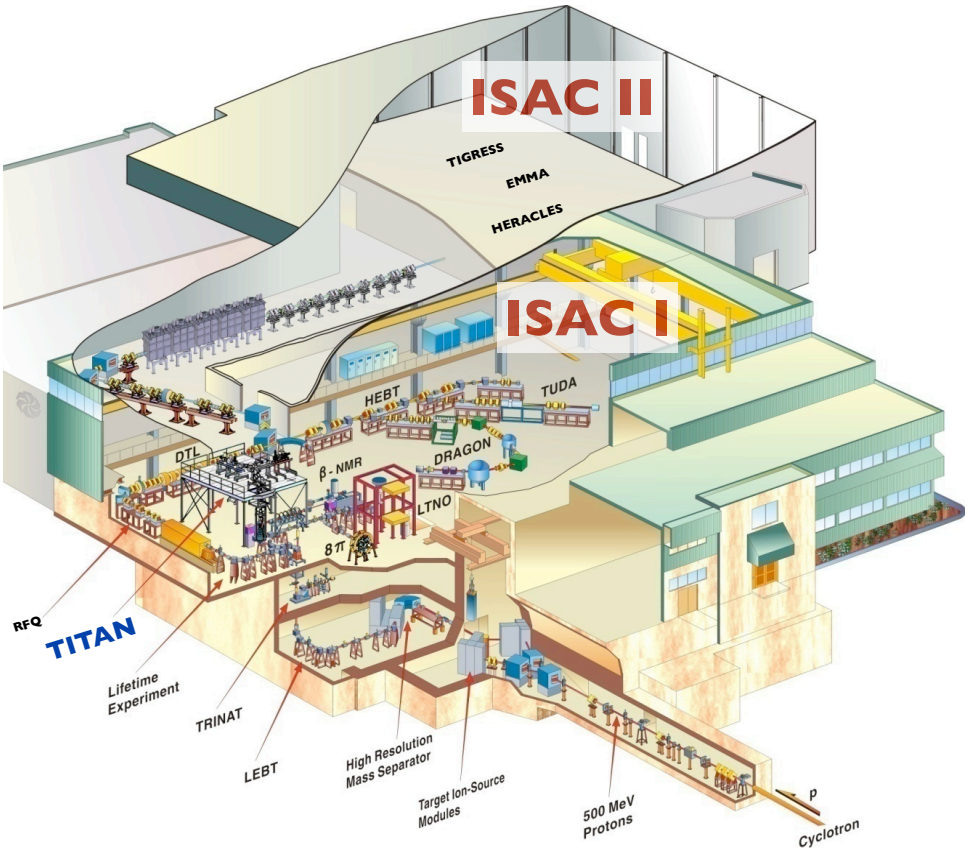

Figure 2.6: Schematics of ISAC experimental halls. The TITAN experimental facility is located in the ISAC-I hall. The path of the proton beam, target station, accelerator and other experimental facilities are shown. Figure from [42].

2.2.2 Electron Beam Ion Trap (EBIT)

TITAN's EBIT is used to boost the charge state of singly charged ions for high-precision mass measurement [45] or for in-trap decay spectroscopy measurement of electron capture branching ratios [46]. As can be seen from Fig. (2.5), EBIT has a different beam-line independent of the ion path from the RFQ to the measurement Penning trap (MPET). Depending on the desired precision level, yield, and halflives, the singly charged ions are sent either directly to the MPET or to the EBIT for charge breeding. EBIT uses an intense electron beam to remove electrons from the orbitals of the ions by means of successive electron impact. This process usually takes several milliseconds and varies slightly depending on the desired charge states [47] and ion of interest. In addition to the charge breeding, the high current density ($\vec{J}$) of EBIT also produces a strong image

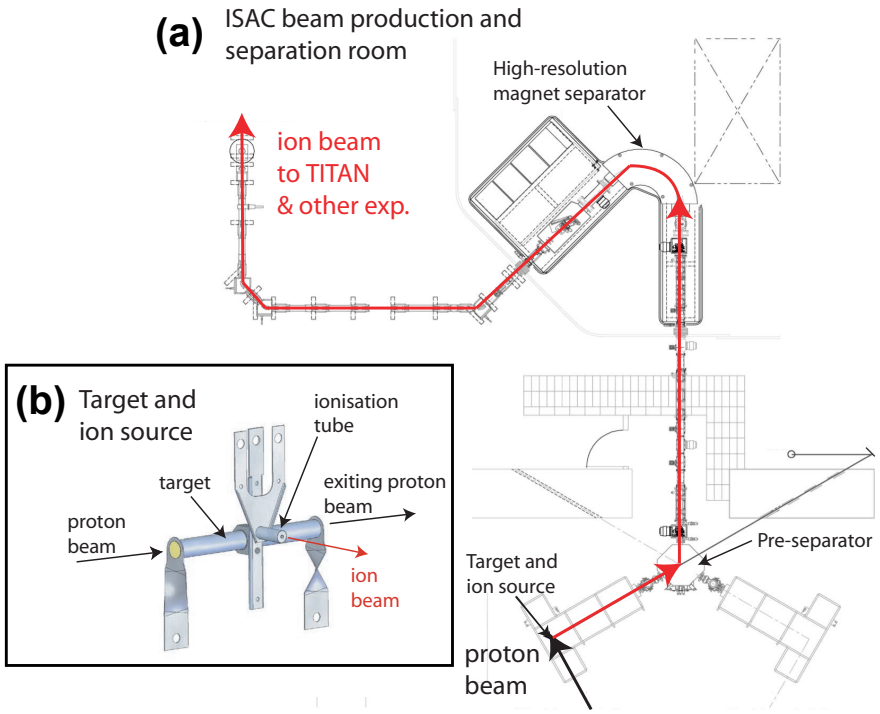

Figure 2.7: The beamline of ISAC facility and the target station. **(a)** Beam line from the target station to the ISAC facility. The target station, ionization and beam separation are shown. **(b)** A target assembly. Various parts of a typical ion source are shown. Figure from [28].

charge [3] on the trap wall that confines the positively charged ions inside the trap and works as a support for radial confinement with the magnetic field. Fig. (2.9) shows the schematic diagram of the TITAN EBIT. EBIT's superconducting magnet is in Helmholtz configuration, which means that EBIT has optical access, thus allowing for x-ray spectroscopy of HCIs [48]. Charge-bred ions are selected by time-of-flight (TOF) using a Bradbury-Nielson gate [49]. A typical TOF spectrum for different m/q is shown in Fig. (2.10). A number of experiments have been performed using EBIT since its first commissioning in 2008 [45]. The measurement of ^{74}Rb [10] for the test of the standard model and the decay spectroscopy of ^{124}In and ^{124}Cs for electron capture branching ratio determinations [48] are two examples of two different, successful measurements using EBIT.

Although the EBIT is a unique feature of TITAN that facilitates the high-precision mass measurement, the charge breeding process introduces a large energy-spread among the ions. The spread is in the range of 10-100 eV/q [50], which is a major drawback that reduces the benefit of charge

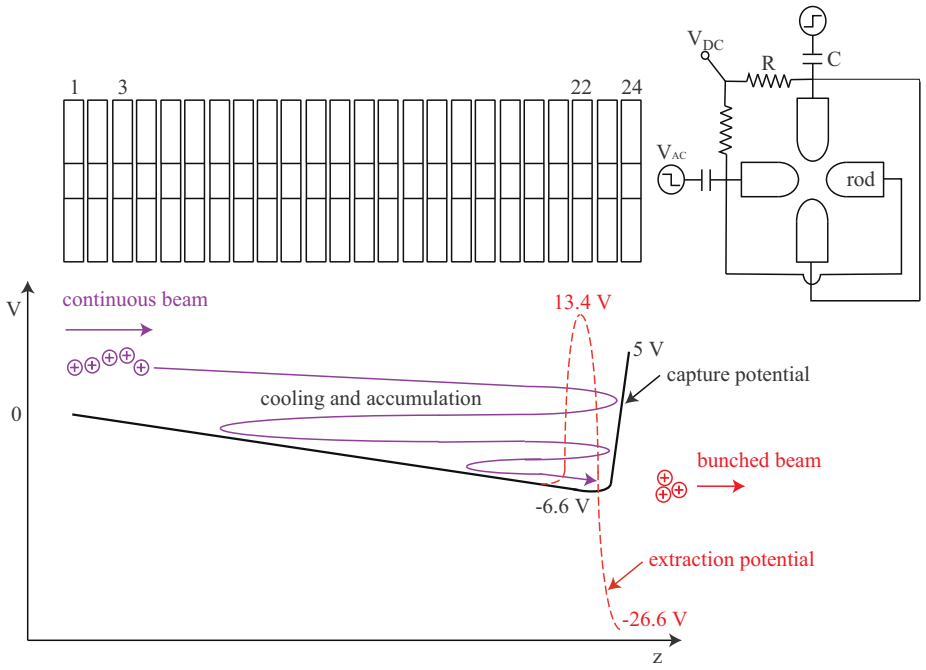

Figure 2.8: Schematics of trapping in the RFQ. The four rods, each with 24 segments, are used to apply the radio frequency for the radial confinement. Ion accumulation and bunching are achieved by adjusting the axial potential by means of the axial segments [28].

breeding. In the next chapter we further discuss the problem.

2.2.3 TITAN's Measurement Penning trap (MPET)

MPET is TITAN's hyperbolic Penning trap that is designed for precision mass measurements. As we discussed earlier, the electrostatic field perturbs the pure cyclotron motion, leading to three eigenmotions (Fig. 2.4). Once inside the MPET, the ideal situation is to have minimal axial oscillation [28] so that the ions are in the most uniform field region. For Penning trap mass spectrometry the magnetron motion (ω_-) is converted to reduced cyclotron motion (ω_+) by means of a RF excitation process. This conversion is periodic in time and allows the application of a range of frequencies on the ions. When the frequency matches the cyclotron frequency ($\nu_{rf} = \nu_c$) of the ion in the trap, we have the full magnetron to reduced cyclotron motion conversion [33]. As a result of the RF, the kinetic energy, which is almost entirely radial, increases and at the resonance it is

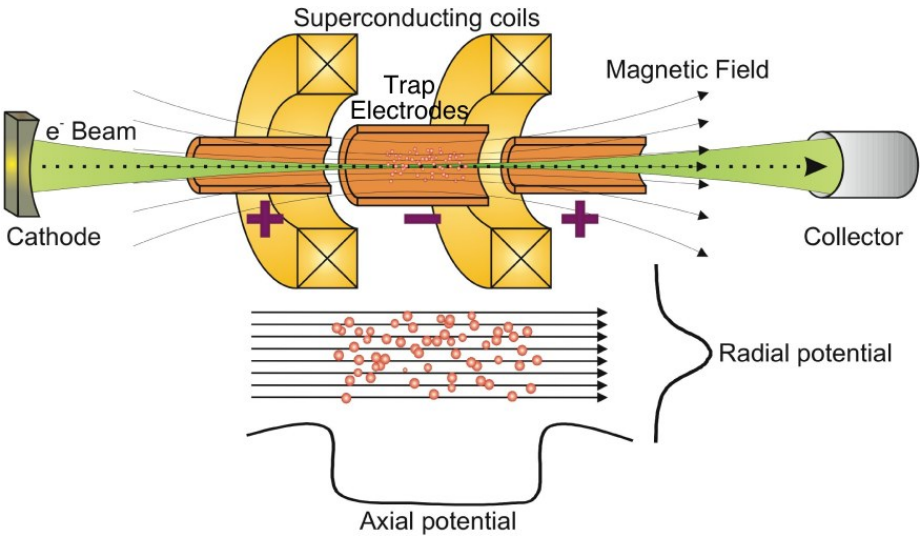

Figure 2.9: Schematic of EBIT electrodes and a cartoon of the axial and radial potential. Radial confinement is achieved through a magnetic field generated by current through coils in a Helmholtz configuration and from the space charge of the electron beam. Axial confinement is achieved by biasing the outer cylindrical electrodes higher than the middle ring electrode. The electron beam is generated by the cathode, focused by the magnetic field, and collected on the collector. Successive electron impact ionizes the singly charged ions into higher charge states.

maximum. When the ions are extracted from the trap, due to the magnetic field gradient, the azimuthal energy is transformed into axial energy. Hence, the ions that are excited by the resonance frequency have the lowest time-of-flight (TOF) to travel to the detector. This phenomenon generates a resonance TOF spectrum with respect to the frequencies applied. The global minimum of the time of flight spectrum gives an indirect access to the eigenmotion [27, 51, 52] of the ion inside the trap. A theoretical curve fitting to the TOF data yields the resonance frequency from which the mass of the ions is determined. Mass measurement by this method of exciting the cyclotron motion is known as the time-of-flight ion cyclotron resonance (TOF-ICR) method. When measured against a reference ion species whose mass is known with a very high accuracy and precision, common parameters cancel out and the systematic uncertainties can be reduced to part-per-billion level, depending on the mass difference between reference ion and the ion of interest [53]. A more detailed description of the systematics will be given in chapter 7. The uncertainty on a measured

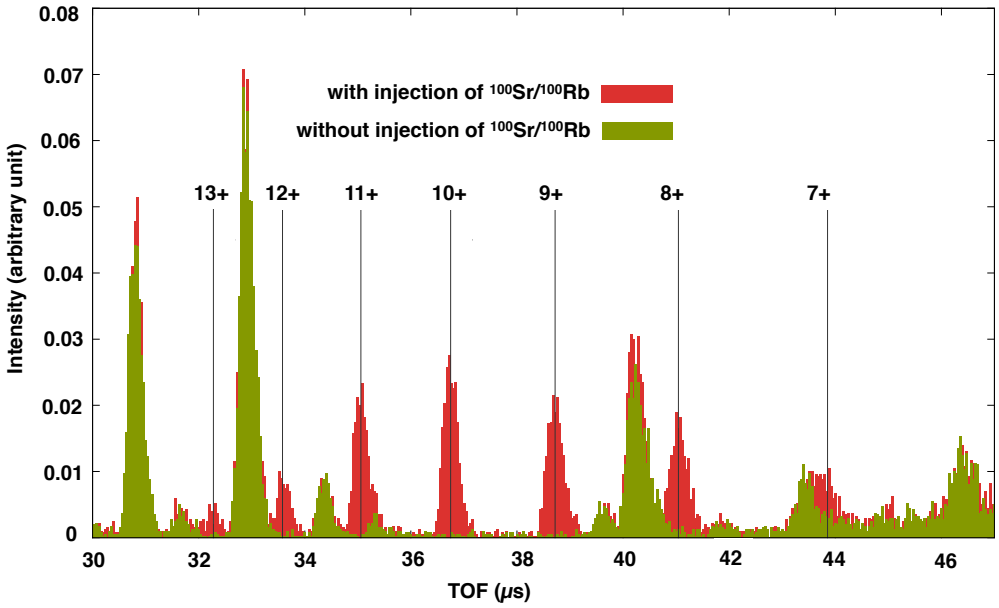

Figure 2.10: Time of flight spectrum of ions after boosting the charge state in the EBIT. When the ions are not injected, the residual gas inside EBIT is charge-bred (green). When the ions are injected, the ions (red) can be separated from the background by a Time of Flight (TOF) gate.

mass is given by Eq. (2.8):

$$\frac{\Delta m}{m} \simeq \frac{m}{qeBT_{RF}\sqrt{N}}. \tag{2.8}$$

Here, T_{RF} is the duration for which the RF is applied and N is the total number of ions detected. Eq. (2.8) also shows how higher charge states linearly increase the precision while a non-linear increase in precision occurs with increased ion number (N).

Although the charge-breeding process can enhance the precision of mass measurement significantly, this process causes a large energy spread among the ions which affects the precision of mass measurement adversely. One strategy of reducing systematic effects and the uncertainty in the mass measurement is to make the individual ion trajectories inside the MPET as similar as possible [54]. This ensures that the ions experience very similar fields. Ions with the increased energy spread will have trajectories which are far from each other compared to their colder counterparts. With increased energy spread, the ions may spend time in the relatively non-ideal region of the electric field of MPET. Above a certain energy, the ions will not be trapped at all, which means a complete

loss of the valuable radioactive particles. To take full advantage of charge-bred ions to enhance the precision of mass measurement, the above mentioned drawbacks need a remedy. In TITAN this will be solved by CPET. Once in online operation, CPET will shrink the wide energy distribution that stems from the charge-breeding and will increase the usable ion number N, thereby increasing the precision. As CPET is the main focus of this thesis, the details of the working principles of CPET are discussed in chapter 4. Before that, we briefly study the different cooling process in the next chapter, which will help us understand the reason for using the particular cooling method that CPET will employ.

Chapter 3

Cooling of charged particles

The trapping of ions and atoms opened the door to new research and observations. Some research areas, for instance, production of antihydrogen, quantum computing, laser spectroscopy, and most notably Bose-Einstein condensation, demand extremely cold ions and atoms in addition to trapping. As a result, efficient methods of cooling had to be developed. There are many experiments and observations that would not be possible without cooling the atoms. For example, to achieve precise mass measurements in Penning traps, it is important to reduce the energy spread among the ions before they enter the trap [55]. Observing Bose-Einstein condensation would not be possible without cooling the atoms to extremely low temperature [56]. The concept of ion-trap quantum computing cannot be imagined without first considering the cooling mechanism [57]. Observation of quantum jumps [58], and the work on quantum logic gates [59] all of these experiments have cooling as a prerequisite.

Cooling in atomic and nuclear physics generally refers to reducing the energy differences among the atoms and ions in an ensemble. In other words, the goal is always to reduce the phase-space volume. Depending on the final purpose, the extent of cooling varies a lot and Bose-Einstein condensation sets the ultimate low limit so far. The interaction between neutral atoms and the cooling environment (e.g. laser) is either through the atomic quantum states (most optical cooling) or the magnetic moment (evaporative cooling). Cooling in principle could be done even without

trapping the target atoms or ions; however, this kind of cooling is usually unidirectional [60]. Use of a laser along one axis along the path of the particle is an example of such cooling.

The physics behind cooling of ions and atoms is governed by Liouville's theorem. It tells us that the volume of the phase space remains constant as long as there is no external field applied:

$$\frac{d\rho}{dt} = \frac{\partial \rho}{\partial t} + \sum_{i=1}^{N} \left(\frac{\partial \rho}{\partial q^i} \dot{q}^i + \frac{\partial \rho}{\partial p_i} \dot{p}_i \right) = 0, \tag{3.1}$$

where ρ is the 6-dimensional phase space volume, q the spacial coordinates, and p represents the momentum coordinates [61, 62]. In laser cooling, a laser beam is shot into the atoms or ions to exert a force on the particles that are at the proper velocity to absorb the laser and thus modifies the second term in the bracket of Eq. (3.1) [63]. In evaporative cooling, the particles with higher momentum are allowed to escape the system, thus reducing the effective volume of momentum space (first term in the bracket, including the sum, as the number of particles decrease) and thus that of the phase space [64].

As long as the temperature is high enough to prevent the particles from interacting quantum mechanically, the distribution of the ion energy is always given by the Maxwell-Boltzman distribution and is common to any trap. As the temperature decreases, depending on the wave-functions of the particles, those with anti-symmetric wave functions (fermions, which obey Pauli's exclusion principle) and particles with symmetric wave-functions (bosons, which do not follow Pauli's exclusion principle) split out and follow Fermi-Dirac and Bose-Einstein statistics, respectively. For all three distributions, the populations n_i of a certain energy state E_i are given by the following equation:

$$n_i = \frac{g_i}{e^{\frac{E_i - \mu}{kT}} + \varepsilon} \begin{cases} \varepsilon = -1 & \text{Bose-Einstein distribution} \\ \varepsilon = 0 & \text{Maxwell-Boltzman distribution} \\ \varepsilon = +1 & \text{Fermi-Dirac distribution.} \end{cases} \tag{3.2}$$

Here, g_i is the degeneracy of the state i, μ the chemical potential ($\mu < 0$ for Bose-Einstein, $\mu \ll 0$ for Maxwell-Boltzman and $\mu = \pm ve$ for Fermi-Dirac distribution [65])

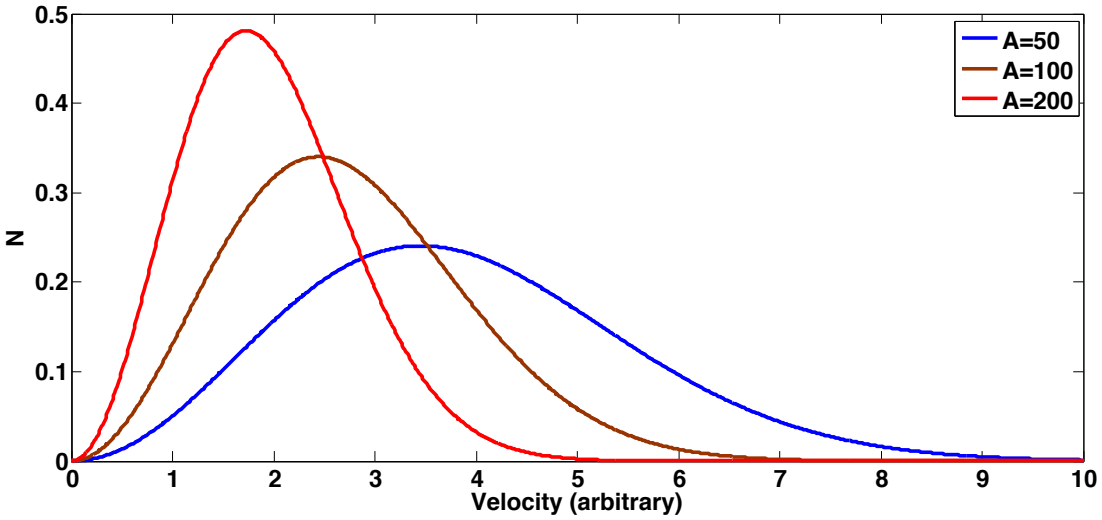

Figure 3.1: Mass dependence of the Maxwell-Boltzmann velocity distribution for different mass numbers (A).

At higher energies the distribution is always a Maxwell-Boltzman distribution ($e^{\frac{E_i-\mu}{kT}} \gg 1$), however, low energy particles (both fermions and bosons) follow Fermi-Dirac or Bose-Einstein statistics. Irrespective to the final goal of the cooling and the extent—as to how much one wants to cool the ions or atoms—the aim is always to crop the low-energy tails of the distribution shown in Fig. (3.1).

CPET is designed to cool radioactive ions. As a result, for this thesis, we focus primarily on the ion cooling methods.

3.1 Ion temperature

Before we start the discussion of cooling techniques, it is important to clarify what we mean by ion energy and temperature. These physical quantities are measured in a completely different manner compared to that of a gas that is confined by physical walls where the gas molecules heat the walls and undergo random motion. Classically, a thermocouple or a thermometer gives the temperature of a gas that is in contact with it. However, when ions are in a trap, a thermometer or a thermocouple is clearly not suitable for measuring the temperature. In addition, a small number of ions in the trap are far from what we call thermal equilibrium. Depending on the number of ions

stored, the temperature measuring method varies significantly. If the number is large enough, the plasma size and oscillation can provide information about the temperature [66]. Charge exchange, recombination radiation, and x-ray spectroscopy can also give information on plasma temperature for facilities like the tokamak or an electron beam ion trap (EBIT), respectively [67, 68]. In most cases, a spectral analysis is the best way to probe the temperature, and from this we can get information about the velocity distribution of the particles. In case of the particles in a Penning trap, the fluctuation in the ion cyclotron energy can be associated with the temperature and the analogy of Planck's black-body radiation theory can be applied, where, for the oscillator in which the average occupation number $\langle n \rangle$ is given by [26]:

$$\langle n \rangle = \frac{1}{e^{h\nu/k_B T} - 1}. \tag{3.3}$$

Since temperature and energy are related by the classical relation $T = \frac{\bar{E}}{k_B}$, mentioning only the temperature is usually sufficient.

From these relations we can get information about the temperature [21]. For example, for a single ion in a Penning trap, the distribution is found to be thermal by studying the cyclotron frequency.

The optical transitions of atomic states provide information about the temperature as long as the Doppler region is not reached, i.e. the ion's oscillation amplitude a is much larger than the wavelength of the laser (λ) being used. However, as the temperature becomes lower (below Doppler limit, small $\langle n \rangle$ and $a < \lambda$), the system becomes quantum mechanical and the quantum mechanical behaviour puts a barrier on measuring temperature without interrupting the system, as is true in the case of any quantum system. To extract information from such a fragile system, a laser is used again with appropriate frequency corresponding to the electronic transition of the ion. The line width of the fluorescence is then measured as a function of the laser frequency. With all the line broadening effects taken into consideration, including the radiative lifetime of the excited state, collision broadening, the laser spectral width and the expected Doppler effect, a curve fitting is

done with the theoretical equation from which the temperature is extracted [21].

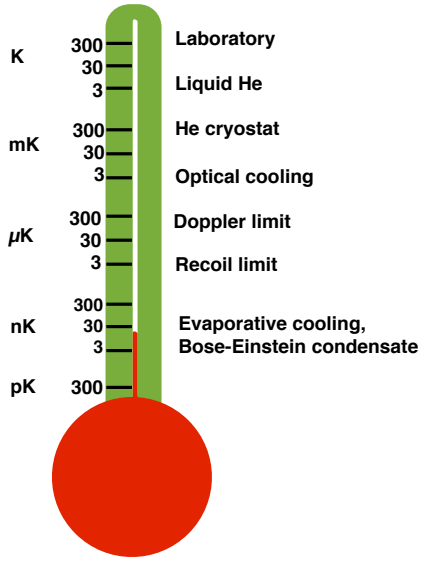

Figure 3.2: Temperature scale of different experiments.

Fig. (3.2) shows some major cooling methods and their temperature limits.

3.2 Cooling of ions

Cooling of ions can be performed in a number of ways and different cooling techniques are suitable for different setups [69]. The most commonly used cooling techniques are:

- Resistive cooling
- Sympathetic cooling
  - Buffer gas cooling
  - Sympathetic cooling by means of charged particles
- Rotating wall compression
- Stochastic cooling
- Evaporative cooling
- Laser cooling

In the next sections we briefly discuss each of these cooling mechanisms.

3.2.1 Resistive cooling

Resistive cooling uses the image charges [3] that are induced on a trap electrode surface due to the charge of the ion or ion cloud. The image charges create a potential drop across two electrodes, between which the ion or cloud oscillates. As the ions oscillate between two or more electrodes, the energy is dissipated by means of an external resistor in a circuit [69]. The process of resistive cooling is depicted in Fig. (3.3).

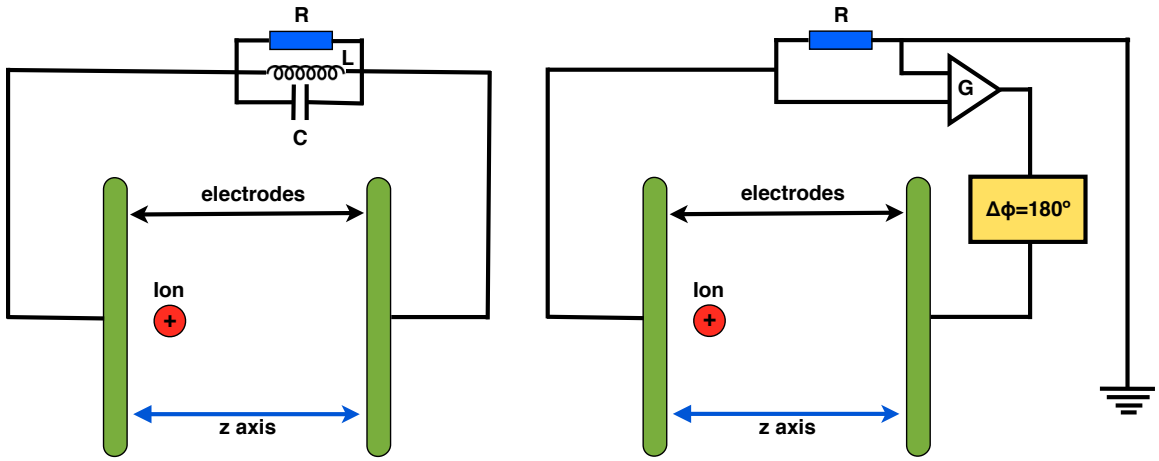

(a) Resistive Cooling of ion. (b) Resistive cooling with negative feedback.

Figure 3.3: Resistive cooling methods for ions in a trap.

The working principle in resistive cooling is the Ohmic law which says that, if a current i passes through a resistor R, then the energy dissipated through the resistor in unit time as heat is i^2R. For simplicity, we discuss the scenario of a charged particle with charge-to-mass ratio q/m oscillating between two parallel plates. We consider the charged particle oscillating along the z axis as shown in Fig. (3.3). The current due to this charged particle is:

$$i = q/t = qv_z/d, \tag{3.4}$$

where d is the amplitude of the charged particle oscillation. To relate the velocity of the ion with

its energy E we write:

$$\frac{dE}{dt} = -Ri^2 = -R\frac{q^2 v_z^2}{d^2}, \tag{3.5}$$

replacing v_z^2 with $2E/m$ gives

$$\frac{dE}{dt} = -Ri^2 = -\frac{1}{\tau_R}E, \tag{3.6}$$

where the time constant $\tau_R = md^2/2Rq^2$.

Although this method is efficient for large charge-to-mass ratio, a preferable method is the so-called negative voltage feedback technique [69, 70]. In this method the phase and amplitude of the ion motion is read by an external circuit, and an opposite voltage is applied to enhance the damping of the ion motion [70]. A schematic diagram of a negative feedback circuit with an ion in a trap is shown in Fig. (3.3(b)). The reduction in time constant is given by [70]:

$$\tau_G = \frac{1}{1+G}\tau_R, \tag{3.7}$$

where G is the gain in the circuit, and τ_R is the same time constant that one would have without the negative feedback.

3.2.2 Sympathetic cooling

Sympathetic cooling refers to cooling of one type of particle through scattering by another type. This scattering could be between different groups of charged particles, or between charged particles and a neutral gas. Examples of the former include electron, positron and proton cooling [71]. Cooling of charged particles by means of a neutral gas is called buffer gas cooling. Examples include the cooling of ions by means of H_2 or He gas [72]. Sympathetic cooling in which a laser is used will be discussed in the optical cooling section.

3.2.3 Buffer-gas cooling

In buffer gas cooling the ions are allowed to elastically collide with a neutral gas (usually inert gases like He are chosen). The ions oscillate within the buffer gas environment and energy is transferred to the buffer gas which reduces the energy of the ions. This method is successfully used to cool down radioisotopes by ISOLTRAP at CERN, JYFLTRAP at Jyväskylä [73], CPT at ANL, and by TITAN at TRIUMF. For ions of moderately low energy that have energies within the range of a few eV, the cooling process is due to a force similar to the drag force. For an ion with velocity $\vec{v}$ and mass m the damping force $\vec{F}$ is given by:

$$\vec{F} = -\delta m\vec{v}, \tag{3.8}$$

where δ is the damping constant,

$$\delta = \frac{q}{m}\frac{1}{K_{ion}}\frac{p/p_S}{T/T_S}, \tag{3.9}$$

where K_{ion} is the ion mobility, p_S the standard atmospheric pressure, p the gas pressure, while T and T_S are the gas temperature and the standard room temperature, respectively [74]. With the buffer gas, it is possible to reduce the energy spread among the individual ions below 1 eV [75, 76]. A digital radio frequency quadrupole (RFQ) cooler and buncher at TITAN is routinely used to cool radioactive isotopes for precision mass measurements [77].

3.2.4 Sideband cooling by buffer gas

Sideband cooling by means of coupling the eigenmotions in a Penning trap was successfully accomplished when electrons were stored in a Penning trap for the first time [69]. As we discussed in chapter-2, when ions are in a strong magnetic field, the field confines the ions radially giving them a cyclotron motion (ω_+ and ω_-, see Fig. 2.1(b) and 2.4). To confine the ions axially, an electrostatic field is applied which gives an axial oscillation to the ions (ω_z). Due to collisions with the buffer gas, the ions lose radial energy and the magnetron radius evolves in space. In sideband cooling this magnetron motion is coupled to either the reduced cyclotron motion (ω_+) or to the

axial motion (ω_z). At equilibrium, the final amplitudes are given by Eqs. (3.10) [69]:

$$\langle r_{\pm} \rangle = \frac{1}{\omega_{\pm}} \sqrt{\frac{\pi kT}{m}}, \tag{3.10a}$$

$$\langle z \rangle = \frac{1}{\omega_z} \sqrt{\frac{\pi kT}{2m}}, \tag{3.10b}$$

where z represents the axial amplitude and $r_{\pm}$ the cyclotron and magnetron amplitudes, respectively. This method is used at REXTRAP to cool the radioactive isotopes for acceleration and charge breeding [78].

3.2.5 Sympathetic cooling by means of charged particles

Cooling of ions by means of electrons, positrons or protons is in principle the same as buffer gas cooling except for the fact that the collisions involve Rutherford scattering. When the ions and coolants (electrons or protons) enter the strong magnetic field, the motion of the ions as well as that of the coolants are highly constrained radially by the magnetic field and axially by the electric fields. In such an environment, when both coolant and ions are allowed to mix, they undergo scattering in which the ions lose energy to the coolants. As an example, a whole cooling cycle is shown schematically in Fig. (4.1). The advantage of using charged particles instead of a buffer gas is two-fold. Firstly, charged particles interact with other charged particles more strongly than with a neutral atom and hence boost the cooling process. Secondly, if electrons or positrons are used as coolants, the energy absorbed by electrons or positrons is almost instantaneously radiated by them through synchrotron radiation, and thus there is no need to have any separate cooling mechanism for the coolant itself. Antiprotons are routinely cooled at CERN [79–81] for the production of antihydrogen atoms using this method. A Malmberg Penning trap which is also known as a multi-ring-trap (MRT) is used to trap the hot ions and the cold electrons and positrons. The geometry of a MRT allows the shaping of the trapping potential as convenient for loading, trapping, and extraction of charged particles of opposite signs. Charged particles are injected into a trap which is

usually loaded with the coolant particles trapped in so-called "nested" traps [82]. If the coolants are leptons, some time is allowed for them to self-cool via synchrotron radiation and then the hot ions are brought in. The ions are allowed to undergo collision with the coolants, and then the cooled ions are extracted. Fig. (3.4) shows the hot ions and the coolant in a MRT. This cooling method

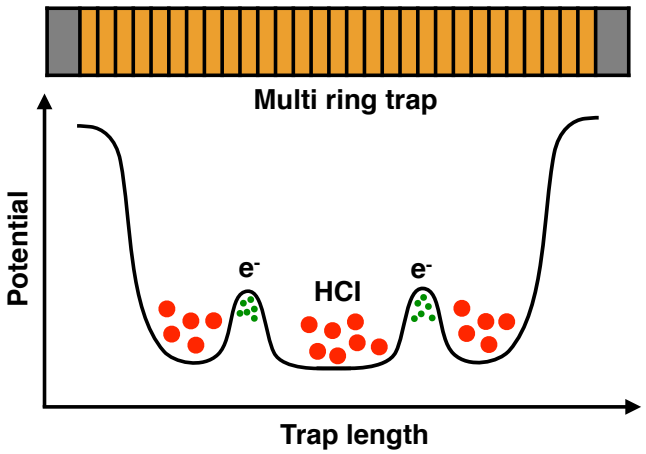

Figure 3.4: Coolant and ions in a MRT. The coolants (green) are trapped in nested traps. The hot, charged particles (red) are allowed to collide with the coolants as they oscillate axially.

will be used at TRIUMF to cool short-lived radioisotopes [55]. Further details are discussed in chapter 4.

3.2.6 Rotating wall compression

The space charge effect plays a major role when the charge density of the particle cloud in a trap is high [78]. If the density is high enough, the radius of the charged particle cloud increases, and eventually the particles are lost as they hit the trap wall. This expansion can also be a direct result of the collisions with the residual gases present in the vacuum [83]. As a result, the phase-space volume of the particle cloud increases. Rotating wall compression is an effective way of compressing the cloud under such conditions. The compression is performed by means of segmented electrodes while the charged particles are confined radially in a strong magnetic field. As the spheroid of ions rotates around the trap axis, a multipole [84] RF frequency is applied to the trap electrodes which drag and rotate the ion or electron cloud around the trap axis on top of the their intrinsic

rotation. If the applied multipole frequency is higher than the charged-particle spheroid's intrinsic frequency, an overall spatial (radial) compression is achieved by exciting a plasma wave [85]. Fig. (3.5) shows schematically how the cooling is performed by means of segmented electrodes.

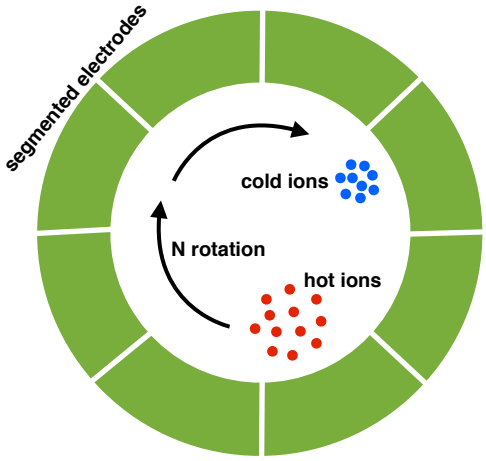

Figure 3.5: Rotating wall cooling is performed by means segmented electrodes. After a number of rotations of the cloud, the desired energy distribution and compression could be achieved.

In general, for larger numbers of charged particles, the radius of the cloud is a function of temperature [78]. However, in rotating wall compression the temperature effect is reduced and the radius of the cloud becomes predominantly a function of ion number instead. For a charged particle cloud with density n_0 and N_{tot} particles with an aspect ratio α, the radius of the cloud is given by [78]:

$$r_{\text{cloud}} = \left(N_{\text{tot}} \frac{3}{n_0 \alpha(n_0) 4\pi} \right)^{1/3}. \tag{3.11}$$

Because of the conservation of phase space density, for ions, rotating wall compression causes a heating of the ions and requires some other mechanism to take out the energy [78, 86]. In case of electrons and positrons, the energy is radiated via synchrotron radiation [87, 88].

3.2.7 Stochastic cooling

Stochastic cooling is similar to negative feedback, resistive cooling in terms of the basic principle. In stochastic cooling the average displacement or energy spread of an ion cloud in a storage ring

is read and this information is sent to a so-called kicker, which based on the information of the average displacement, applies an appropriate potential at a precise time in order to slow down the cloud [69]. Fig. (3.6(a)) shows the schematic diagram for stochastic cooling in a storage ring. Stochastic cooling was theorized for Penning traps (both hyperbolic and multi-ring Penning traps)

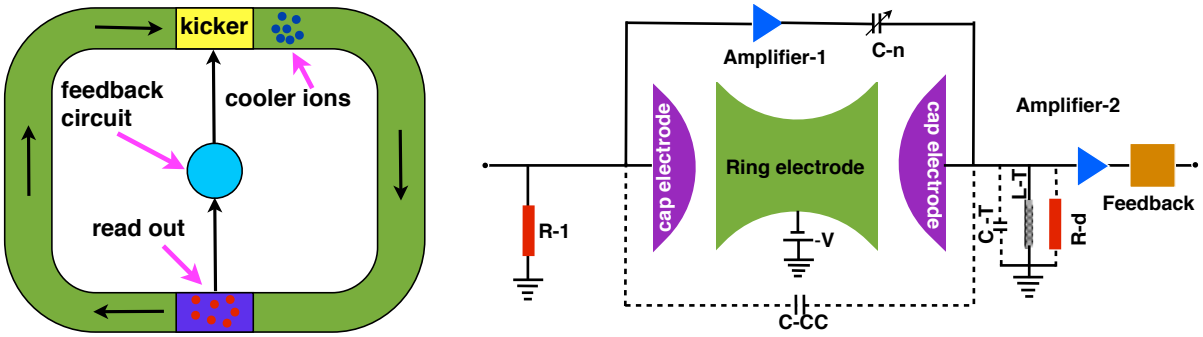

(a) Stochastic cooling in a storage ring.

(b) Stochastic cooling circuit for a Penning trap. Reconstructed figure from [89].

Figure 3.6: Two different methods of stochastic cooling.

[89, 90], and cooling was successfully accomplished [91] in them. A circuit for stochastic cooling in a Penning trap is shown in Fig. (3.6(b)). However, in Penning traps the space limitation prevents putting the read-out and kicker at different locations. As a result, in the Penning trap these two elements are merged into a single element. Instead of the spatial position of the elements (read-out and kicker) the position of the ion cloud in time is used to control the action. Assuming the noise is only due to the thermal noise of the electronic circuit, the effective cooling constant is given by [69]:

$$\tau_{\text{stoch}} = \frac{k_B T t_0}{\varepsilon_{\text{lim}}}, \tag{3.12}$$

where t_0 is the time constant that we had for the resistive cooling (see resistive cooling section), and ε_{lim} is the limiting value that the energy-per-ion can decrease to.

3.2.8 Evaporative cooling

Evaporative cooling of atoms or ions is analogous to cooling a hot cup of coffee. In both circumstances the objects are confined in space; for coffee it is the cup and for ions it is usually a

combination of magnetic and electric fields. The most energetic particles evaporate from the confinement as they have sufficient energy to escape. Evaporative cooling is also called self-cooling as there is no need for any other external source to participate in the cooling process except for the field involved in trapping. Evaporative cooling is one of the most successful methods to reduce the phase space [92] volume and to achieve extremely low-temperature. Bose-Einstein condensation was observed by cooling atoms using this method [56, 93]. For evaporative cooling there are a number of methods in use. Cooling can be performed with the so-called pulsed evaporative method [94] where the potential of the trap is reduced in steps to enhance the evaporation. In the SMILE-II trap, axial evaporative cooling was demonstrated in a Penning trap [95]. Taking advantage of the long-range Coulomb interactions of charged ions, evaporative cooling can be accomplished both axially and radially [96]. The collision strength being proportional to q^2 favours evaporative cooling of highly charged (q) ions (HCI). The variations in evaporative cooling comes in the clipping

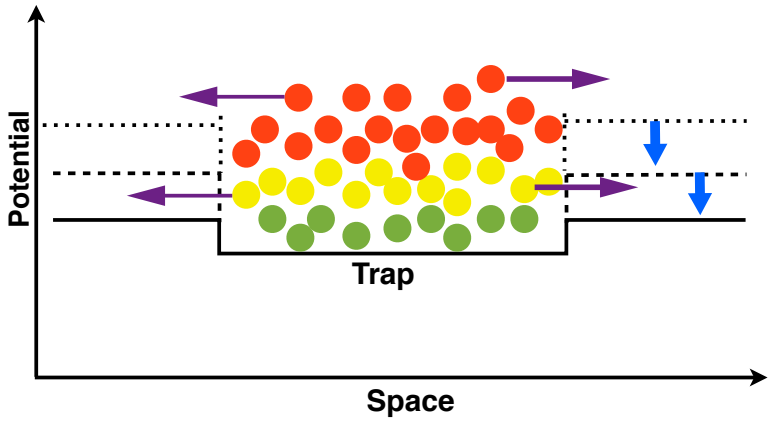

Figure 3.7: Evaporative cooling. The trapping potential is lowered gradually in steps to allow the particles to gain a new equilibrium and then for the relatively more energetic particles to escape the trap.

process of the left hand tail of the distributions shown in Fig. (3.1). With the simplification of considering only the s-wave scattering (i.e. zero angular momentum) a model is presented in Ref. [92] to predict the loss of energy and ions. If we have ions with energy ε and a trap depth of ε_t, particles with energy $\varepsilon > \varepsilon_t$ are practically free. As a result these particles escape the trap, resulting in a decrease in energy per particle in the trap. The potential can be adjusted so that more and more

particles escape the trap, leaving only the very low energy ones inside the trap. In a trap with an effective evaporating volume [92] given by V_{ev} and W_{ev}, with $\eta = \varepsilon_t / k_B T$ the truncation parameter, the loss of ions (N_{ev}) and their energy (E_{ev}) are given by [92]:

$$\frac{dN_{\mathrm{ev}}}{dt} = -\sqrt{\frac{8k_BT}{\pi m}} n_0^2 \sigma e^{-\eta} V_{\mathrm{ev}}, \tag{3.13}$$

$$\frac{dE_{\mathrm{ev}}}{dt} = \frac{dN_{\mathrm{ev}}}{dt}\left(\eta + \frac{W_{\mathrm{ev}}}{V_{\mathrm{ev}}}\right) k_B T, \tag{3.14}$$

respectively. Where σ is the energy-independent scattering cross section at temperature T [92].

It is interesting to note at this point that, although this calculation is done in the s-wave regime, ions can easily be brought to this configuration by means of stripping off the electrons and closing an atomic shell.

3.2.9 Optical cooling

Optical cooling or laser cooling is a clean way of cooling the ions. The reason behind calling the cooling technique clean is that in this process there is no chance of any contamination due to charge state loss or entrance of other ions species as is the case for sympathetic cooling. However, laser cooling is only limited to neutral atoms, or at most to singly-charged ions of very few species. It is a common practice to enhance the cooling by means of trapping the atoms or ions in a weak magnetic field. With the magnetic field on, the optical traps are called magneto optical traps or MOTs [95]. This process is very efficient for cooling atoms or ions to the sub-Kelvin level. Laser cooling can be divided into the following major categories:

- Doppler cooling
- Sub-Doppler cooling
  - Sideband cooling
  - Sisyphus cooling

– Sub-recoil cooling

3.2.10 Doppler cooling

The Doppler effect is the phenomenon in which the frequency that an observer sees for an electromagnetic wave is a function of the relative velocity between the source and the receiver. According to the Doppler effect, the frequency ν_0 in the laboratory frame of reference detected by an observer with a velocity v_r is modified to:

$$\nu = \left(\frac{1-\beta}{1+\beta}\right)^{1/2} \nu_0, \tag{3.15}$$

where $\beta = v_r/c$.

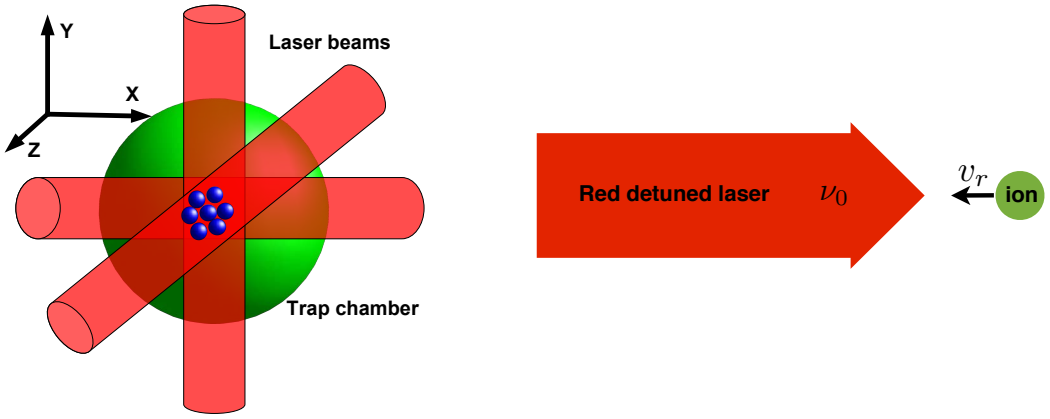

(a) Laser cooling with Doppler principle. (b) Red-detuned laser and Doppler cooling.

Figure 3.8: Laser cooling.

Now, for any ion (i.e. the receiver) with the relative velocity v_r, travelling in the opposite direction of the laser beam with frequency ν_0, the photon will be absorbed by the ion only if the electronic transition of the ion has an energy $E_T = h(\nu_0 + \Delta\nu)$, where h is Plank's constant and $\Delta\nu = \nu_0 - \nu$. As a result of the absorption, the ion is excited and loses momentum because of the inelastic collision between the ion and the photon. Although there was a specific direction along which the laser was shot, the direction of emission is random, so is the direction of the ion recoil. The statistical average of such absorption and emission results in a decrease in velocity along the direction at which the laser is shot. Often the ions that get the kick and speed up become

transparent to the laser and leave the trap while the ions that get the kick and slow down also become transparent to the laser (but not to the weak magnetic field) but remain in the trap as expected. The laser can then be tuned to a lower frequency and thus the ions that are in resonance with the new frequency can be filtered out based on their energy. This process can continue until all the atoms are transparent to the laser. An ion cloud temperature of $\sim 10^{-5}$ K can be achieved by means of Doppler cooling [63], referred to as the Doppler temperature given by [97]:

$$T_D \cong \hbar\kappa/4k_B, \tag{3.16}$$

where κ is the optical decay rate.

3.2.11 Sub-Doppler cooling

As Doppler cooling is limited by the recoil of the ions, sub-Doppler cooling can be used to further cool them. Sub-Doppler cooling is performed in a number of ways, some of which are discussed below.

3.2.11.1 Sideband cooling

In sideband cooling, the cooling mechanism is directly related to the harmonic oscillations of the ions (in a harmonic trap). In the case of Doppler cooling, the applied, detuned laser matches the resonance frequency (of photon absorption) due to the ion's spatial motion. Whereas in the case of sideband cooling, the resonance is due to the oscillation of the ion in the trap. In addition, Doppler cooling involves the excitation of the ion's internal quantum mechanical state, whereas the excitation in sideband cooling is related to the excited state of the ion with respect to the trap. As a result, sideband cooling is considered a mesoscopic phenomenon [97], whereas Doppler cooling is microscopic. It is possible to reach the 3D zero-point energy state by means of sideband cooling provided cooling is done for a sufficient time [59]. If the ions are cold enough, and are in their internal ground state $|g\rangle$, and at an energy state $|n\rangle$ with respect to the trap, we represent the state as $|g,n\rangle$. If the ion's internal transition frequency is ω_A and the quantized vibrational transition

states in the trap has frequency ω_T, then we can write the transitions as:

$$|g,n\rangle \xrightarrow{+\omega_A} |e,n\rangle \tag{3.17a}$$

$$|g,n\rangle \xrightarrow{-\omega_T} |g,n-1\rangle\,. \tag{3.17b}$$

A schematic diagram of the cooling process is shown in Fig. (3.9). If the resolved sideband

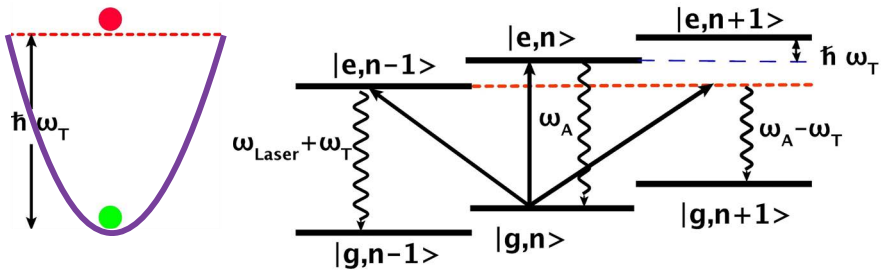

Figure 3.9: Sideband cooling of ions in a trap with harmonic potential. Reconstructed figure from [97].

cooling Eqs. (3.17a) and (3.17b) are combined, the transition takes place is given by:

$$|g,n\rangle \xrightarrow{+(\omega_A-\omega_T)} |e,n-1\rangle\,. \tag{3.18}$$

Eq. (3.18) implies that a laser that can drive such a transition must have a frequency:

$$\omega_{Laser} = \omega_A - \omega_T. \tag{3.19}$$

Shortly after pumping up to an excited state, the ion returns to its internal ground state as a result of spontaneous emission. This spontaneous emission will cause the ion to recoil and for this reason it is necessary that the ions are trapped firmly so that the recoil can be ignored [98]. If we can ignore the recoil, the state is given by $|g,n-1\rangle$, which means the ion gets cooler. If the laser is shot along the x-axis, to an ion with velocity v_x and cross-section $\sigma(\omega)$ then the rate at which the ion loses energy is given by [23]:

$$\frac{dE}{dt} = \frac{I}{\hbar\omega}\sigma(\omega)(\hbar k v_x + 2R), \tag{3.20}$$

where I is the energy flux of the laser beam, k is the magnitude of the photon wave vector $\vec{k}$, and R is the recoil energy given by $\hbar k^2/2m$, with m being the mass of ion [98].

3.2.12 Cooling with a polarization gradient

Experimentalists first observed the cooling due to a polarization gradient when they were trying to cool Na atoms by means of Doppler cooling which has a lower limit of $\sim 240\mu$K. But to their surprise they observed much cooler atoms at $\sim 43\mu$K [99]. So they knew that some other cooling mechanism must be taking place that they did not know of. In fact, it was the polarization gradient that was playing a role in cooling the atoms. In short, the method of polarization gradient makes the ions climb a potential slope and lose their energy and become cooler. This is possible only in a standing wave and by not allowing the ions to fall from the potential hill. A laser is detuned and the polarization is adjusted in a way so that the optical pumping rate is slower than the atomic centre-of-mass motion in the laser field. As a result, the ions on average experience the uphill more than the downhill thus causing an energy loss. This technique, as shown in Fig. (3.10), could be used in two different polarization schemes that we will discuss here.

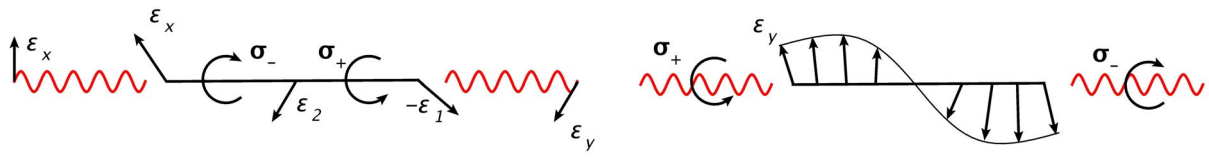

(a) lin $\perp$ lin configuration cooling (b) $\sigma_+\sigma_-$ configuration cooling

Figure 3.10: Laser cooling taking advantage of the polarization gradient. Reconstructed images from [100].

3.2.12.1 Sisyphus cooling

Similar to sideband cooling, in order to reach the sub-Doppler limit, Sisyphus cooling can be used, which also involves the use of a laser-polarization gradient [100, 101]. In Sisyphus cooling two counter propagating, linearly polarized lasers which have a direction of polarization perpendicular to each other are used [102]. As a result, this method is titled as cooling in the lin$\perp$lin configuration. Cooling of $^{24}Mg^+$ ions has been reported for the transition of $J_g = 1/2 \rightarrow J_e = 3/2$ in a

Figure 3.11: Sisyphus cooling.

storage ring, however, there is nothing to prevent similar cooling in linear ion traps [103].

3.2.12.2 Cooling in $\sigma^- - \sigma^+$ configuration

Similar to Sisyphus cooling, if the counter propagating lasers are circularly polarized, we call this the $\sigma^- - \sigma^+$ configuration as depicted in Fig. (3.10(b)). Although numerical simulations [102] and theoretical calculations [101] have predicted the potential use of this method, this type of cooling has yet to be realized for any kind of ions in any experimental facility so far (to best of my knowledge).

3.2.12.3 Subrecoil cooling

Photon recoil sets a very strict limit on the laser cooling. Even when the ions are cold enough, they do interact with the environment via photon exchange. Isolating a system from such interactions and avoiding heating due to photon recoil requires even more clever techniques. This includes the so-called sub-recoil cooling. Subrecoil method of cooling is used mostly on neutral atoms and is yet to be applied to any ion yet.

3.3 Conclusion

Neutral atoms are cooled using some of the above mentioned methods, and they are then used to cool the ions to very low temperatures [104]. Applications of such cold ions include (but are not limited to) the formation of Coulomb crystals [105], research related to cold chemistry [104], and for the use in quantum computing [57]. Mass measurements of HCIs (or singly charged ions) do

not require cooling to such low temperatures. Measurement Penning traps (e.g., MPET for TITAN) confine the ions axially by means of static fields and can accept ions of a few eV energy spread. By adjusting the electric field one can still keep the ions very close to the trap centre where the field is least perturbed [28]. As a result, ions cooled to $\sim$1eV should be sufficient for this purpose [106]. Also, although the optical cooling is naturally an excellent choice because of its inherently clean nature, the requirement of a narrowband laser source and a suitable atomic energy level configuration presents a challenge on the choice of ion to be cooled [69]. Being a general mass measurement facility, TITAN must remain open to accept almost any ion. In addition, the multiply charged ions of any element are not possible to cool using lasers. On the other hand, buffer gas cooling is not an option as the HCIs will lose their initial charge state due to charge transfer. So, while the sympathetic cooling by means of a buffer gas can yield cooling to below 1 eV, the preservation of charge state is not possible. On the other hand, in the process of evaporative cooling, a large percentage of ions is lost to achieve the desired temperature of desired isotopes of a certain charge state, which is a major drawback when considering the cooling of rare radioactive isotopes which have very low yields. The low yield is the reason for not being able to use the resistive cooling either, where a small ion cloud will take a very long time to accomplish the cooling. Stochastic cooling also takes a long time to achieve significant cooling. The most favourable way of cooling for a wide variety of ion species and a broader range of ion cloud sizes is the sympathetic cooling with charged particles. Three very convenient choices of charged particles to cool the HCIs are electrons, positrons, and protons. While the former two have the advantage of self-cooling, the latter one is easier to load into the trap. In the CPET we will have the facility to accomplish the cooling using both electrons and protons. Considering all the merits and drawbacks, it was found [55, 106, 107] that sufficient cooling of the HCIs at TITAN for mass measurement can be achieved by means of using electrons or protons [55, 107]. In the next chapters, CPET and its working principles for cooling will be discussed in more detail.

Chapter 4

TITAN's cooler Penning trap

4.1 Introduction

The precision in mass measurements of radioactive isotopes is enhanced by increasing the charge state as was discussed in chapter 2. We also learned that the use of buffer gas is not possible to cool the highly-charged ions (HCIs). This is because maintaining the charge state is crucial when the HCIs are used for mass measurement. To overcome this challenge, a natural choice is to use some lighter, charged particle with the same polarity. Considering their light weight, the use of positrons would be the best option. However, a sufficient positron supply requires highly radioactive materials like ^{22}Na [108]. As we will discuss in this chapter, electrons can be used to perform the cooling before ion-electron recombination takes place. To accomplish the cooling by means of charged particles, a suitable trap is required. Multi-ring Penning traps (MRTs), also known as Malmberg Penning traps, have been used to study electron and positron plasmas for decades [109]. In recent years MRTs gained more popularity in the context of antimatter research at CERN [29]. Antiprotons are routinely cooled, using electron plasmas inside a MRT at CERN. Because of their versatility, MRTs are also being developed at other radioactive beam facilities to cool HCIs. This includes HITRAP at GSI [32], the RIKEN MRT [110], RETRAP at LLNL [111], and the Stockholm cooling trap [95]. HCI beams extracted from the TITAN EBIT will also be cooled using a MRT. At TITAN we named it the cooler Penning trap or CPET. In this chapter we

will discuss the CPET design, and how it will achieve the required level of cooling.

4.2 Sympathetic cooling and the working principles of CPET

In sympathetic cooling with charged particles, the trap is loaded with the coolant (electrons or protons; in the Fig. (4.1) only the electron cooling is depicted). Once there is a dense and cold cloud of the coolant, the ions are injected (by lowering the potential at the gate electrode) where they undergo Coulomb collisions [70, 112–114] with the coolant. During this process the ions lose their energy to the coolant and thus the total energy as well as the energy spread between individual ions decreases. Finally ions are extracted and sent for the mass measurement.

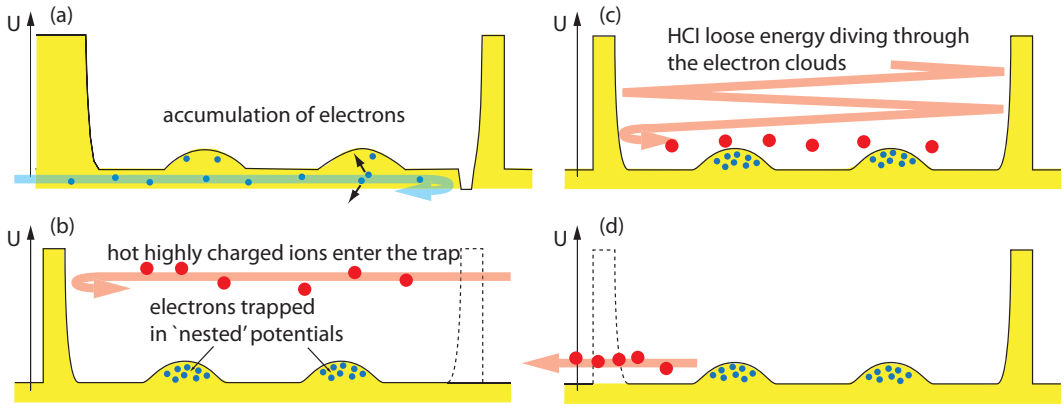

Figure 4.1: Electron cooling of the highly-charged ions. **(a)** The electrons are accumulated in the trap and they undergo self-cooling via synchrotron radiation. **(b)** HCIs with large energy-spread enter the trap. **(c)** Ions collide with the electrons and lose energy. **(d)** The cold ions are extracted from the trap.

When working with radioisotopes, it is very important to know how long it takes to cool the ions. Firstly, because of the halflives of the ions and, secondly, because of the ion-electron recombination. Too long a cooling time will cause the isotopes to decay to their daughter nuclides and hence render them useless. In addition, with time, more and more ions will undergo electron-ion recombination and also become useless. In the following we give a rough estimate of energy exchange between the coolant and the ions.

The whole cooling procedure for CPET was studied extensively by Ke [115]. Considering an ideal condition of a two-component plasma without magnetic field, and defining N_e and N_i to be

the number of electrons and ions, respectively (sharing the same volume), the rate at which the electron and ion energy (temperature) changes is given respectively by [113]:

$$\frac{dT_e}{dt} = \frac{1}{\tau_i}\frac{N_i}{N_e}(T_i - T_e) - \frac{1}{\tau_e}(T_e - T_{res}), \tag{4.1a}$$

$$\frac{dT_i}{dt} = -\frac{1}{\tau_i}(T_i - T_e), \tag{4.1b}$$

where τ_e is the time constant for electron self-cooling via synchrotron radiation in a magnetic field (which is ≈ 0.07 s in a 7 T field [115]), T_e and T_i are electron and ion energies respectively, T_{res} is the ambient temperature, while the time constant for equilibrium in a two-component plasma, τ_i, is given by [116]:

$$\tau_i = \frac{3(4\pi\varepsilon_0)^2 m_e m_i c^3}{8\sqrt{(2\pi)} n_e q^2 e^4 \ln(\Lambda)} \left(\frac{kT_i}{m_i c^2} + \frac{kT_e}{m_e c^2}\right)^{3/2}. \tag{4.2}$$

Here, k is the Boltzmann constant, m_i is the ion mass, q is the charge of the ion, v_i is the velocity of the ion, n_e is the electron density, and m_e is the electron mass.

The Coulomb logarithm ($\ln(\Lambda)$), which carries the appropriate cutoffs for the impact parameters for the electron-ion collision in the plasma, is given by:

$$\ln(\Lambda) = \ln\left(4\pi\left(\frac{\varepsilon_0 k}{e^2}\right)^{3/2}\frac{1}{q}\sqrt{\frac{T_e}{n_e}}\left(T_e + \frac{m_e}{m_i}T_i + 2\sqrt{\frac{m_e}{m_i}}\sqrt{T_e T_i}\right)\right). \tag{4.3}$$

Similar expressions can be derived for proton cooling as well [115]. The only difference is that the protons do not lose significant amounts of energy via synchrotron radiation, but the advantage is that there is no electron-ion recombination if the protons are used. Simulations were done using this model and the results for the electron cooling is shown in Fig. (4.2). As we can see, although not on the order of milliseconds (the order of life time for short-lived isotopes that TITAN can measure), the ion energy can be reduced significantly within a fraction of a second (Fig. 4.2 **a**) without losing too many of them due to recombination (Fig. 4.2 **c**).

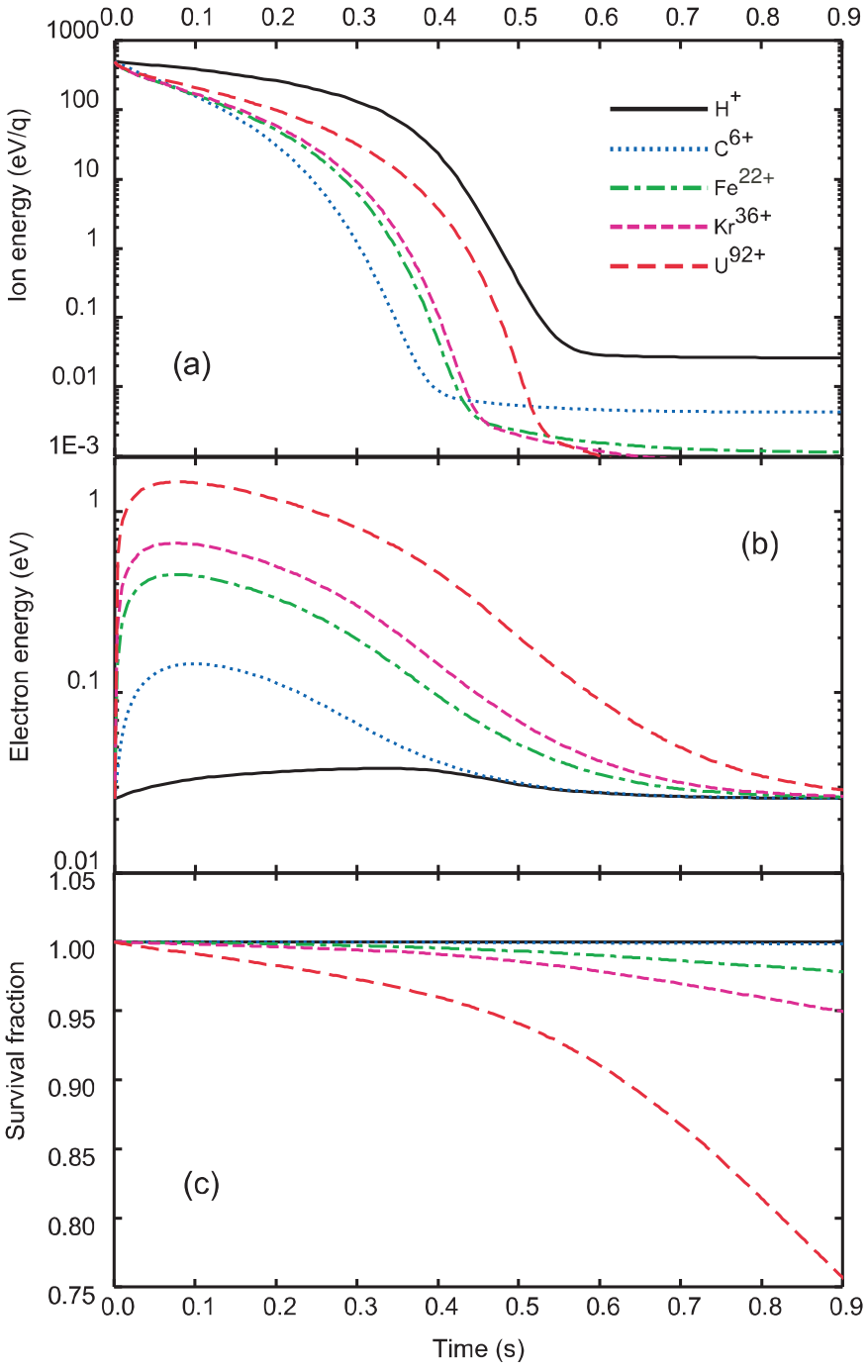

Figure 4.2: Simulation results for electron cooling. **(a)** Simulation results showing the energy decrease of various ions over time in an electron plasma. **(b)** Electron energy. **(c)** Fraction of ions that maintain their charge state during the cooling without undergoing radiative recombination. These simulations were performed taking an electron density n_e=10^7/cm^3, number of electron $N_e = 10^7$, and a total ion number of $N_i = 10^3$. In addition, only the radiative recombination between ions and electrons was considered. Contribution of three-body recombination and dielectronic recombination are ignored [115].

Although sympathetic cooling is used routinely to cool antiprotons at CERN, due to their higher electron affinity, the cooling of HCI without compromising their charge state will be more challenging. The cooling time, electron density and plasma radius, and the best charge state, all have to be tuned and optimized for an experiment.

4.3 Trap structure

CPET is a Multi Ring Penning Trap (MRT), widely known as Malmberg-Penning trap. The trap is comprised of 29 gold plated, oxygen-free, high-conductivity (OFHC) copper electrodes which give a field that is free of stray potentials [87, 117]. Fig. (4.3) shows the CPET trap assembly and the electrodes. Each electrode has a 35 mm inner diameter and a length of 12.7 mm. The gap between the trap electrodes is 1 mm.

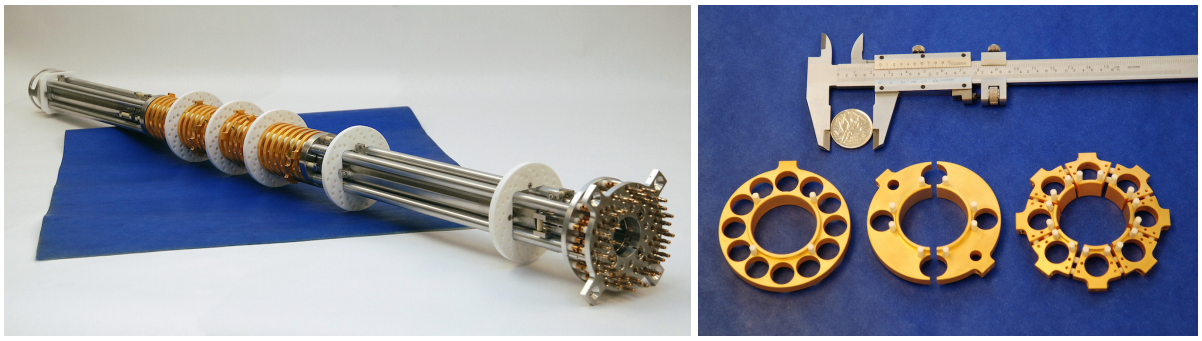

Figure 4.3: Left: The trap assembly with rods and ceramic support parts. Right: Three types of gold plated electrodes.

Two sections of the trap with a total of 6 electrodes are designed to apply RF fields. Each section has 2 two-split electrodes to apply dipole cleaning (Fig. 4.4) on each side of 1 eight-split electrode to facilitate the rotating wall compression as discussed in chapter 3 [25, 118, 119].

The trap is housed inside the room-temperature bore of a 7 T superconducting magnet which has a homogeneity of $\delta B/B \sim 10^{-3}$ within a cylindrical region of length 400 mm and 25 mm diameter. For the central region of 100 mm length the homogeneity is on the order of 10^{-6} [107]. Fig. (4.5) shows the CPET beam line and the major components for the off-line setup.

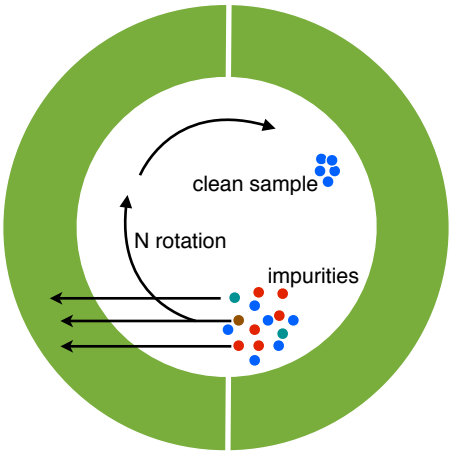

Figure 4.4: Dipole cleaning of the ions. Impurity ions can be dipole-excited to hit the trap wall to give a cleaner sample.

4.3.1 Alignment

For trapping of ions and electron plasma as well as to cool the HCIs efficiently, the $\vec{E}$-field generating electrodes and the magnetic field ($\vec{B}$) axis must align properly. The Lorentz force acting on the charged particles or plasma varies depending on the extent of the misalignment [120]. The misalignment is also responsible for changing the ideal field geometry of a trap. As a result, the better the alignment is, the higher the plasma and ion trapping time [121, 122]. The misalignment also contributes towards the enhancement and triggering of the diocotron mode (details are discussed in the later chapters) of plasma instabilities. Also, it is important to know where exactly the axis of the strongest part of the field is situated to take the full advantage of a superconducting magnet. To ensure the proper alignment, the method of field mapping [25] was adopted for CPET. For the alignment purpose, the magnetic field axis was located at 3.5 T points which are situated inside the magnet bore and then extrapolated to the bore faces as shown in Fig. (4.6).

Fig. (4.7) shows the extrapolated values in 2D.

The field mapping and aligning of the trap axis to the field axis has some very clear drawbacks. First of all, this two step method has larger uncertainty at its mapping stage [25, 123]. The hall probes, magnetometer and the mechanical system for probe positioning directly contribute to the uncertainty. Secondly, after this not-so-precise mapping, aligning the trap axis to mapped field is

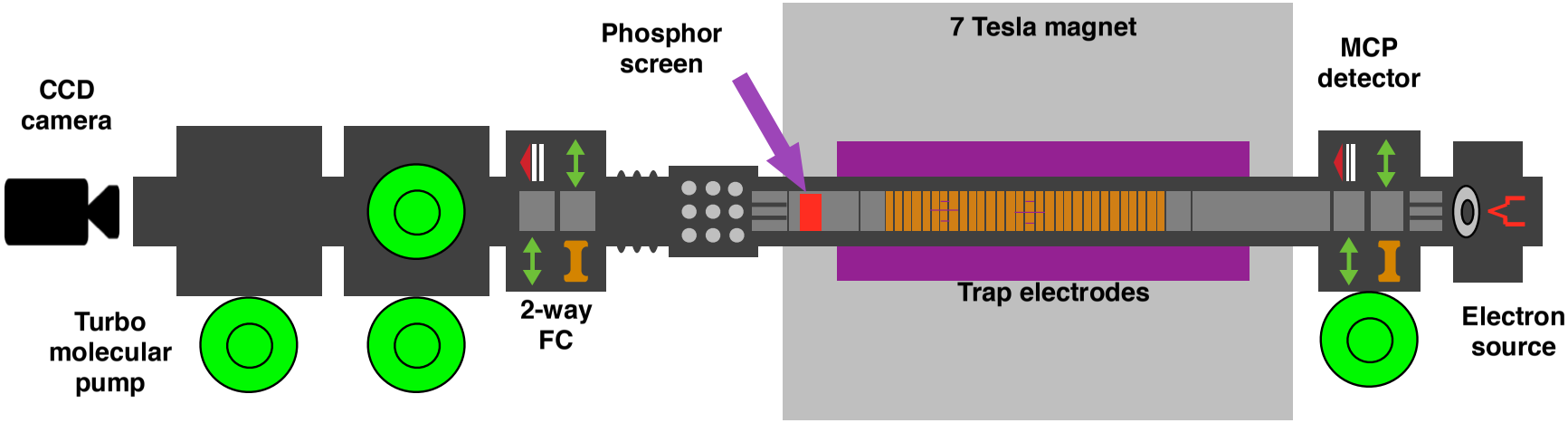

Figure 4.5: CPET offline test layout. A phosphor screen was installed inside one of the drift-tubes on the plasma extraction end (marked in red). Electron plasma profiles, plasma radius, and radial position of the plasma are calculated from the CCD camera images.

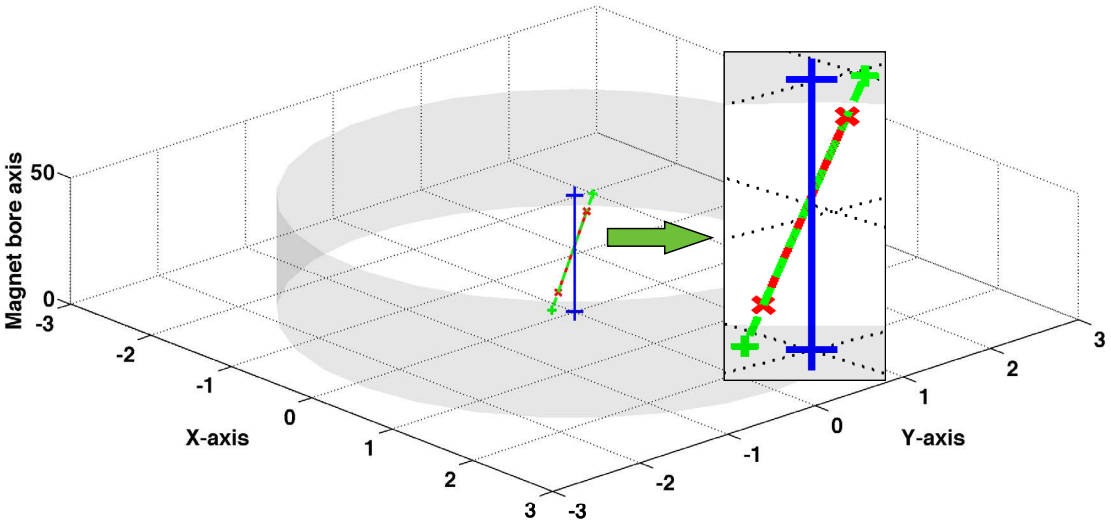

Figure 4.6: Extrapolation of the magnetic axis to both faces of the magnet bore from the half magnetic field values. The blue line shows the magnet's mechanical axis, the red line shows the magnetic axis up to half the field value and the green line shows the extrapolated line at the magnet openings. All lengths are in inch.

done with traditional survey tools. This second step has limitations of its own, most notable is the movement of the ground on which the setup is placed (in case of TITAN, the constant vibration of the platform reduces the precision). Optical aberration and error due to parallax and human judgement further contribute to the uncertainty.

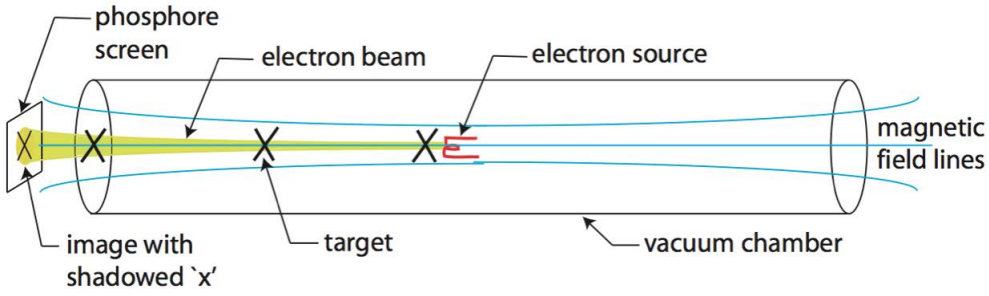

Figure 4.8: MPET alignment procedure. Figure from [28].

Fig. 4.8 shows another alignment procedure which was followed for the measurement Penning trap (MPET) at the TITAN facility. It is a one-step procedure and found to have much smaller uncertainty compared to the field mapping method [28]. In this method an electron source and a

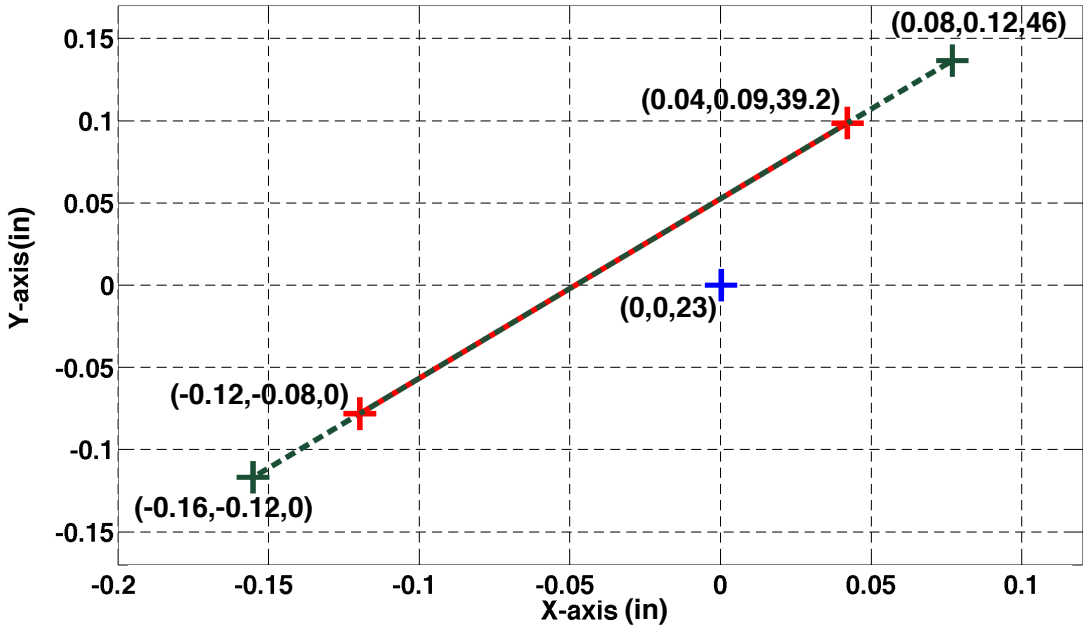

Figure 4.7: Extrapolated values from the uniform and strong field region to the magnet bore openings. Values are in inches.

combination of fine slits are used to form an 'X' image on a phosphor screen. The image of the first cross is superimposed on the second by moving the trap bore and thus a relatively more precise alignment is achieved [28, 123]. A similar method is followed at other facilities to align the trap electrodes with respect to the magnetic field [124].

Despite the drawbacks of alignment based on field mapping, we were able confine the plasma for a rather long duration, sufficient for our purposes (as discussed in the next chapter) [16].

4.4 Electron and ion sources

A tungsten hot filament (Fig. 4.9(a)) is used as an electron source that sits $\sim$1.3 m away from the trap centre (Fig. (4.5) shows the source position on the beamline). The source was tested and the current was found to be very stable compared to the field emission tip (FET) reported in ref. [119]. Details of the systematic studies with FETs will be discussed in the next chapter. During the experiment, the electron current was in the range of $\sim$100 μA at the entrance of the trap and the transmission was $\sim$20%.

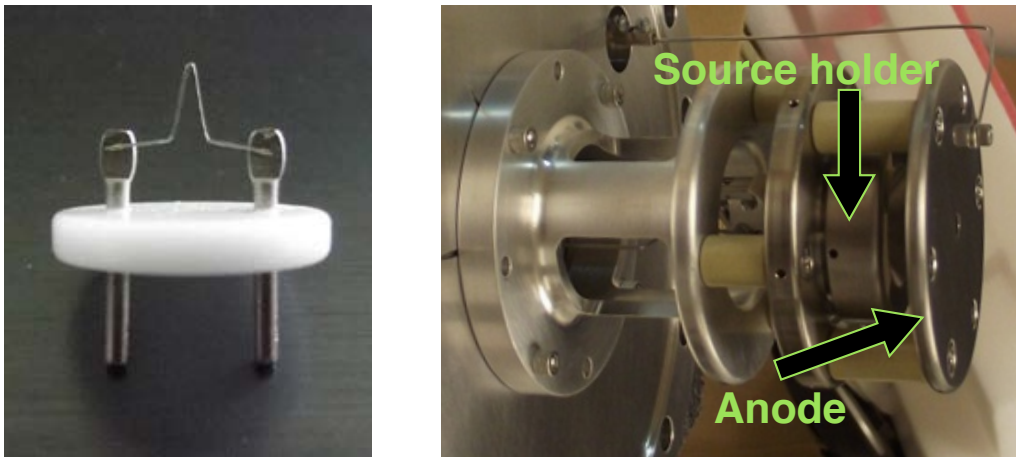

(a) Hot-filament tungsten electron source.

(b) Surface ion source holder for CPET off-line tests.

Figure 4.9: CPET electron source and ion source.

HCIs will not be available until CPET is coupled to the TITAN beam line (Fig. 2.5) and hence, the tests with HCIs will have to wait until CPET is commissioned. However, it will be possible to do some preliminary tests such as loading, trapping and extraction with singly charged ions. It will also be possible to introduce some artificial energy spread among the ions by means of an arbitrary function generator. To accomplish these vital tests, a surface ion source (same as the TITAN off-line ion source) and necessary support structures were designed and built. Fig. (4.9) shows part of the assembly including the source holder and the anode.

4.5 CPET ultra-high vacuum and the baking facility

To ensure an ultra-high vacuum, all parts inside the vacuum are cleaned following a very high standard cleaning routine that includes the use of an ultrasonic bath and the use of deionized water [25]. Four turbo-molecular pumps helped to achieve a good quality vacuum, which reached $\sim 2 \times 10^{-8}$ Torr during the tests reported in this thesis.

For further enhancement of the vacuum the whole CPET housing, a titanium tube, was coated with the non-evaporative getter (NEG) material TiZrV (Ti 30%, Zr 20% and V 50%) [125]. Tests

without the trap assembly inside showed a vacuum improvement of at least two orders of magnitude after activating the NEG coating. The heavier molecules are pumped to below the detection limit of a residual gas analyzer (RGA). During the baking process, the NEG coating is activated and thus increases the sticking probability for the common gas components in the vacuum [125], which in turn improves the vacuum significantly. The activated NEG coating's pumping rate at UHV is very high, usually in the range of thousands of litres per second [125]. Fig. (4.14) shows the RGA scans both before and after the baking. The highest baking temperature for the test was 180 ^{o}C, and total baking duration was $\sim$4 days.

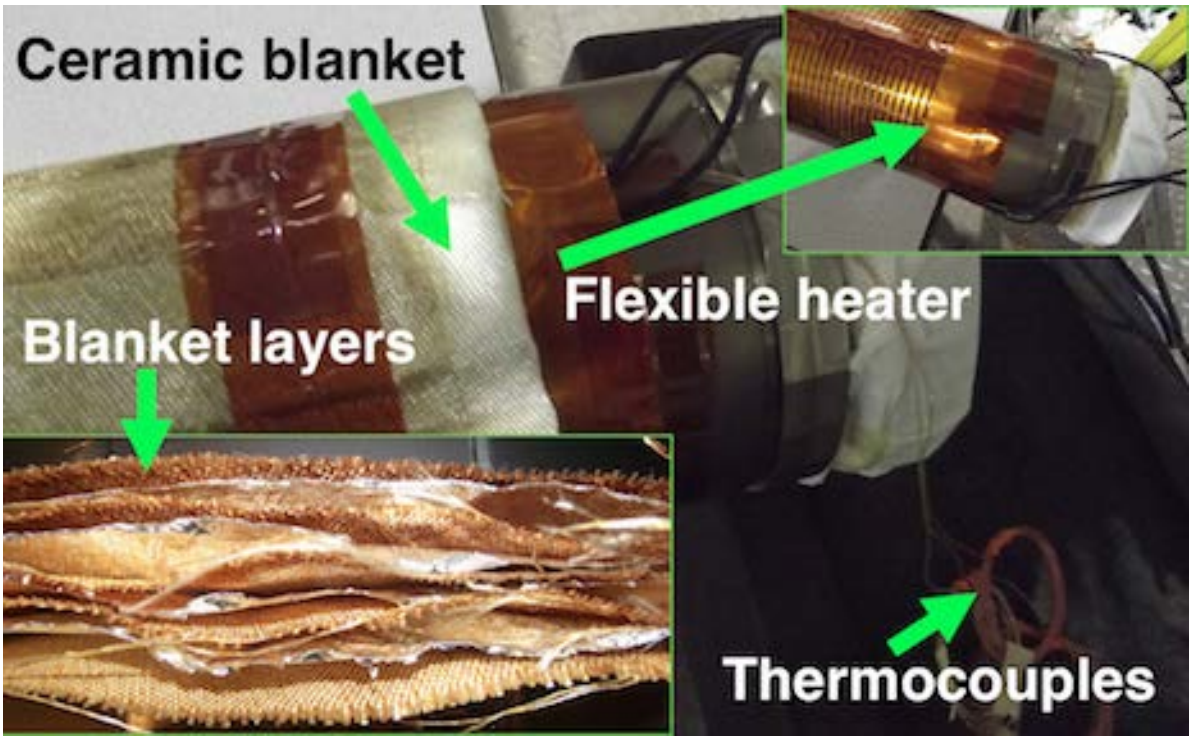

Figure 4.10: Ceramic blanket on CPET. The titanium tube with NEG coating on the inner wall and outer wall is wrapped with a flexible heater and a ceramic blanket. The custom-made Kapton flexible heater and ceramic blanket layer is shown in the inset.

Baking the trap system inside the superconducting magnet bore is very challenging, especially because of the very tight spacing we have. The trap housing has 4.5 inches of outer diameter while the inner diameter of the magnet bore is only 5 inches. To overcome this problem we decided to adopt an insulating method that uses multiple ceramic-aluminium-ceramic sandwiched layers.

Fig. (4.11) shows the insulating material and the temperature insulation it provides. The activation temperature of the NEG film is around 180 ^{o}C, which was reached using flexible heaters and a ceramic blanket from Aerospace Fabrication [126].

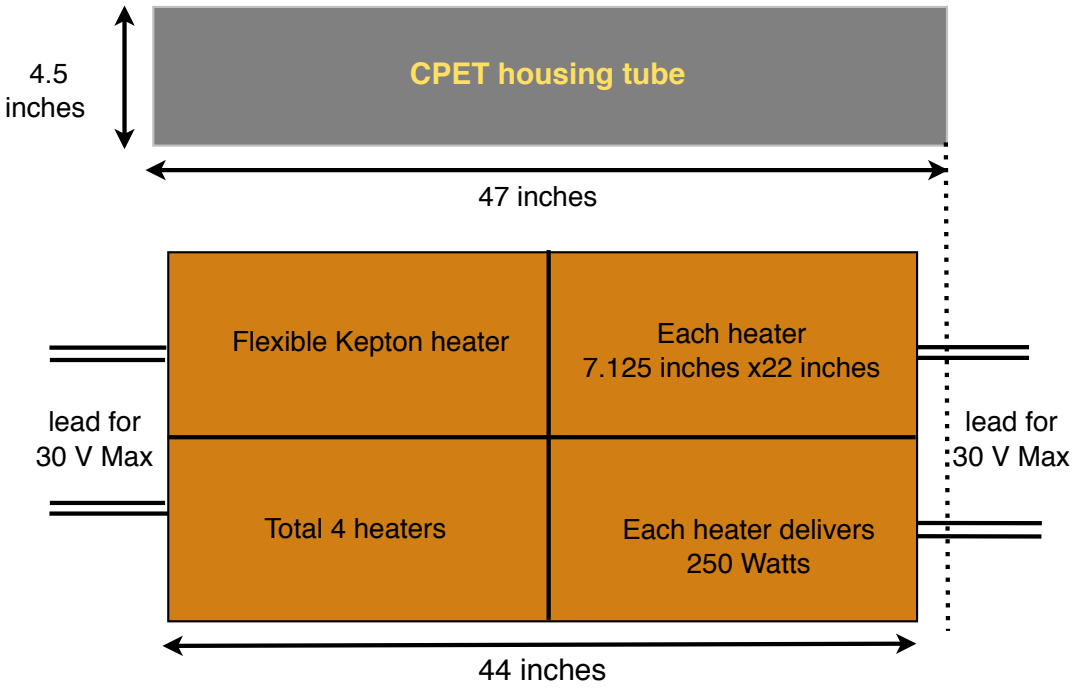

Figure 4.11: CPET's flexible heaters. A total of 4 heaters will be used to bake the trap. The combined power of the heaters is sufficient to heat the tube to 200 ^{o}C

The purpose of using the ceramic blanket is two-fold. First, to keep the trap housing warm enough so that the desired temperature is reached without too much space used (like the conventional fibre-glass insulation materials) and secondly, to prevent the heat getting radiated to the magnet bore. The maximum allowed safe temperature of the magnet bore is 100 ^{o}C, which is set by the magnet manufacturing company Cryomagnetics Inc. [127]. In the offline tests we simulated the magnet bore by a same thickness and same material (aluminum) tube of the same inner diameter.

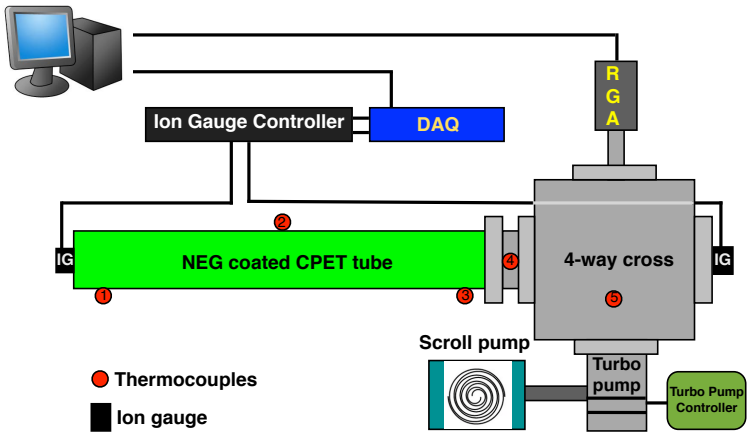

Figure 4.12: Offline baking setup for CPET. Equipped with the residual gas analyzer (RGA) and the vacuum gauges, the performance of the non-evaporable getter (NEG) coating was studied. The total pressure dropped below the measurable limit of the ion gauges after baking.

Results in Fig. (4.13) show that the blanket can keep the temperature within the safe limit. We can always bake at a slightly lower temperature and for longer period of time [125] to be more conservative and not to quench the superconducting magnet. However, below 120 ^{o}C the NEG will not activate [125].

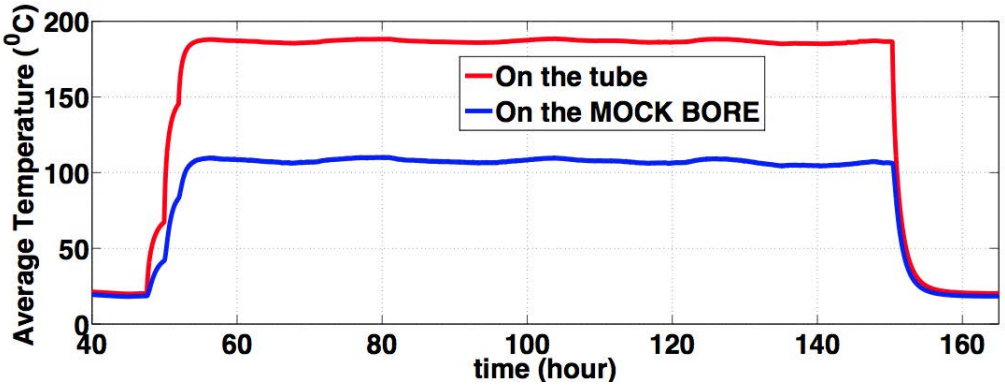

Figure 4.13: Temperatures on the magnet bore and on the trap housing. The temperature difference maintained between the trap holder tube and the mock magnet bore was satisfactory.

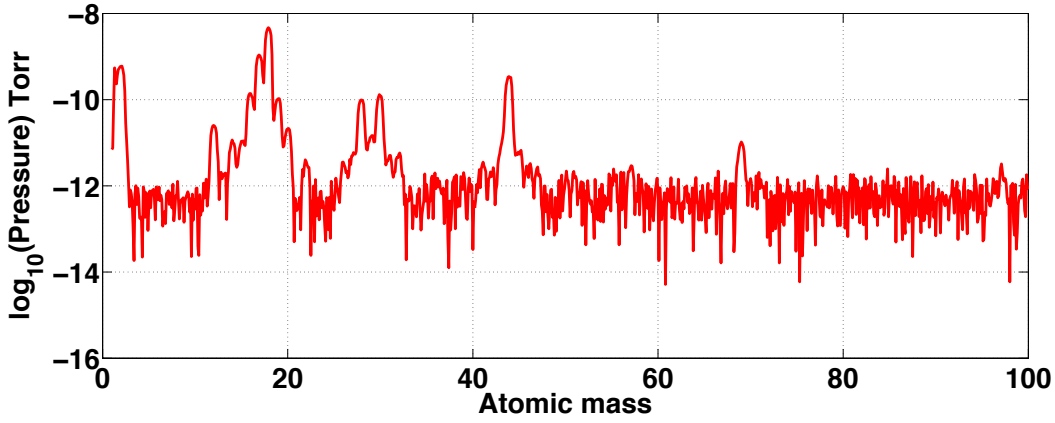

(a) RGA scan before baking.

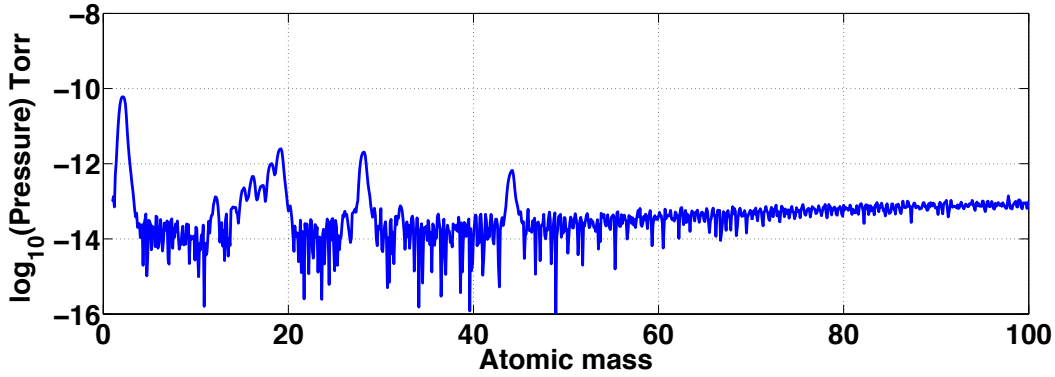

(b) RGA scan after baking.

Figure 4.14: Partial pressures before and after baking. A residual gas analyzer (RGA) was used to study the partial pressures of individual gas species.

Baking the system is always helpful to improve the vacuum, especially if the vacuum is not so good after initial pumping. However, the NEG coating has a limit, usually after ∼50 times of activation the NEG coating loses its pumping capabilities [125]. Opening the vacuum will always require a re-activation of the coating which is not very convenient and hence should be avoided during off-line tests.

4.6 Detectors

For plasma and ion diagnostic purposes we have both Faraday cups (FC) and micro channel plate (MCP) detectors at both ends of the trap. However, for a better plasma diagnosis, we have tem-

porarily installed a phosphor screen (22.22 mm active area diameter) inside the drift tube on the electron plasma extraction end. Fig (4.5) shows a schematic drawing of the present CPET setup and the position of the phosphor screen. In chapter 5 the CPET detectors will be discussed in more detail.

4.7 CPET control system

The CPET control system comprises of two major parts. One is the precise timing of loading, trapping and extraction, and triggering the CCD camera etc. The second part is the control of the potentials on all the electrodes and detectors, and reading the temperature and pressure sensors. Fig. (4.15) shows the wiring of different CPET elements as they are connected now, excluding the high-voltage (HV) switches that are controlled by the programmable pulse generator (PPG).

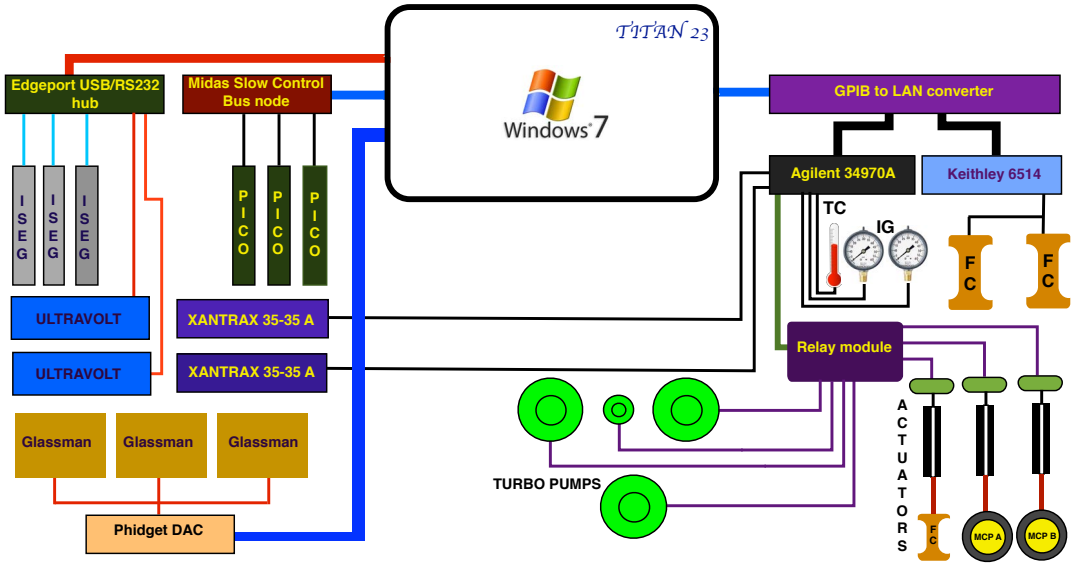

Figure 4.15: CPET control system schematic. A desktop computer with LabVIEW controls the system. See text for the acronyms.

4.7.1 Programmable Pulse Generator

A TRIUMF-made, programmable pulse generator (PPG) is used to trigger different hardware including the CCD camera and to produce appropriate pulses with precise timing. For the current

off-line tests, the PPG controls the high-voltage MOSFET switches that set the potentials at each gate electrode for electron loading, trapping and extraction. Fig. (4.16(a)) shows a typical timing scheme of the TTL signals for a complete loading, trapping, extraction, and CCD image detection cycle.

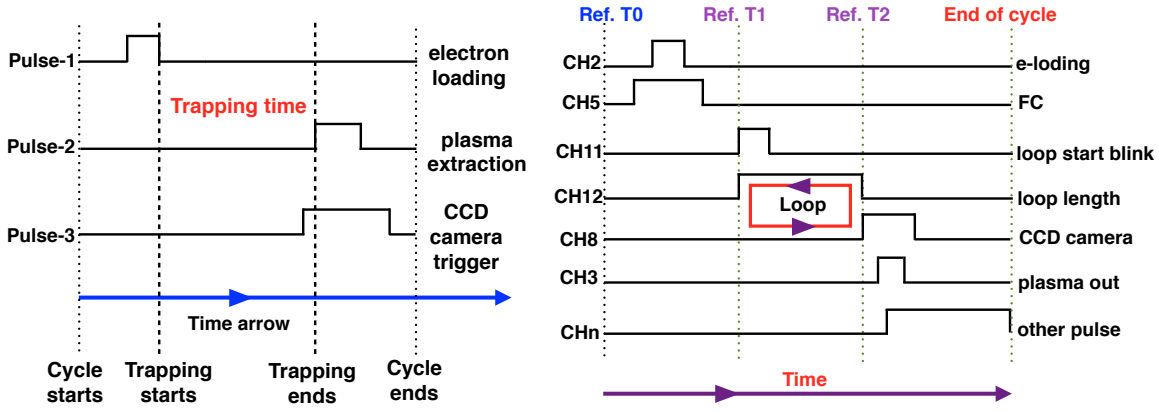

(a) A typical electron loading, trapping and plasma extraction cycle.

(b) Modified PPG cycle for longer trapping time.

Figure 4.16: CPET PPG cycles. The fast high-voltage switching and the precise timing is achieved using CPET PPG.

It was found that the CPET PPG is not capable of setting a delay more than $\sim$ 42 second. As a result, to trap the electron plasma for a longer time, the CPET PPG cycle was modified. For trapping times exceeding 40 seconds a channel is dedicated to loop for a certain number of times to allow this. The process is illustrated in Fig. (4.16(b))

4.7.2 Voltage control, system monitor and interlock

A LabVIEW^{TM} program is used to actuate the detectors, set the potentials at different elements on the beam line including the trap potential and to monitor the vacuum pressure of the system. The user interface is shown in Fig. (4.17).

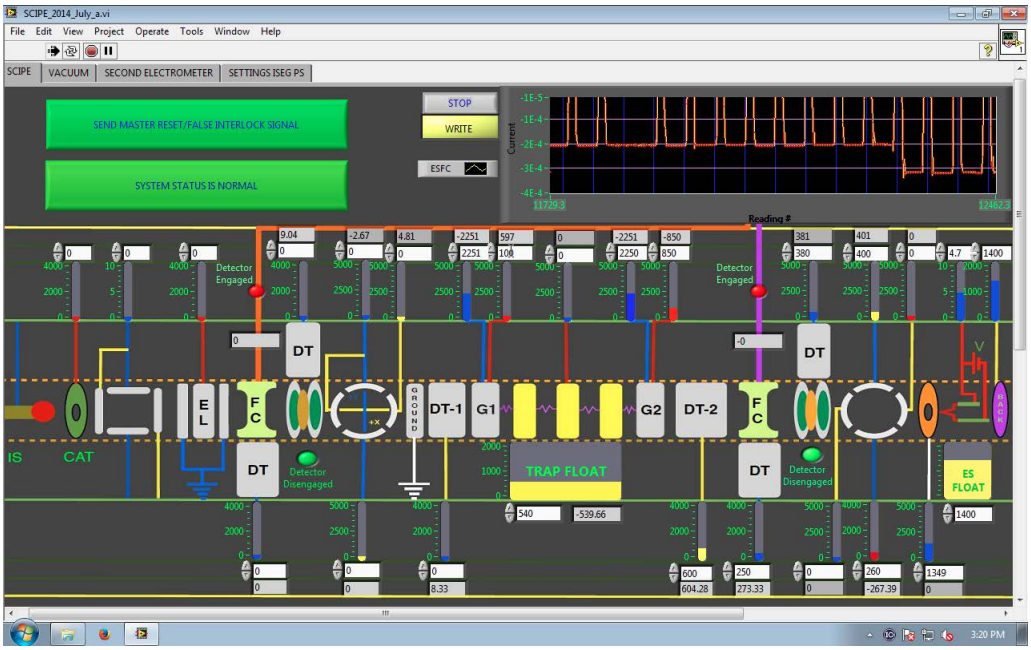

(a) Voltage control and system status monitoring tab.

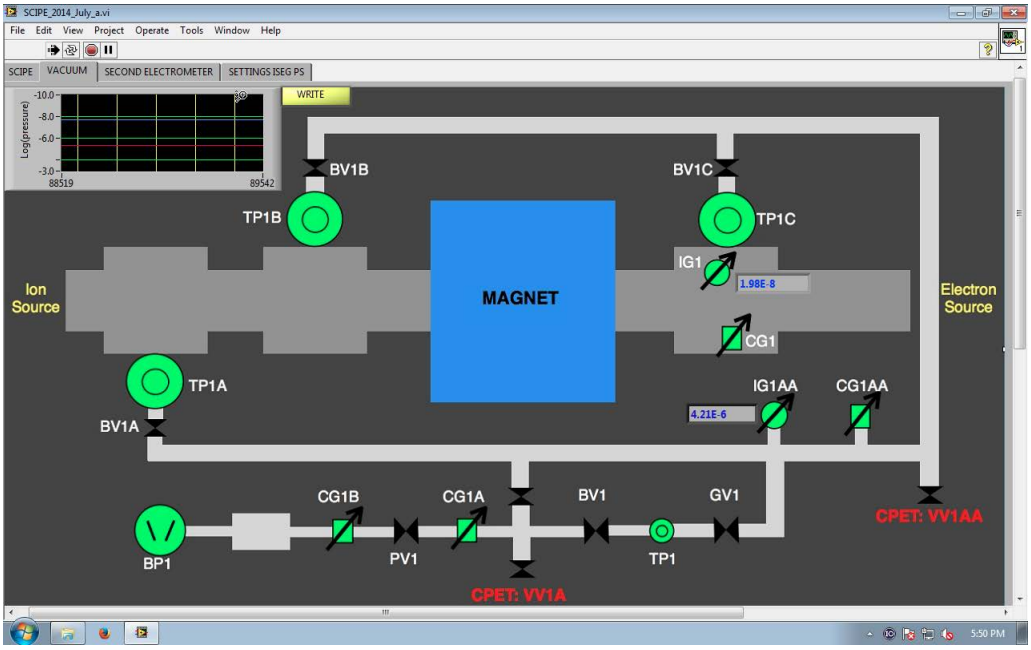

(b) Vacuum monitoring page and recording tab.

Figure 4.17: A LabVIEW program sets the electrode potentials, which are interlocked with the vacuum readout.

The LabVIEW program works as the platform for the control system, using the combination of

a large number of electronic devices including a GPIB-LAN converter which works as a hub for the Keithley electrometer (reads current), and the Agilent switching unit (used for detector actuation, pressure and temperature reading). The control system's response time is below 1 second, and the high fast ($\sim$ 100s of nano seconds) voltage switching are done using CPET PPG as discussed above. The images below show some of the CPET electronics that are used to control the system and for data acquisition.

(a) The Keithley electrometer (bottom) is used for current reading. Agilent DAQ module (middle) is used to control the Faraday Cup and Micro-Channel plate actuators and also to read the vacuum pressure and system temperature (useful during the baking of the system).

(b) A pulse generator (top left) is used to trigger CPET PPG externally. High quality iSeg power supplies (top) are used for the electrodes where low noise power output is required. Control hub (bottom) is used to connect different electronics to the PC.

Figure 4.18: Major components of CPET DAQ and control system with some of the power supplies in CPET electronics rack.

While setting up a rectangular potential well is technically simpler compared to a harmonic potential well, a harmonic potential well can confine the electron plasma for significantly longer period of time [122]. However, at TITAN, the goal is to cool short-lived radioisotopes with half-lives in the range of hundreds of milliseconds. Even $\sim$10 of seconds of plasma life time is sufficient to cool the highly charged ions after which the reloading of the trap with electrons can be repeated.

Also, the electron plasma at room temperature is going to expand significantly in diameter by continuous collision with residual gas [128] after several minutes [122] which will eventually require applying a rotating wall compression [129] while the loss of electrons over time continues. This infers that a long time plasma confinement (beyond a few minutes) is not a major advantage over reloading of the trap with electrons for our purpose. Considering all these aspects, we decided to use a rectangular potential well for the initial plasma systematic tests. In the next chapter we discuss some of the important results.

Chapter 5

Systematic studies of CPET

The purpose of the offline test is to make sure that when the cooler Penning trap (CPET) is commissioned, minimal effort is required from the experimenters to operate it. This necessitates the reproducibility of the trap's loading, trapping and extraction and the study of the characteristics of the electronics, vacuum and the mechanical systems. In this chapter we discuss some of the important initial systematic tests of CPET. We propose some modifications to improve the system's performance, especially for the detectors, to facilitate the offline tests, so that we can have an efficient and reliable detection system for the online operation.

5.1 Electron source and transmission efficiency

Once all the electric and electronics systems were ready, after the system was pumped down to a pressure of $\sim 2 \times 10^{-8}$ Torr, the first test we did was the transmission efficiency of the electron beam. Any small problem with alignment of the trap with the 7 T magnetic field contributes towards the electrons reflecting back even before reaching the high-field region by enhancing the mirror effect which will be discussed below.

When charged particles propagate from a low magnetic field region to a higher field region, the

field gradient prduces a force of the form:

$$F_z = -\frac{1}{2} q v_\perp r \left(\frac{\partial B_z}{\partial z} \right). \tag{5.1}$$

Here, $v_\perp$ is the transverse component of particle velocity, B_z is the axial component of the magnetic field, r is the cyclotron radius of the particle at axial position z and q is the charge of the particle.

Using Eq. (5.1) it can be shown that the condition for the magnetic mirror effect is given by

$$\frac{v_\perp}{v_{||}} > \sqrt{\frac{B_{min}}{B_{max}}}, \tag{5.2}$$

where $v_{||}$ is the parallel component of the particle velocity and B_{max} and B_{min} are the fields at the source and the centre of the trap. This shows that above a certain ratio of transverse to parallel component of particle velocity, the particle will reflect back. Even if a particle travels parallel to the field initially, due to the field gradient, the particles will gain a transverse component down the path unless it is exactly at the centre line of the field as shown in Fig. (5.1).

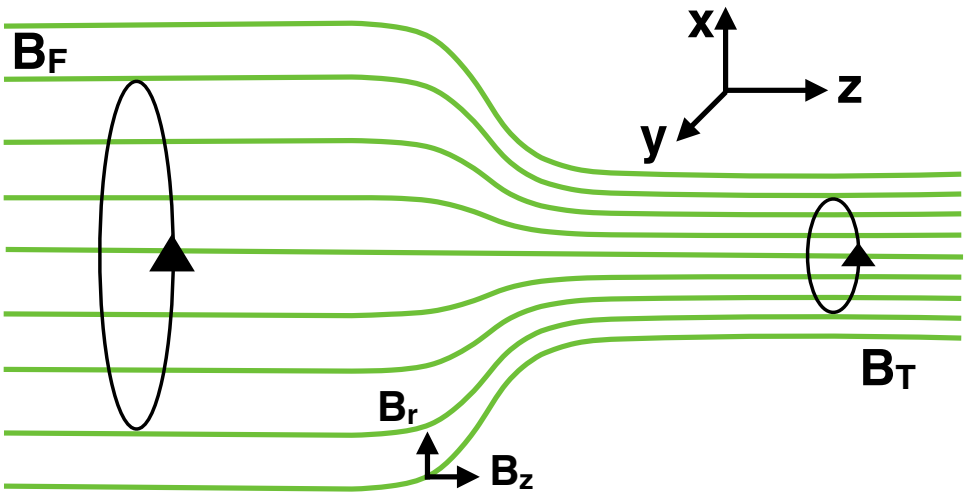

Figure 5.1: Magnetic field gradient responsible for mirror effect. The force on the particle acts in the opposite direction of the motion of the particle. With a sufficient transverse component the velocity could be reversed. Slightly modified reproduction from [130].

The mirror effect could be reduced if an electron source has very small spatial distribution and

is positioned on the magnetic field axis.

Considering the simplicity and the point-like nature, a Field Emission Tip (FET) [131] was tested as CPET electron source [1]. The advantage of using a FET are many. It is easy to install, being a field emission source, the tip does not affect the UHV, which is very important for CPET, and is easily available. A LabView program was used for conditioning of the tips which protects the source by lowering the bias voltage if the output current exceeds a certain value. Fig. (5.2) shows the program's user interface used for conditioning the tip.

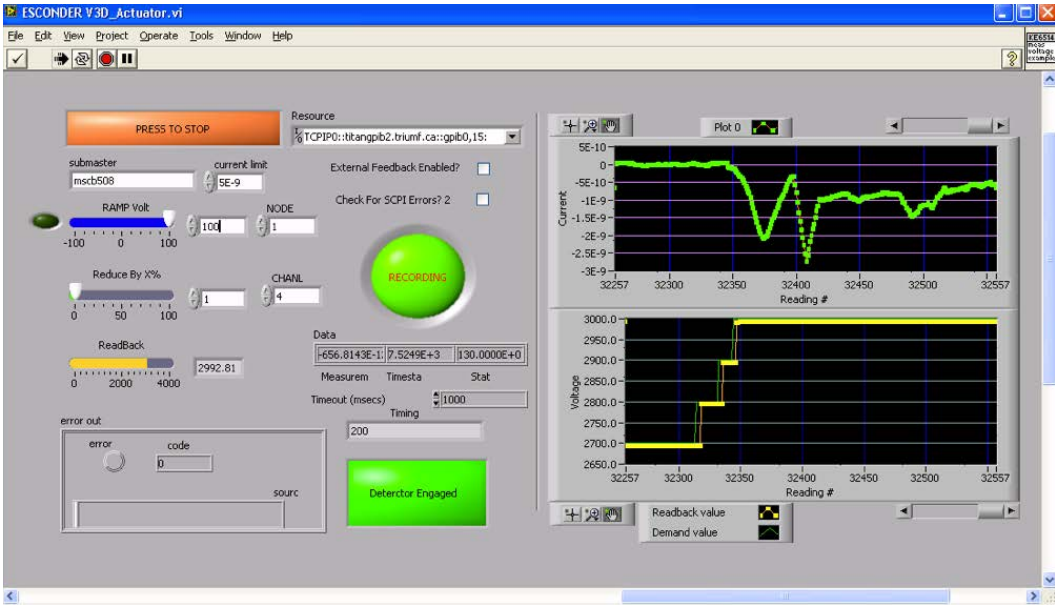

Figure 5.2: LabView program was used to condition the FET and to measure the transmission efficiency.

The tips were saved on numerous occasions from burning as can be seen from Fig. (5.3) during the conditioning process.

Because of the point-like geometry of the tip, a transmission efficiency of up to 100% was observed. However, tests show the unstable nature of the current from the FETs despite a long conditioning time. Fig. (5.4) shows the current profile and the transmission efficiency. To measure the transmission efficiency the current at the entrance and exit of the trap were measured. A digital

[1] The tests were possible because of the collaboration with our friends and authors of [131] at the National Superconducting Cyclotron Laboratory who sent us the tips.

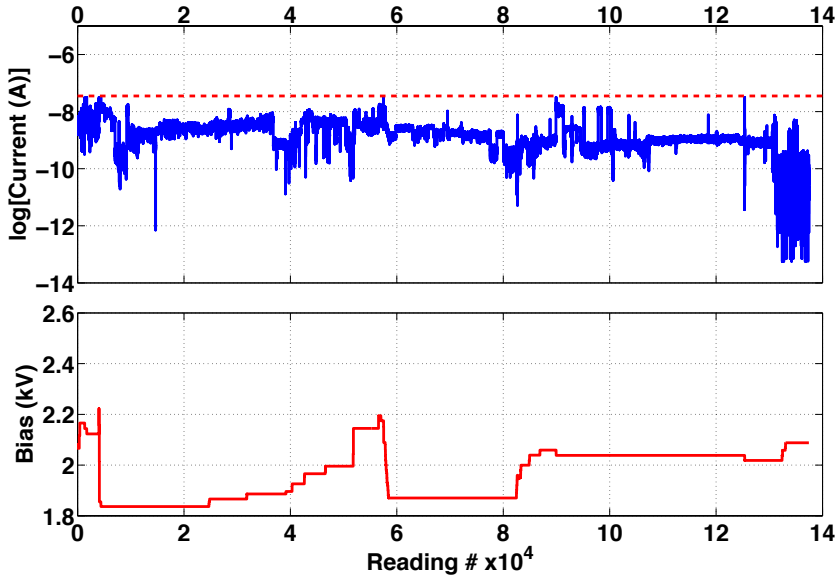

Figure 5.3: A LabView program was used to condition the FET. Whenever the current (figure on top) reaches a set high value (broken red line in figure), the LabView program adjusts the bias (figure on the bottom) to save the tip from damage due to excess current. Here the current limit was set to 5×10^{-8} A).

tag (1/0) was used to differentiate between current reading at the entrance and exit.

In spite of a number of advantages of using the FETs, there are some major drawbacks that forced us to look for an alternative electron source. First of all, they are very sensitive to the applied extraction bias. A momentary rise in current (which are natural for the FETs) can burn them. Some tips never produce electron current as mentioned in [131], but we can know about a tip's current producing ability only after putting the tip in use, by opening the vacuum and applying the bias which is a major drawback. Fig. (5.5) shows the images of three different tips. The tips also produce very little current, only in the nA range (Fig. 5.4 and 5.3) and the current fluctuates over a wide range. This is problematic for the reproducibility of the tests and experiments which makes it almost impossible to establish a tune.

Finally, we concluded that the FETs are not the appropriate source of electron for our experiment and we tested a hot filament electron source.

In comparison, the conditioning and use of the hot filament source is much easier and a single source was used for over one year without any problem. The only major drawback is the heat

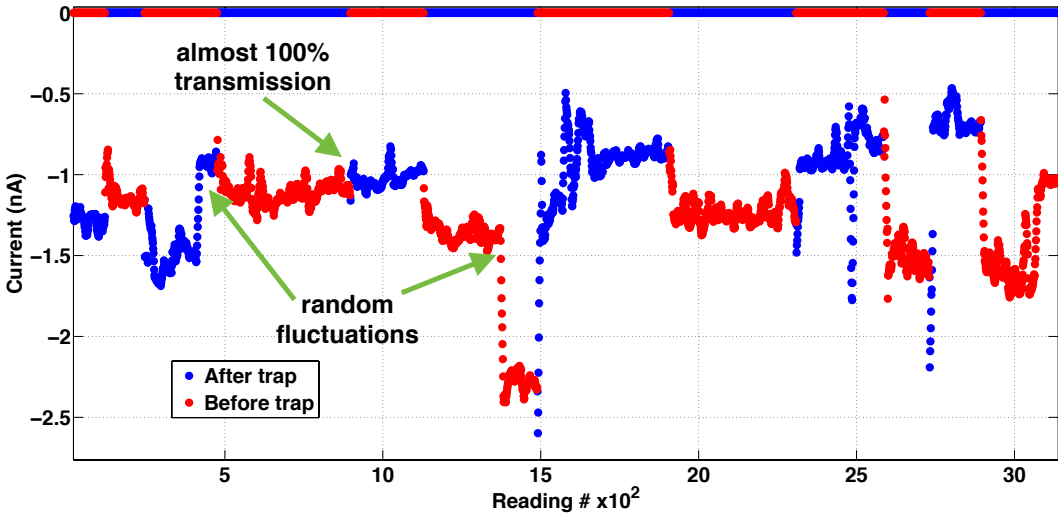

Figure 5.4: Transmission efficiency test of CPET with FET. Occasionally the transmission reached almost 100%. However, the random fluctuations of the electron current makes it very difficult to carry on tests with the FETs.

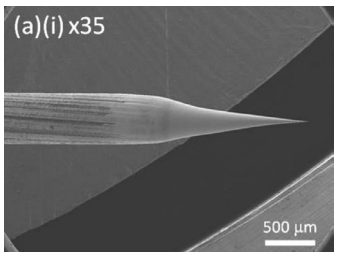

(a) Good tip. Figure from [131]. Image taken with an electron microscope.

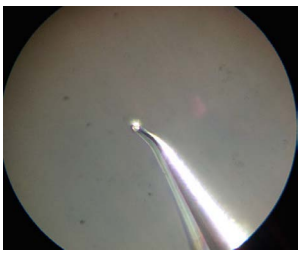

(b) A bad tip. Never produced electrons. Image taken with an optical microscope.

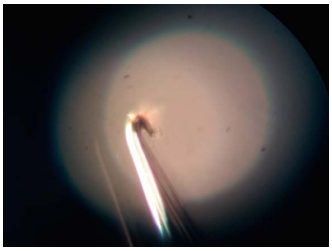

(c) Burned tip. Image taken with an optical microscope.

Figure 5.5: Images of field emission tips (FETs). The damage or a potential problem is sometimes visible even with an optical microscope

generated by a hot filament. This extremely hot filament can make the CPET UHV deteriorate significantly, at least locally. Fig. (4.9(a)) shows the thermionic source used for the tests presented in this thesis. The current from the hot filament is very stable and is usually on the order of μA. The hot filament's brightness causes some problem on CCD images of the plasma (discussed later in this chapter) and the beam is evidently not 'point-like'. An image of the direct beam is shown in Fig. (5.6). This image was taken with the micro-channel plate (MCP) on the electron extraction-end, where the magnetic field strength is almost the same as the value at the electron

source, which means that the initial size of the beam is the same as is detected on the MCP, on the electron extraction end (or the ion injection end). This has the potential for magnetic mirror effect problems as we discussed earlier. However, the loss of electrons due to the mirror effect becomes less problematic due to the large current generated by the hot filament.

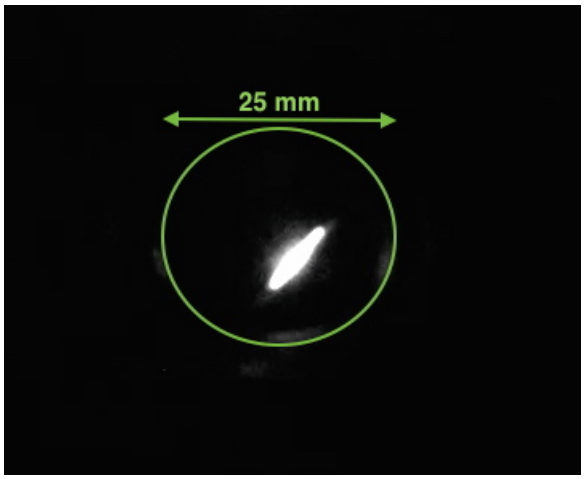

Figure 5.6: A CCD image of the electron pulse direct from the source. The green circle shows the circumference of the phosphor screen coupled to the MCP detector.

As can be seen from Fig. (5.7), the transmission efficiency reached and exceeded 5% for the thermionic source which is sufficiently high for us to conduct our tests and presumably for online use as well.

There are two other aspects of the system that carry a significant importance alongside a reliable source. These are the potential profiles of each element of the system and the power supplies used. The first requires careful design and high quality machining while the second aspect needs using good judgement to decide which power supply is good for what application. A tuneable potential along the plasma extraction line is important to make sure that the plasma or ion can be steered and focused, which is crucial for plasma measurements such as electron number and plasma diameter. CPET does not have a completely controllable extraction line. See Fig. (5.11) for the extraction line of CPET. The feed-through section is completely grounded and, a long section after that has no element at all (i.e only a vacant space surrounded by the beam-line). The power supplies we have are quite stable. The fluctuation is minimal, in the range of mV, except for the ones that are

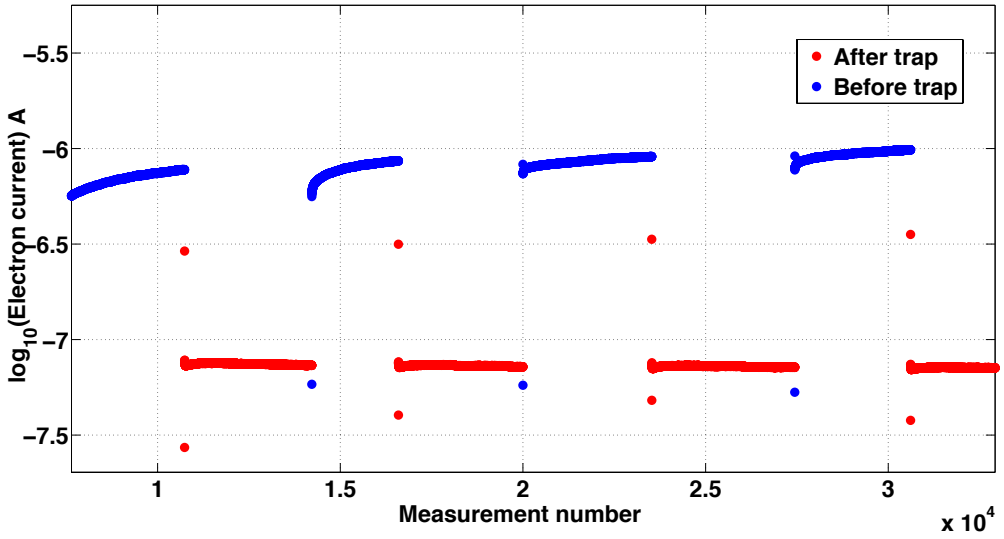

Figure 5.7: Transmission efficiency test result. The current was measured at the entrance and exit of CPET using Faraday cups.

switched. Depending on the difference between the switching voltages, due to the capacitive load, at each extraction the extraction potential varies slightly from the set potential. However, for up to 130 second trapping we did not observe any problem because of these fluctuations. As a result, we did not consider any systematic study focusing on the effect of the stability of the power supplies on the trap operation. A typical arrangement of the power supplies is provided in appendix-A for all elements in the CPET system.

5.2 CPET detectors and the calibration

Every test depends on one or more detectors. Various types of detectors are required depending on the nature of the tests and experiments. As a result, before we go into the details of the tests, it is important to discuss the detection or diagnostic methods and the apparatus we have and some of the problems we experienced in the beginning.

5.2.1 Micro channel plates

CPET has two sets of micro channel plate (MCP) detectors in chevron configuration on both sides of the trap. The MCP detectors are highly sensitive and can detect a single ion. Both the MCPs are

coupled with a phosphor screen and a mirror at 45^{o} which can be used to find the ion or electron position. This helps with steering the ion and electron beams to the right position if required. The CPET MCPs played a major role in the very first tests performed. For tests with ions they will be required again, but for most of the tests reported in this thesis they were not required.

5.2.2 Imaging devices: phosphor screen and CCD camera

The experiment uses a phosphor screen and a Pointgrey CCD camera (model: GX-FW-28S5M-C) that are used to determine the plasma radius and position. The CCD camera is triggerable, which makes it possible to capture images at the moment electrons are extracted from the trap. Recent modifications required us to put the phosphor screen inside the magnet bore which is far from the CCD camera mounting location. Putting the CCD camera far from the phosphor screen makes the solid angle generated on the CCD by the phosphor screen smaller, and thus we have a reduced pixel number for the same detector with increasing distances. To overcome this problem we installed a zoom lens to enhance the image quality and to have more detailed information about the plasma.

5.2.3 Faraday cup and Phosphor screen and their calibration

CPET has one two-sided Faraday cup (FC) on each side of the trap to measure the electron and ion currents. In general, the FC and the phosphor screen do not require calibration, because of their simple design, when reading the DC current (in case of the FC), or to observe the images produced by the charged particles (in case of the phosphor screen). However, if we want to use the FC or the phosphor screen to read charge numbers in a pulse of charged particles, like an extracted plasma, they must be calibrated first. The purpose of this calibration is to relate the electron number to the signal we see on the oscilloscope. For some of the test results presented in this thesis we used the phosphor screen as a FC. For this reason we did a calibration of the phosphor screen by sending DC pulses of known current and length. The method we followed is to relate the area generated by the signal to the charge number. The advantage of this method is that the area of the signal remains the same for same number of charge particles detected for any change in capacitive or resistive nature of the system (RC characteristics).

At first a DC current was measured by using an electrometer. For the calibration presented here, the current was 1.35×10^{-6}A. Using one of the gate electrodes of the trap, the DC beam was then chopped into pulses of 100 to 0.001 millisecond lengths and the corresponding signals were recorded using the oscilloscope (Tektronix TDS-2024C). The signals are shown in Fig. (5.8).

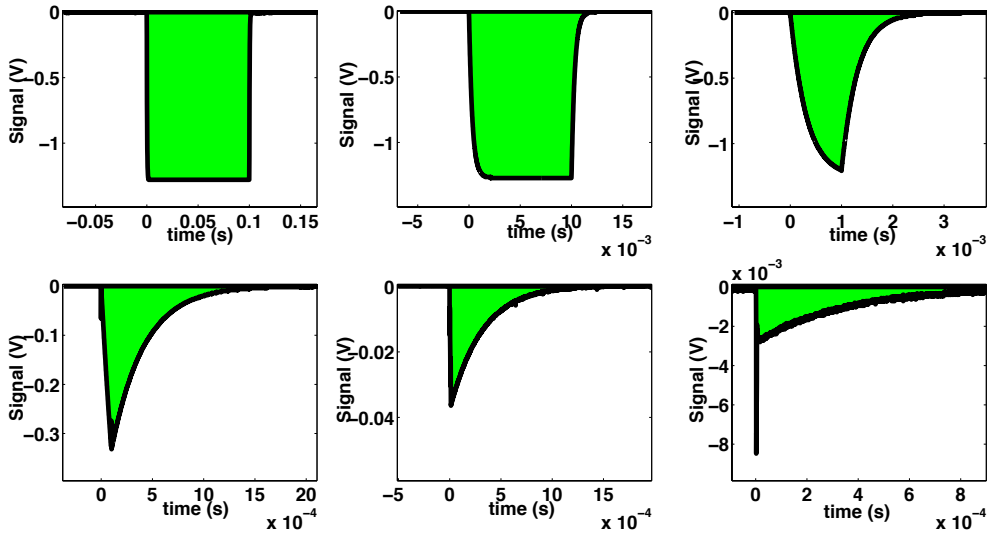

Figure 5.8: Area generated by the signal of DC pulses of different time length.

The area enclosed by the signal is integrated numerically using a Matlab program and then plotted against the pulse length. The real value of the electron numbers is then superimposed on the plotted values of the integrated areas. As the value of the area and the electron number must match, the area values are multiplied by a multiplication factor which we call the calibration factor. For a very low number of electrons ($\lesssim 10^5$) the FC detection may not be possible due to two reasons, the first being the ambient noise. The second reason is the potential switching on the extraction gate electrode, which sends a very strong pickup signal to the FC and overwhelms the real electron signal.

To fix this problem, an amplifier box, made by the detector group at TRIUMF, is used with the FC to amplify the FC signal if it is too weak. The circuit diagram is shown in Fig. (5.9).

Fig. (5.10) shows the overlap of real electron number and the integrated area from Fig. (5.8). Using this method we found the calibration factor to be 7×10^{12}. This number is used to find the

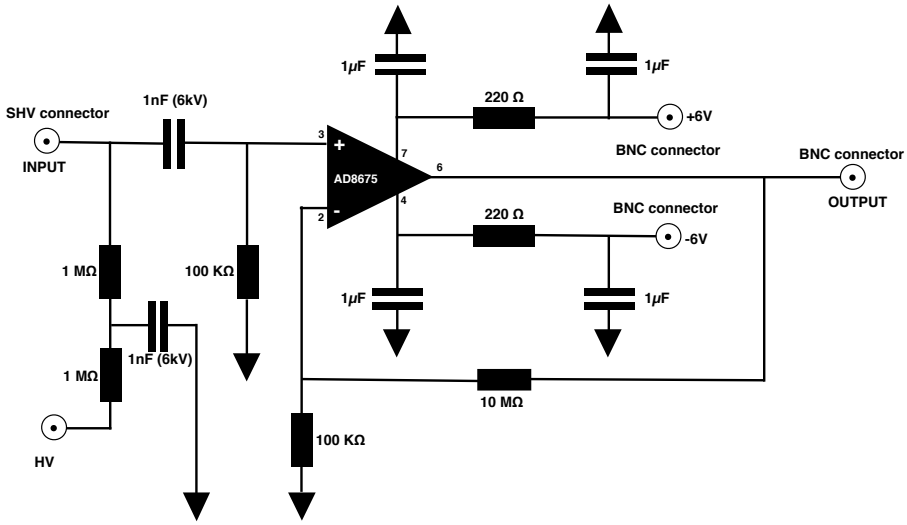

Figure 5.9: Amplifier circuit for electron number detection. For smaller electron numbers the signal will need to be amplified.

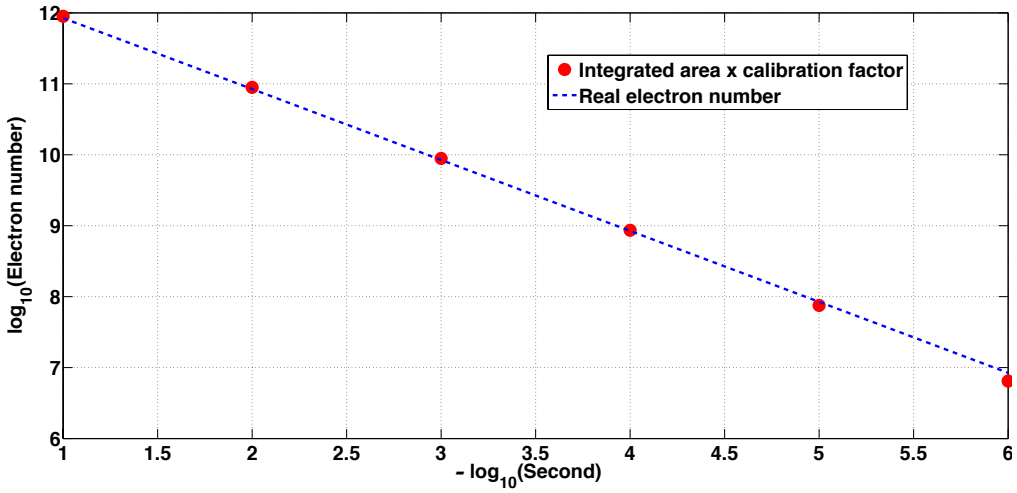

Figure 5.10: Calibration graph. The area generated by electron pulses is plotted against the time length of the pulses. Matching the area to the electron numbers requires a multiplication factor which we call the calibration factor for our system.

electron number in all the tests we performed. The range of calibration was selected such that the number of electrons we expect to trap in the CPET falls within it. This means that the calibration factor is reliable, even if the system does not remain linear (as in Fig. 5.10) over a very wide range.

5.3 Choosing the detector position and size

The detection method we use is destructive, i.e. we lose the particles if we want to detect or count them. Because of CPET being at room temperature, we are not considering the non-destructive methods [132] of plasma (or ion) diagnostics at this moment. The first stage of offline tests involves the electron plasma. The electron plasma detection is more challenging compared to the ion detection. This is due to the fact that the plasma size depends on the magnetic field and its radial position evolves with respect to the magnetic field following the relation:

$$R_{Detector} = \sqrt{\frac{B_{Trap}}{B_{Detector}}} \times R_{Trap}, \tag{5.3}$$

where, $R_{Detector}$ and R_{Trap} are the radius of the electron plasma at the detector location and trap, respectively, and $B_{Detector}$ and B_{Trap} are the axial field strengths of the magnetic field at the detector location and trapping region. Simulations were done to check if the electrostatic potential could be used to focus the expanded beam and be kept within the diameter of the detectors, but it was found that the electrons follow the magnetic field line and only potentials in the range of $\sim$20 kV show some moderate focusing effect if an Einzel lens-like configuration is used. The relation between plasma expansion and magnetic field given by the Eq. (5.3) along the CPET beam-line is shown in Fig. (5.11).

The initial position of the CPET detectors for the plasma detection were too far from the trap center (and in a weak magnetic field) to reliably detect the electron plasma. The expansion of plasma was $\sim$37 times the diameter inside the trap. The situation of plasma expansion is shown in Fig. (5.12).

Our detectors are only 25 mm in diameter, which means that even a plasma with 1 mm diameter

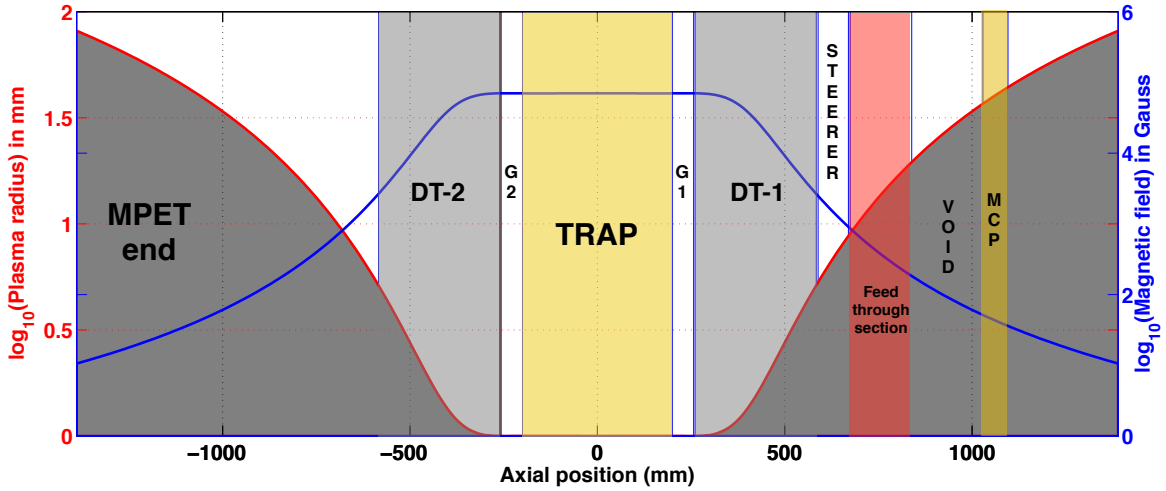

Figure 5.11: Magnetic field on-axis and the corresponding diameter of a plasma of unit radius (here 1 mm). At the detector location the field is only ∼50 mT which means the plasma expands ∼37 times when it reaches the detectors at their original position which is more than 1 m away from the trap center.

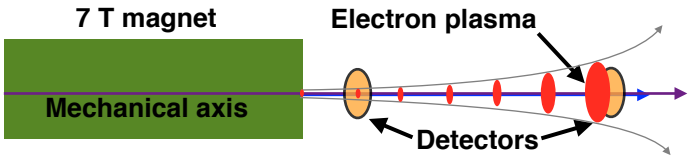

Figure 5.12: Effect of plasma expansion for a perfect trap alignment. If the detector is too far from the trap, even for a perfect alignment (mechanical and $\vec{B}$ field axis) the on-axis plasma may expand too much and the detector may not be able to cover the whole plasma. The blue line indicates the magnetic field axis.

cannot be fully covered by the detectors at their original location. In addition to this drawback, the alignment of the magnetic field with respect to the mechanical axis of the beamline poses another challenge. As the electron plasma follows the magnetic field lines, the plasma may miss the detectors by the time the plasma reaches the position of the detectors. This is shown in Fig. (5.13).

Now, to know how long we can keep the electron plasma confined inside CPET, we require to be able to detect the electron plasma in a consistent manner. To confirm the extent of plasma expansion and the effect on detection, SIMION simulations were performed. It is clear from the Eq. (5.3), Fig. (5.11) and SIMION simulations, that if the plasma would have moved off-axis

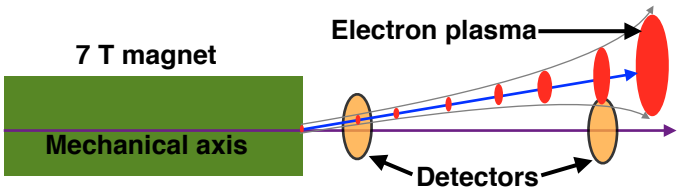

Figure 5.13: Effect of plasma expansion for a imperfect trap alignment. Because of the misalignment, even the on-axis plasma can miss or only be partially captured by the detector. If the detector is brought closer to the trap, the same plasma can be detected.

to a fixed position (r, θ), we should still be able to see the plasma consistently hitting exactly the same position on a detector every time, provided that the plasma size and radial position is within a certain limit. The SIMION simulation shows that for the initial detector position, if the plasma column is radially more than 0.3 mm off axis, we cannot detect the plasma (Fig. 5.14).

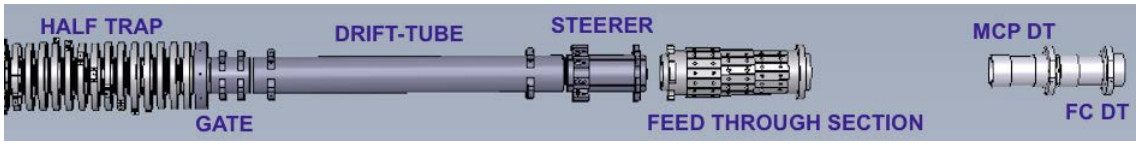

(a) Different elements on the electron plasma extraction line.

(b) On-axis cloud may expand too much and hit drift-tubes before the detector.

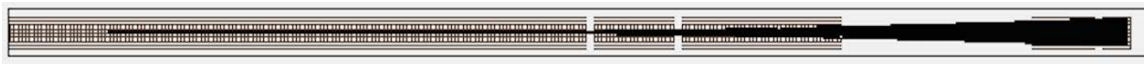

(c) Expansion of the electron plasma in the fringe field. Even on-axis plasma will exceed the detector area if the plasma inside the trap is bigger than 0.34 mm in radius.

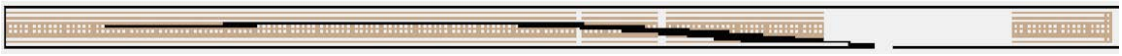

(d) Off-axis (0.5 mm) plasma misses the detector before coming out of the feed-through-section.

Figure 5.14: SIMION simulations for plasma detection. The electrons are generated at the centre of the trap (first segment on the left).

Because of all the issues discussed above — plasma expansion, misalignment, detector size and location — at the beginning we were able to detect plasmas with a very small radius and only when they were at the right position inside the trap. With our best effort we were able to detect only a fraction of the extractions. Fig. (5.18) shows the success rate (ratio of detected signal on

the extraction) of detection. Initially we did not have any testing method to confirm the presence of the $m = 1$ mode of plasma oscillation, which drives the plasma column off-axis [133]. The $m = 1$ mode of plasma oscillation is triggered by misalignment of the trap axis with respect to the magnetic field [134], improper injection [135], image charge effects [15, 120], ions produced from the residual gas species present in the vacuum [136], and also the neutral atoms of residual gases [128]. The motion of plasma under the diocotron mode $m = 1$ is shown in Fig. (5.15).

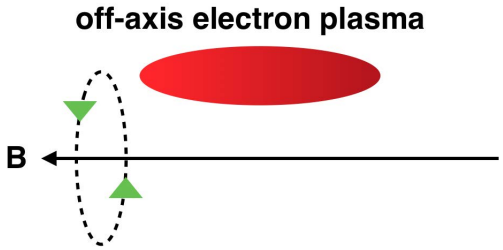

Figure 5.15: When triggered, the diocotron mode drives the plasma away from the trap axis.

According to [136], a very small amount of ions can drastically destabilize the plasma. For small and ellipsoidal plasmas and single charged particles, this mode of motion is also called the magnetron motion and considered to stem from the axial trapping potentials's radial component [15]. Fig. (5.16) shows the result from a SIMION simulation's axial view of the plasma detected and how the off-axis plasma moves on the detector even for a perfect alignment of the magnetic field and the trap axis.

The ELTRAP group successfully stabilized the plasma and damped the diocotron motion in a very straightforward manner [137]. They applied a non-resonant dipole frequency (DF) on the electron plasma that brings the plasma back close to the trap axis. To test this method for CPET plasma, a capacitively isolated DF box was built (Fig. 5.17) to apply DF, and attempt was made to damp the mode presuming its presence.

The initial tests do not confirm the effectiveness of this method for CPET. However, further tests should be conducted before reaching any conclusion. Fig. (5.18) gives an idea as to how unstable the spot is at the detector. More details of the $m = 1$ mode and its study in CPET are given in the next chapter.

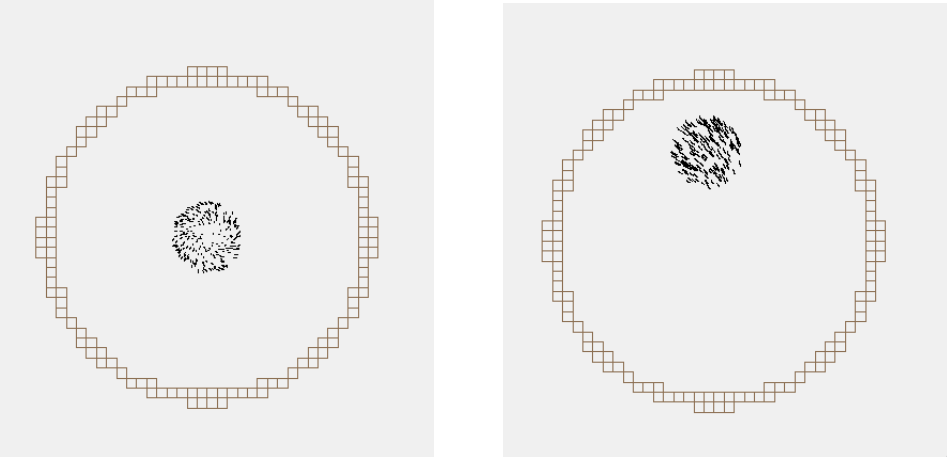

(a) On axis plasma with perfect field alignment hits the detector center.

(b) 0.25 mm off axis (inside the trap) plasma remains within the active detector area.

Figure 5.16: A plasma of 0.1 mm diameter after extraction at the detector of 25 mm diameter.

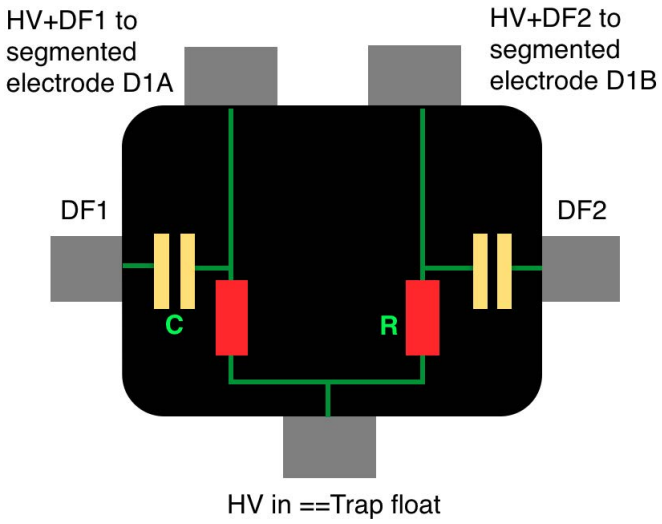

Figure 5.17: High voltage and dipole frequency coupling electronics. DF1 and DF2 are two dipole frequency inputs.

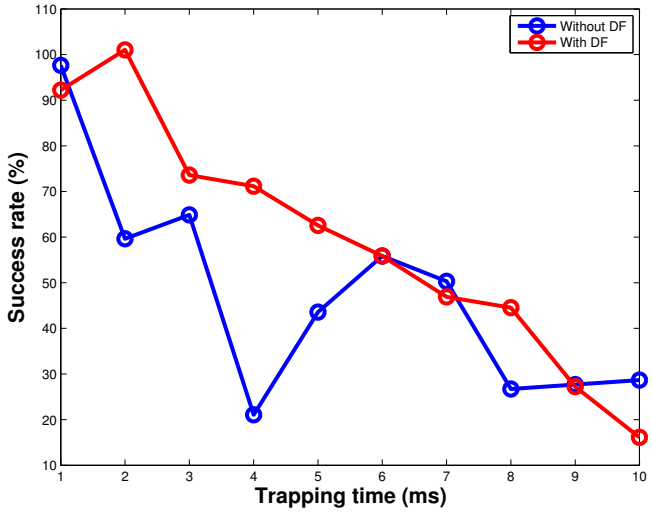

Figure 5.18: Success rate of detection for different trapping times with the MCP at its original position. The effect of applying a dipole frequency was negligible.

To have a quantitive comparison of the CPET detectors with that of other facilities, where multi-ring Penning traps (MRTs) are used, we investigated the details of the detectors in some of them. Here we discuss our findings.

5.3.1 CPET detector position and size comparison with other facilities

To detect the plasma position (radial) and size we need to have the detectors at the most suitable locations. It is also important that the size of the detector is large enough for a particular location, i.e. a detector could be installed far from the trap if the detector has larger active area and other ion optics do not block the area exposed to the incoming plasma or ion beam. Alternatively, a detector of smaller active area could be used, provided the detector is installed closer to the trap. Here we present some examples from other experimental facilities. As every facility has magnets of different geometry, size and strength with different size of detectors with varying distances from the trap centres, it is important to define a meaningful parameter by means of which we can compare the effectiveness of the detectors at each facility. We define the captured area ratio as that particular parameter. The captured area ratio represents *the fraction of area of the trap cross*

Table 5.1: Area covered by detectors at different facilities.

Facility	Diameter of MCP/FC/PS (mm)	Captured area ratio (%)	Beam size amplification at detector	Effective detector area compared to CPET
CPET	25	2	37x	1
RIKEN	26	5	10x	14
ALPHA	41	19	7x	32
ATRAP	25	>60	4x	113
ELTRAP	110	>100	1x	1392

section covered by the detector:

$$\text{Captured area ratio} = \frac{A_D}{A_{ev}} \times 100\%, \tag{5.4}$$

where, A_D is the active area of the detector and A_{ev} is the evolved area of the plasma with a diameter equal to the inner-diameter of the trap at the detector. Table (5.5) summarizes the analysis, and the comparison of CPET detector with other facilities.

For comparison with other facilities, we define the effective detector area compared to CPET as:

$$\text{Eff. detector area compared to CPET} = \frac{\text{Area of a plasma at CPET detector}}{\text{Area of that plasma at detector in other facility}}. \tag{5.5}$$

Fig. (5.19) shows the effective area of the CPET detectors (at their original location) compared to other similar facilities. Only the electron extraction-end detector of CPET was considered in this case. Other detectors that will be used either for electron beam (instead of the electron plasma) or ion detection, this analysis is not required. This is because, the effect of magnetic field is not relevant in those cases.

It is clear from the above analysis that the CPET detectors with their fixed diameters have very limited detector capability at their original positions.

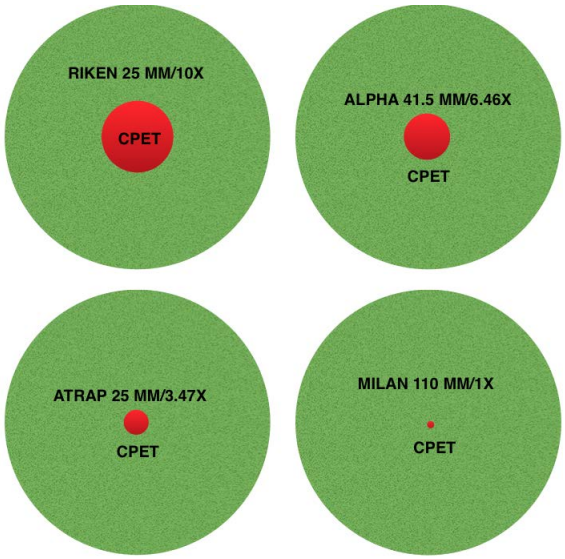

Figure 5.19: Effective detector area comparison. RIKEN[122], ALPHA[138], ATRAP [82], ELTRAP [139] detector's effective areas are shown in green. CPET's effective area is shown in red. This comparison is for CPET's original design detector location.

5.4 Possible improvement of the detection method and detectors

There are two approaches to improving the detection. A short-term or temporary solution and a long term solution that will be useful for the online-operation as well. We tested the short-term solution and demonstrated that the CPET detectors at the original position are not acceptable for plasma detection and need to be moved closer to the trap where the magnetic field strength is orders of magnitude stronger. However, in the short-term solution we installed a phosphor screen inside the DT-1. The phosphor screen assembly reduces the pumping speed partially and blocks the ion path completely. Due to these problems, we are compelled to look for a permanent solution that will allow us to bring the ions into the trap, and at the same time, detect the electron plasma without compromising the pumping speed significantly. In the following we discuss both the short-term and the long-term solutions for the CPET detectors.

5.4.1 Short-term solution for the offline tests

Once we were convinced that the plasma could be seen intermittently because of the $m = 1$ diocotron motion [15, 133], we improvised a quick and less expensive test. We planned to put a simple aluminium holder with a phosphor screen closer to the trap and hence in a stronger magnetic field. The magnetic field at the phosphor screen location is ∼6300 gauss. This means the diameter of a plasma is expanded only ∼3 times on the screen. As a result, a 22 mm diameter phosphor screen is able to cover ∼4.5% area of the trap (about the same value of the RIKEN trap). Considering this advantage, an aluminium holder was machined and put inside the drift-tube on the plasma extraction end (DT-1 in Fig. 5.11). No cable was needed to bias the phosphor screen as the bias of the DT-1 would be the bias of the phosphor screen as well. Fig. (5.20) shows the aluminium holder and its position inside DT-1.

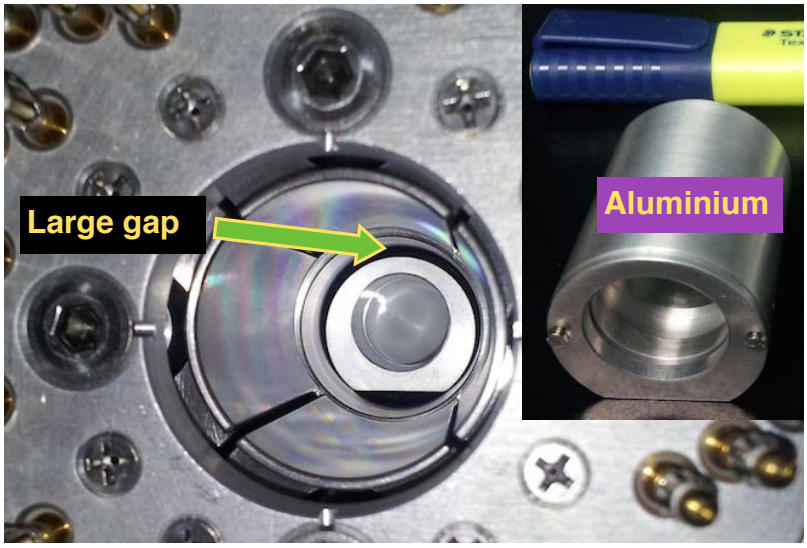

Figure 5.20: CPET phosphor screen/FC. Large gap around the holder was allowing too much light from the electron source. The detector system was also electrically connected to DT-1 (see Fig. 5.11).

With this modification we were able to see immediately that the $m = 1$ plasma motion is in action. Fig. (5.21) shows the sum of multiple plasma extraction cycles on the phosphor screen.

With the help of this modification and some programming changes in the CPET programmable pulse generator (which was previously not able to allow a trapping time over 40 seconds) electron

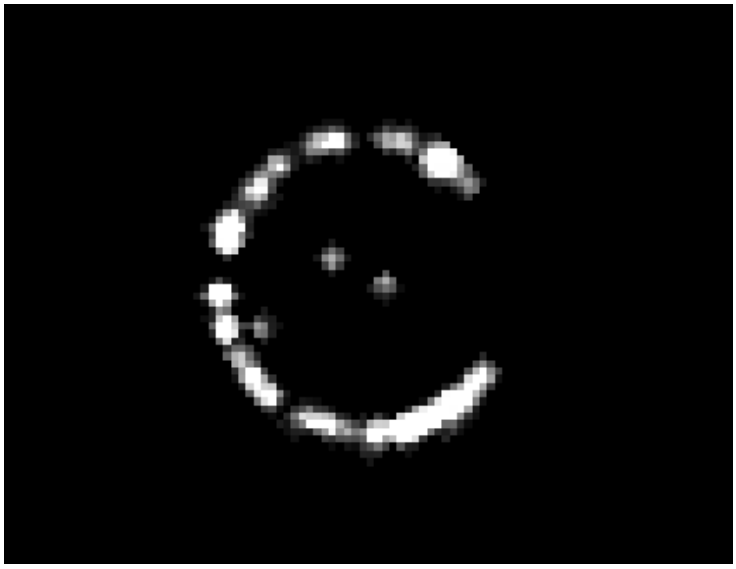

Figure 5.21: First proof that $m = 1$ mode of plasma oscillation is in action. This image is for 1.5 second plasma confinement after noise reduction. 100 individual frames were added to generate the image.

plasma was detected for over 2 minutes of trapping time. Fig. (5.22) shows the plasma spot for 10-130 second plasma trapping.

Despite being able to confirm the long plasma trapping time and the evolution of the $m = 1$ mode, the detector had few major drawbacks. Being inside the drift tube and electrically connected to it, the detector is susceptible to any electromagnetic noise generated elsewhere around the trap that is visible to the drift tube itself. The major source of such noise is the gate electrode (G1 in Fig. 5.11) which is switched to extract the plasma to the phosphor screen. This causes a problem with regard to finding the electron number by reading the charge on the phosphor screen. A lot of effort was made to suppress and/or cancel the noise but the signal-to-noise ratio is extremely low, and any attempt to cancel the noise was reducing the signal below the level of detection. Another problem is the smaller size of the phosphor screen holder and the cut on the bottom which was supposed to act as a reference for the alignment of the screen. After installation we found that the cut and the gap around the holder allow too much light from our electron source to the CCD camera. An attempt to block the bright light was made by putting the FC in the beamline after loading the trap and this improves the image quality dramatically by completely blocking any

(a) 20 second plasma. (b) 30 second plasma. (c) 40 second plasma. (d) 50 second plasma.

(e) 1 minute plasma. (f) 1 minute 30 second plasma. (g) 2 minute plasma. (h) 2 minute 10 second plasma.

Figure 5.22: 20 seconds to 2 min 10 second plasma in CPET. Trap depth was increased during the test to provide enough electrons so that they were detectable on the phosphor screen. Also, some of the images were digitally enhanced to make the images clearer.

background. Fig. (5.23) shows the differences between two images that were taken keeping the FC at the un-engaged position and by putting it in the beam-line and hence blocking the light.

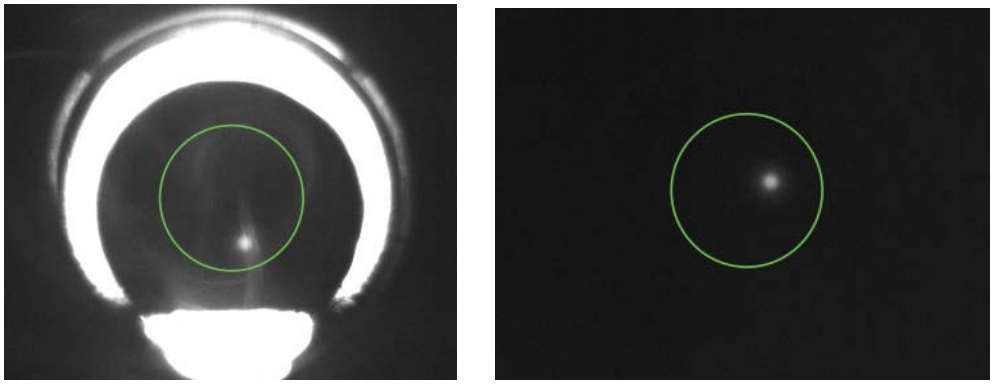

(a) Plasma image without blocking light by FC. The green circle shows the area of the phosphor screen..

(b) Blocking the light by using FC improves the image quality dramatically.

Figure 5.23: Difference between images produced by blocking and not blocking the light from the electron source using the electron injection-end FC.

Although blocking the light with the FC improves the image quality drastically, the repeated actuation of the FC puts a heavy stress on the mechanical assembly system. There were two break-

downs due to the excessive engagement and disengagement of the FC which made us reconsider this option. However, a modification to make the FC assembly more durable is under active investigation. The second drawback with the current position of the phosphor screen is that it is blocking the ion path. This needs to be addressed for the full offline tests and certainly for the online operation. Once we install the ion source, for the full offline test, the detection method must be modified to to facilitate the ion injection.

While efforts are underway to make proper modifications of the system to address both the issues, the first challenge was overcome by using a Macor holder with a larger diameter to block more light from the electron source and at the same time also isolate the phosphor screen from the drift tube. Fig. (5.25) shows the phosphor screen holder and its position inside the drift tube. Fig. (5.24) shows the plasma spot on the phosphor screen with the aluminium holder (Fig. 5.24(a)) and Macor holder (Fig. 5.24(b)).

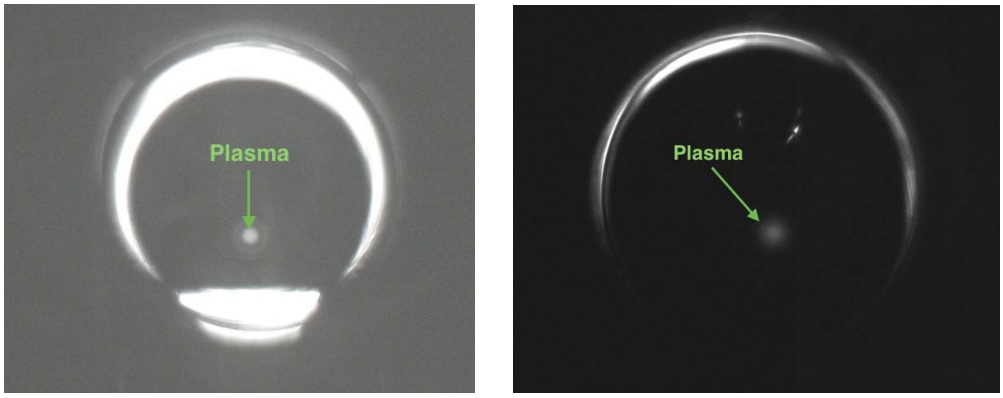

(a) Plasma image with the aluminium phosphor screen holder with 5 kV bias on the phosphor screen. The large bright corona surrounding the screen causes problems for plasma detection.

(b) A plasma image after the holder modification with only 3.5 kV bias on the phosphor screen. The background light was reduced significantly.

Figure 5.24: Plasma image for 1 second confinement before and after replacing the aluminium holder with a Macor holder. With a larger holder diameter, the background light was reduced significantly. Due to the reduction of background light, a lower phosphor screen bias gave a relatively brighter image.

A shielded cable is then used to bias the screen. The shielding of the biasing cable and the drift-tube combined eliminate most of the electromagnetic noise.

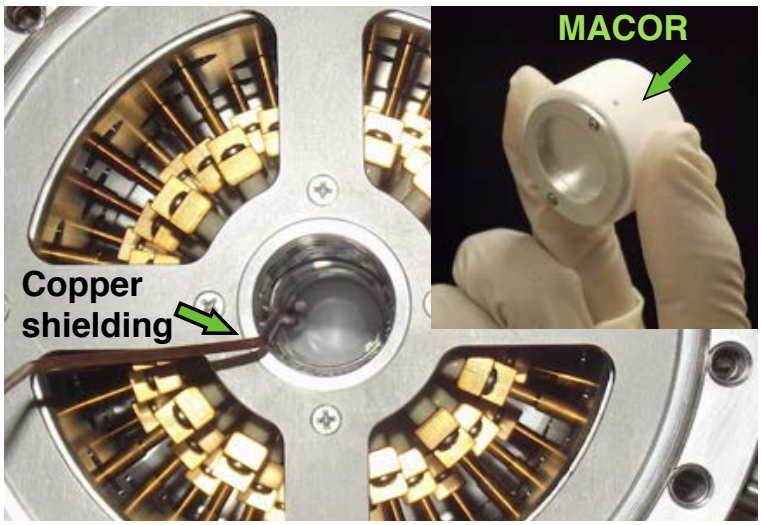

Figure 5.25: Phosphor screen on Macor holder and shielded biasing cable. The shielding reduced the electromagnetic pickup by a couple of orders of magnitude and facilitated the detection of the electron number.

Using the shielded cable, we were able to suppress the nose significantly and a cleaner signal was obtained. In the frequency range of the signal, the noise is negligible. Fig. (5.26) shows the noise and the signal after modification of the phosphor screen.

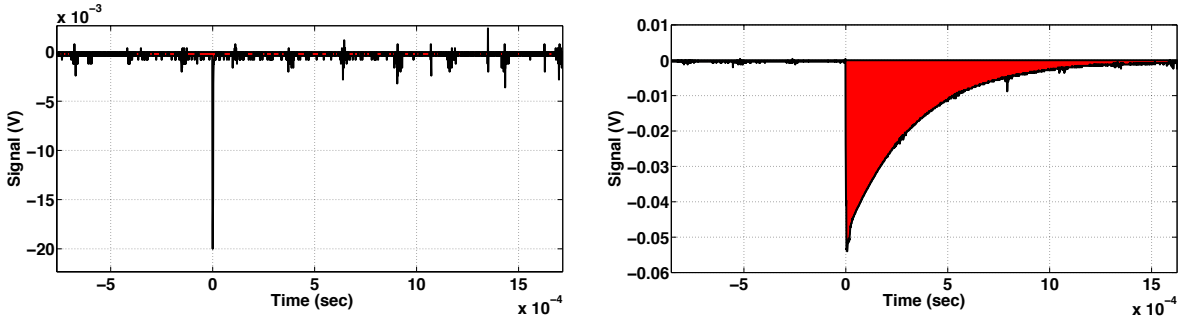

(a) Noise with no electron inside the trap.

(b) Signal with the 1 second plasma confinement.

Figure 5.26: Noise and signal after phosphor screen isolation. Before the modification, differentiating the signal from noise was not possible.

5.4.2 Long term solution for the online-operation

A long term solution is required to detect the electron plasma. During the online operation, we may have to check if the plasma has expanded too much due to collisions with the residual gases in

the vacuum or if it is on axis and having significant overlap with the ions. This information is very important for efficient cooling of HCIs. Without a permanent and suitable detection method it is not possible to acquire this information. Based on our investigation, there are two solutions. The first (and the most straightforward) solution is to move the imaging device and FC assembly closer to the trap. A second solution could be to install high current coils to produce a pulsed magnetic field ($\sim$0.2 T) so that the plasma does not expand beyond the detector area or go off-axis.

Moving the imaging device and FC assembly closer to the trap is the most effective method of plasma detection. This will ensure that the detectors are in a stronger field than where they were situated originally. Fig. (5.27) shows the change in effective area covered by the CPET detectors if moved to right before the feed through section (see Fig. 5.11 and 5.14) compared to where the detectors are located in the original design (Fig. (5.19)).

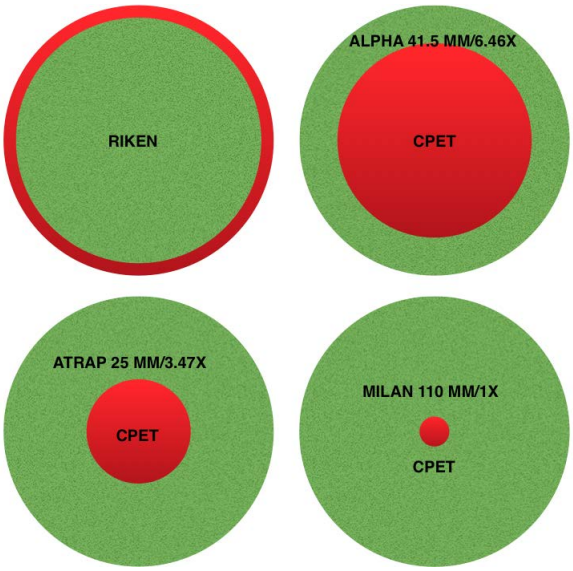

Figure 5.27: Effective detector area if the MCP is moved to the entrance (closer to the trap) of the feed-through-section.

Moving the detector assembly right before the feed-through-section (FTS) will require a new design of the detector-housing-cross and possibly of the FTS as well.

Another solution is to install high current coils to produce a pulsed magnetic field. This method is followed to detect the electrons or positrons in the CUSP trap [81] of the ASACUSA group[140]

at CERN. Although they have a plasma size magnification of $\sim$ 17 (CPET has $\sim$37), it was too large to detect the electrons or positrons, and they decided to use a pulsed high current coil to generate a magnetic field for a very short time ($\sim$ 5 ms) to compress the plasma position and radius so that they are still able to detect them. Due to the high risk of quenching the superconducting magnet by the intense pulses, at this point there are no plans to implement this technique at TITAN.

Currently, a wire grid detector is being tested. Simulations show that the detector could be as high as 50% efficient on ion and electron detection. The detector sits inside the DT-1 but closer to the trap compared to where the test phosphor screens was installed. The advantage of the wire grid detector is that the detector will allow the loading of ions and will be useable during online operation.

5.5 Electron plasma requirements for CPET

CPET will require a very large number of electrons with a very high density to cool the HCIs as we saw from the simulation results in chapter 4. The required ratio of electron number to HCIs is 10^4 for efficient cooling, but generally, the larger the number of electrons, the better the cooling. The electron plasma has to be pre-cooled and this requires it to be loaded into the trap before the HCIs are brought in. The electron self-cooling time is in the range of $\sim$ 80 ms for CPET which is calculated from the formula: Cooling time $\sim 4/\text{magnetic field(T)}^2$ [141, 142]. However, according to Kuroda's thesis (ASACUSA group, CERN), it is 1.5 times longer [143] with some experimental proof [144] based on the theory that the long wavelength radiation is partially reflected back to the plasma from the metal wall of the trap.

5.6 Systematic tests of CPET

For CPET, the ultimate goal is to cool the HCIs that are short-lived and the trap will have to be at room temperature. These requirements dictate the tests CPET must undergo before commissioning it into the TITAN beamline. Here we discuss those essential systematic tests and present the most up-to-date results available. All the tests discussed here involve the electrons. Details of

the numerous tests of the control system, programmable pulse generator, switch boxes, and the integrity of the gold-plated electrodes are skipped.

5.6.1 Loading the trap with electrons

Loading of the trap with electrons is a very important step and the trapped electron number can vary dramatically, based on the method followed. There are three different ways of loading the trap with electrons that we considered: the ballistic mode, the counter propagating electron beam method, and the in-situ generation of electrons using radiofrequency fields.

In the so-called ballistic loading method an electron current is allowed to reflect back from the far end of a trap. As it takes very short time for the electrons to complete a round trip (in the range of $\simeq 0.1\mu$s for CPET), at any time soon after the electrons are allowed to enter, the trap contains an electron beam of twice the trap length. Closing the loading gate traps those electrons. The total number of electrons trapped with this method is:

$$Q = \frac{I \cdot 2L}{\sqrt{(2E/m)}} \times 1.6 \times 10^{-19}, \tag{5.6}$$

where I is the electron current, L is the length of the trap, E is the electron energy and m is the electron mass. With a $\sim 100\ \mu$A electron beam of about 1kV energy, the total number of electrons that can be trapped is $\simeq 10^6$. As we can see, the trapped electron number in this method is proportional to the electron current generated by the source. The duration of loading does not have any effect on this loading scheme. A slightly different mode of ballistic loading is to send pulses of high current electrons which is basically the same procedure as the one mentioned above, but the segmentation of the beam would be done by an electrode other than the trap or gate electrodes. This ballistic loading process is shown in Fig. (5.28(a)).

A different method was used at RIKEN to load the trap where the incoming electrons are scattered by the outgoing electrons, and as a result the scattered electrons get trapped [145]. In this scheme of counter-propagating beam interaction, a large number of electrons ($\simeq 10^{10}$) can be trapped, and unlike the ballistic method, the number of electrons can be controlled by varying the

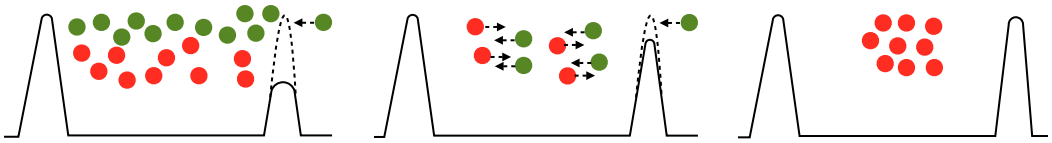

(a) Ballistic loading method. The beam finishes a round-trip inside the trap and is cut-off by the loading gate.

(b) Counter propagating beam scattering off each other and getting trapped.

(c) In situ electron generation. Electron are generated inside the trap.

Figure 5.28: Different loading schemes and the gate potentials. The dotted line shows the gate-closed positions after electron loading is stopped. In Fig. (5.28(a)) and (5.28(b)), the red coloured dots indicate the ions that are travelling to the right, after reflecting back from the gate opposite to the loading gate. In the in situ electron generation method the gate remains closed (Fig. 5.28(c)).

loading time. The process is illustrated in Fig. (5.28(b)). Implementing this method is simple and does not require any hardware modification or extra tools compared to the ballistic mode. The loading is controlled and optimized by adjusting the entrance-gate potential.

A radically different way of electron accumulation was reported by the ELTRAP group [139] where they were successful on generating electrons from residual gas present in the trap by means of applying an RF in segmented electrodes. A small number of electrons from the residual gases work as the seed electrons and the applied RF makes them repeatedly collide with the gas molecules and release more and more electrons. In this method both of the gate electrodes remain closed as it is shown in Fig. (5.28(c)). The major advantage of this method is that there is no need for any independent electron sources or to transport the electron into the trap. The existing trap electrodes of CPET can be used to generate electrons inside the trap. This option of in situ electron generation is under active consideration for CPET.

Clearly, the ballistic method requires a very high current source for sufficiently large numbers of electrons. However, considering the simplicity, the initial plan for CPET was to use the ballistic method. The injection gate was kept at a much lower potential compared to the potential suggested in the RIKEN publications for the counter-propagating beam scattering scheme, but the trapped electron number was found to be significantly higher. The only viable explanation could be that some electrons are scattered by the counter propagating beams and are getting trapped. From this

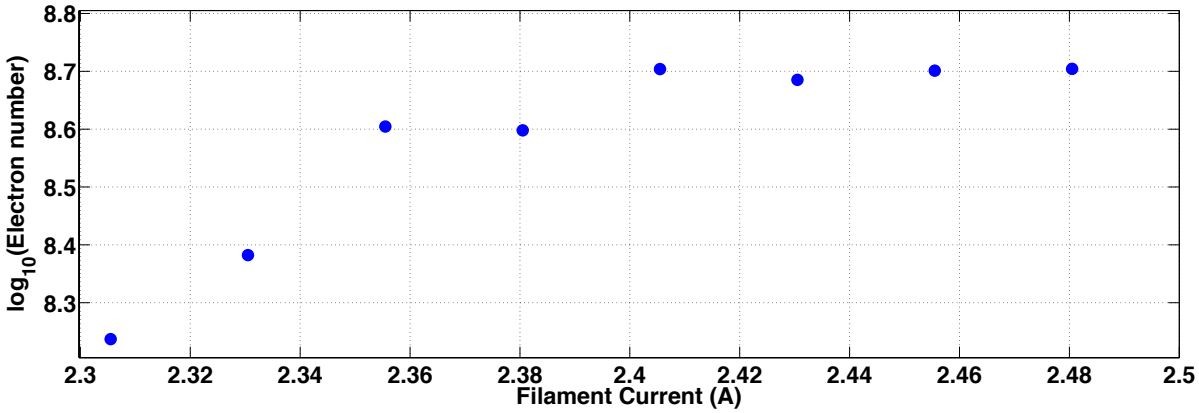

Figure 5.29: Trapped electron number as a function of filament current.

observation we concluded that, in CPET, a combination of the ballistic and the counter propagating beam methods is facilitating the accumulation of a large number of electrons.

5.6.2 Trapping for different electron current

Due to the misalignment, the mirror effect, and potentials at the trap and the gate (G2 in Fig. 5.11) electrodes during loading, a large number of electrons are lost. As we use a thermionic filament as the electron source, it is important to investigate the plasma properties (density, radius etc.) for a range of filament currents, and from the results, we can determine the electron current requirements. While too high a current through the filament can worsen the vacuum and reduce the life span of the source, too little current generates a very small number of electrons to be trapped. We did a systematic test to study the effect of filament current on trapped electron number. The test shows that within the current range suggested by the filament manufacturer, we are able to trap enough electrons ($> 10^8$). The electron number as a function of filament current is shown in Fig. (5.29).

5.6.3 Electron trapping for different potential depths

Trap depth is defined as the potential difference between the trap electrodes (V_T) and the electron source (V_S). The deeper the trap the more electrons can be stored. Similar to the case of injection current, there is a space charge limit for a given trap depth, for which we can say that the trap has

saturated. For CPET we conducted a test with the full trap capacity (all 29 electrodes were used for trapping). The result is shown in Fig. (5.30).

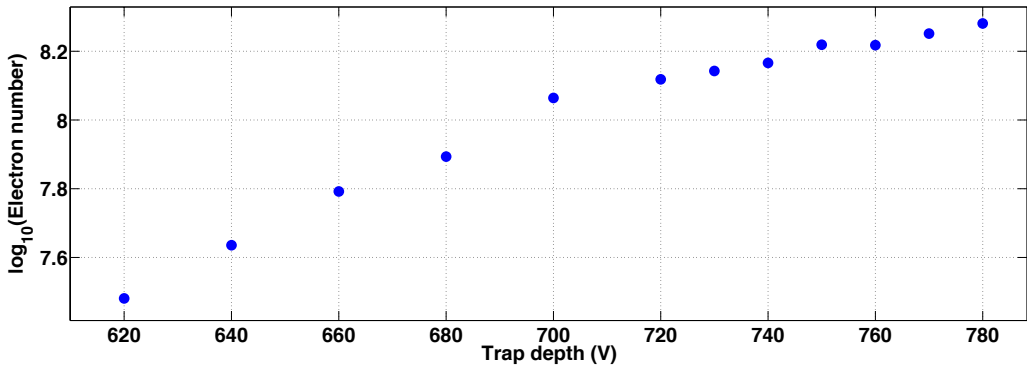

Figure 5.30: Trapped electron number as a function of the trap depth (V_T-V_S).

From the result we can see that the electron number consistently increases with the trap depth and approaches the saturation, as expected [146].

5.6.4 Analysis of CPET electron plasma properties

The research area of plasma physics is very rich, and non-neutral (plasma dominated by one kind of charged particles) magnetized (presence of a significantly strong magnetic field that has effects on the plasma) plasmas are complex physical systems. A detailed discussion of plasma is beyond the scope of this thesis. However, we were able to analyze some of the basic and relevant plasma properties in CPET which we will present in this section.

It is relatively easy to confirm electron accumulation and confinement of a certain duration, but determining whether the electrons formed a plasma requires more detailed analysis. The first step in the plasma analysis in a Penning trap is to confirm that the plasma is spheroidal. To confirm the spheroidal shape of the plasma, the radial intensity profile is studied.

At first we plot the intensity of the plasma as a function of the radius to construct a 3-dimensional plot which gives an immediate visual confirmation of the plasma shape. Fig. (5.31) shows the intensity plot for electron plasma trapped for 1 to 5 seconds in CPET. The radial intensity for a

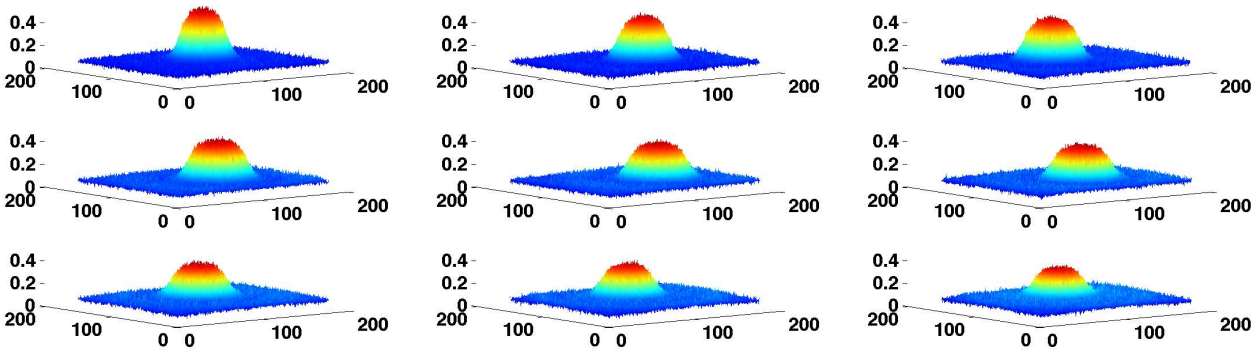

Figure 5.31: 2D projection of the radial intensity profile of the electron plasma for trapping times of 1 to 5 seconds.

spheroidal plasma is given by

$$I(r) = I_0 \left[1 - \left(\frac{r}{R_p}\right)\right]^{\frac{1}{2}}, \tag{5.7}$$

where, I_0 is the peak intensity or the maxima, R_p is the plasma radius and r is the radial position at which the intensity $I(r)$ is measured. To fit Eq. (5.7) to the intensity profile we take a vertical slice through the center of the 3D plasma images shown in Fig. (5.31). The vertical slices (of one pixel width) for each plasma spot of Fig. (5.31) are shown in Fig. (5.32).

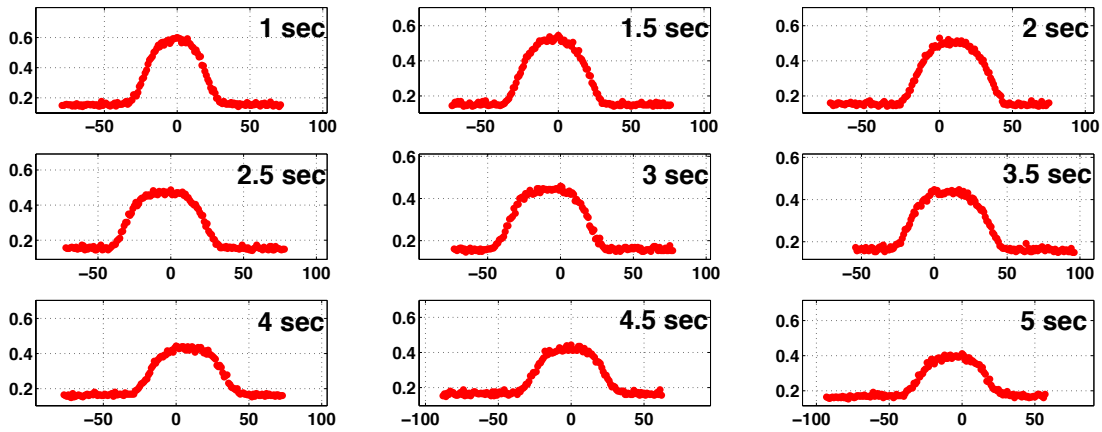

Figure 5.32: Intensity slices generated by taking the radial values from Fig. (5.31).

All the plasma extractions show a very good fit to the equation. One such fit is shown in Fig. (5.33).

All the lengths are initially determined in the unit of pixels. To find the plasma dimensions in

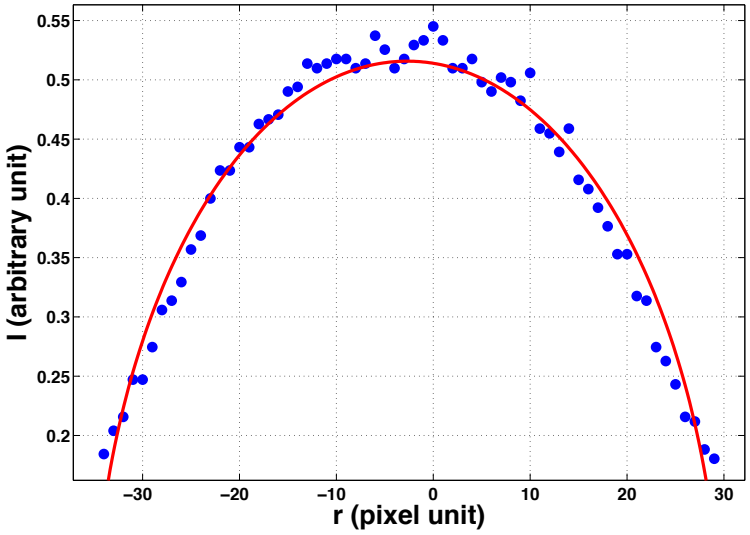

Figure 5.33: A spheroid fit based on the intensity slice following the procedure outlined in [122]. This particular fitting was done for a plasma of 1.5 second trapping time.

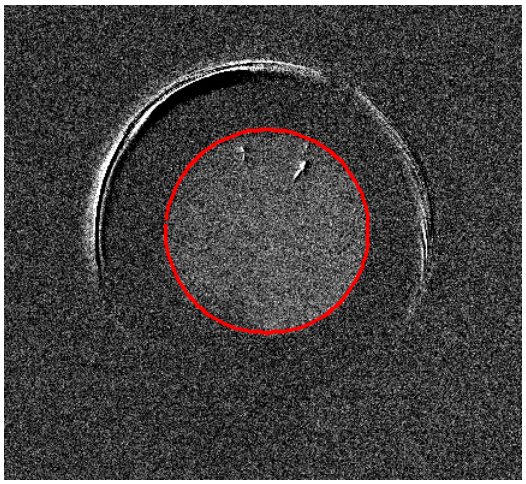

Figure 5.34: Phosphor screen size is related to the pixel width using this CCD image. The radius of the red circle covering the whole phosphor screen active area is 470 pixel units in diameter. This corresponds to the 22.22 mm diameter of active phosphor screen area.

S.I. units the conversion factor needs to be determined. To do so, we trapped a very large number of electrons with large plasma diameter so that the cloud covers the whole phosphor screen. The active area diameter of the P20 type phosphor screen is 22.22 mm. Once the size of the phosphor screen is determined in the pixel unit, it is straightforward to find the conversion factor.

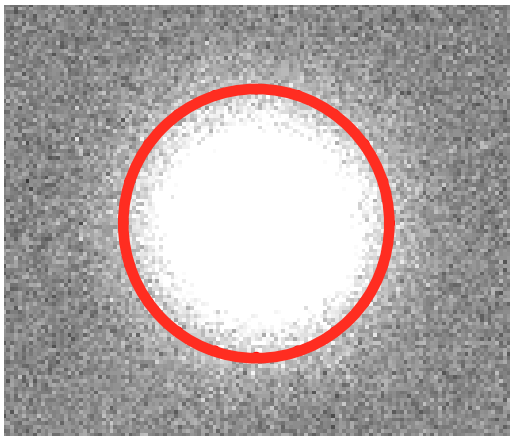

Figure 5.35: A circle is fitted by enhancing (5x) the CCD image to find the full radius of the plasma. Radius of the red circle is 35 pixel units or 35/21.2 mm.

From the circle fitted in Fig. (5.34) we find the conversion factor to be 21.15 pixels per mm.

Once we know the conversion factor, together with Eq. (5.3) which gives the plasma expansion at the detector to be 3.33 times that inside the trap, we can study individual plasma sizes as shown above. The final conversion factor for the dimensions of the plasma and the diocotron mode inside the trap comes out to be 70.44. As a result, the radius of the plasma inside the trap is found to be 0.496 mm for the CCD image shown above.

5.6.5 Electron number for varying trapping time

For the 1-5 second range of trapping time, we had an average of $\sim 1.6 \times 10^8$ electrons trapped. For lower trapping times ($\sim$1-2 second) the diocotron radius is larger and in some of the extractions the plasma missed the detector but was counted as an extraction by the oscilloscope. As a result, the 1-2 seconds data shows fewer electrons compared to the subsequent higher trapping times. Fig. (5.36) shows the electron number for 1-5 second trapping duration. With decreasing diocotron diameter less of the plasma is missing the detector and for this reason the electron number consistently increases up to 2 seconds at which point all the electrons are successfully captured by the detector. We also notice that when the plasma is consistently hitting the detector (because of the smaller diocotron radius), within the time interval under consideration, the electron number does not decrease significantly. This is a very important finding for CPET operation. From this

we can conclude that we can complete multiple cooling cycles for a single electron loading (as we discussed in the chapter 4) once CPET is online.

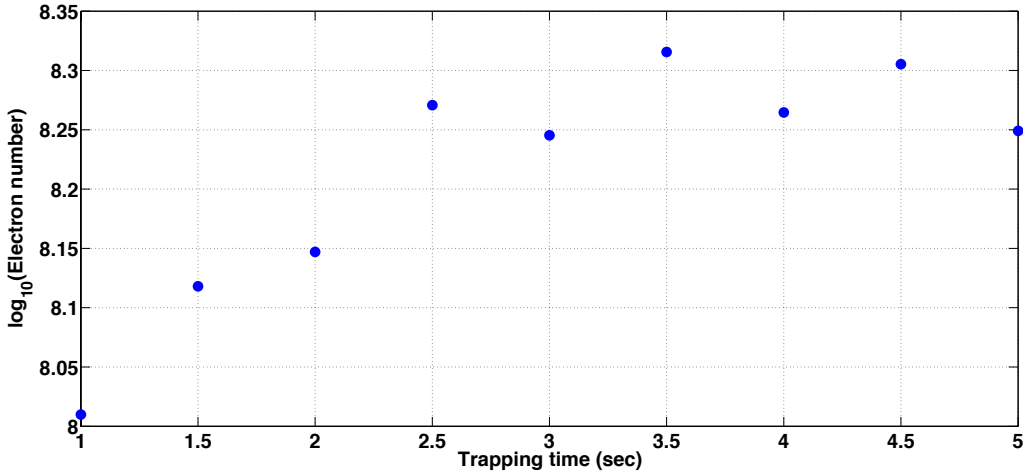

Figure 5.36: Electron number as a function of time in CPET. A total of 64 extractions are averaged. Some of the 1-2 second extractions were hitting outside the phosphor screen but still averaged and this caused the total electron number to seem low.

Now, from the electron number and plasma volume, we can find the electron density of the CPET plasma. The density for a spheroidal plasma is given by

$$\rho = \frac{N}{V} = \frac{N}{\frac{4}{3}\pi r^2 \frac{L}{2}}, \tag{5.8}$$

where V is the plasma volume, r is the plasma radius and L is the trap length. Using the above information we find the electron density in CPET to be $8.12 \times 10^5/\text{mm}^3$. This is consistent with the density found at other facilities [122].

5.6.6 Debye length of the CPET plasma

In plasma physics, a very important parameter to find is the Debye length of the plasma. We used the electron numbers (N) found in the tests mentioned above to calculate the electron density and the Debye length at room temperature (T=300 K). Being a large ensemble of particles, all the particles in plasmas do not experience the same field strength. The Coulomb interaction law of inverse square is replaced by a sharp cut-off due to the screening effect. This cut-off length is

called the Debye length given by:

$$\lambda_D = \left(\frac{\varepsilon_0 k_B T}{\rho q^2} \right)^{\frac{1}{2}}. \tag{5.9}$$

The Debye length comes out to be 4.2×10^{-2} mm which is much shorter than our plasma length (400 mm) and radius ($\simeq$ 0.5 mm). This is an indication that the electron cloud has reached the plasma regime [147].

5.6.7 Plasma intensity for varying trapping time

For the same 1-5 second duration of trapping, the peak intensity (intensity at the center of the plasma image) of the plasma image was studied. From Fig. (5.37) we can see that the intensity of the plasma decreased by $\sim$30% over this time interval. As we saw in the previous test, the electron number did not decrease significantly over the trapping duration under consideration.

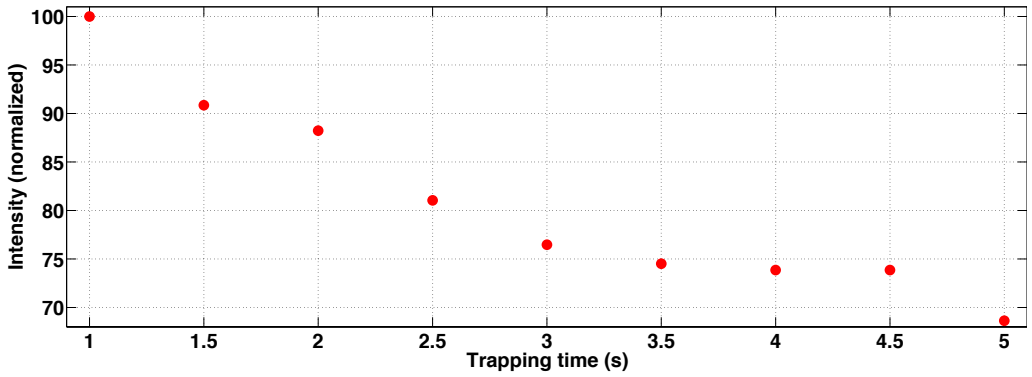

Figure 5.37: The peak intensity as a function of time. The peak intensity was found to drop by $\sim$30% over the 5 second period.

It is not clear to us as to why the intensity decreases while the electron number is not. One possible reason could have been the expansion of the electron plasma. However, from the data collected, we saw that the radius also does not increases significantly. A radially nonuniform potential at the phosphor screen surface can cause such intensity decrease. It is possible that the longitudinal plasma mode is also damping and the reduced axial velocity at extraction is resulting in the reduced intensity. A third reason could be the heating of the CCD camera. In some places a cooling system is used to stabilize the temperature which we did not implement [148]. In any

case, to reach any viable conclusion, further tests are required.

5.7 Conclusion

We performed a number of very important systematic tests and the results are summarized as follows. A good transmission of electrons through the trap, almost ∼50% through the high field gradient was observed. For the HCIs we need to perform the cooling operation within a fraction of a second. The confirmed trapping of up to 130 seconds indicates that we will be able to perform multiple cooling cycles by a single loading of electrons which is very convenient. Results from the systematic tests show that we have at least 10^8 electrons in the trap. In the nested traps, even if we trap orders of magnitude fewer electrons, we will still be able to cool 100s of HCIs. The plasma density we have is excellent and the plasma does not expand significantly within tens of seconds which indicates that the cooling process can go uninterrupted without reloading or applying the rotating wall compression. Day to day reproducibility of all the tests we reported here is also satisfactory. Representative tunes of the system with all the values at electrodes and PPG timings are provided in Appendix A.

Despite the success mentioned above, a lot of systematic tests are yet to be performed. We still do not know the full details of the loading scheme we have, whether the counter-propagating beam method is the best option for CPET [135, 145] loading or not, especially when the electron source is moved off-axis. Determination of the frequency and amplitude of the RF to compress the electron plasma by means of a rotating electric field [85] might be necessary in case we have significant plasma expansion in the smaller nested traps as discussed in chapter 4.

A significant amount of effort is required on the tests mimicking the online setup. This will include establishing an off-axis electron source, testing the ion transmission, trapping and extraction. After the individual tests of load-trap-extract cycles for electron and ions, the simultaneous trapping has to be tested. In the final step, an artificial energy spread will be introduced among the singly charged ions to test the cooling.

Our understanding of the $m = 1$ diocotron mode of plasma oscillation [149–151], which is an

azimuthal drift of the form $e^{im\theta}$ [152], and its damping will play a major role in the cooling of the ions in CPET. It will be important to confirm the overlap between the plasma and the ions inside CPET. Considering the importance of this mode and the interesting phenomenon we observed, the next chapter is dedicate to the $m = 1$ diocotron mode damping.

Chapter 6

Damping of the $m = 1$ plasma oscillation mode

Non-neutral plasmas or single component plasmas are interesting for a number of reasons. The study of different kinds of plasma waves and instabilities [147, 153, 154], production of antimatter [87, 138], and transport properties of plasma [155] are some continuously developing fields. For TITAN's cooler Penning trap (CPET) [16, 119] the application of plasma is close to that of antimatter production: to cool the charged particles. Unlike the singly-charged antiproton in case of antihydrogen production, CPET will cool the HCIs as discussed earlier. For successful cooling of HCIs, we will need a consistently well-defined (density, shape, radial position etc.) plasma for each loading-trapping-detection (or reloading) cycle. For this purpose, CPET is currently being tested offline. During the offline tests we observed that the $m = 1$ diocotron mode is decaying and becoming fixed on the phosphor screen within 3-5 seconds. In this chapter we present the details of our findings which are in good agreement with the magnetic damping, for which the theory was developed and the phenomenon subsequently observed in a modified betatron by Robert and Rostoker three decades ago [156].

6.1 $m = 1$ mode of plasma oscillation

Different plasma oscillation modes were studied extensively by Levy [133], Briggs [157], Driscoll [120, 158], Surko [121], Fajans [159] and others [29]. Levy was able to show that most of the normal modes damped easily by Landau damping [160]. The damping of $m = 1$ mode of plasma oscillation is of particular interest because of its azimuthal properties. The $m = 1$ mode of plasma oscillation, which is an $\vec{E} \times \vec{B}$ drift of the whole plasma column around the trap axis is shown in Fig. (6.1(b)) [15]. For a single charged particle in the Penning trap this motion is known as the magnetron motion [15]. Fig. (6.1) shows the modes of of plasma oscillations in a Penning trap. This motion gives a lot of information about the plasma properties. It is a result of broken

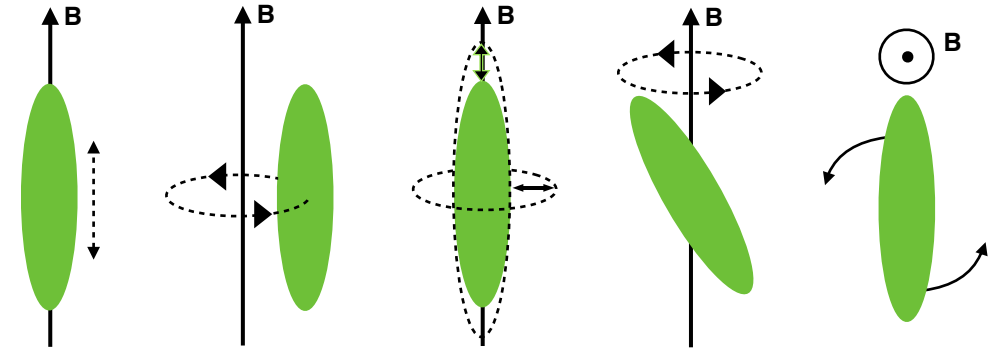

(a) (1,0) (b) (1,1). (c) (2,0). (d) (2,1). (e) (2,2).

Figure 6.1: Oscillation modes of plasma in a Penning trap [26, 147, 154, 161]. The first two modes ($l = 1, m = 0$ and $l = 1, m = 1$) are called the center-of-mass modes because of the oscillation of the center-of-mass.

azimuthal symmetry that may stem from the misalignment of the trap axis to the magnetic field [134], presence of a small number of ions due to the presence of residual gas in the vacuum [135], a radially asymmetric trap potential [162], or from off-axis injection. Once triggered, the motion is sustained by the image charges produced on the trap wall [15]. Depending on the purpose of plasma accumulation, this phenomenon could be an advantage or an obstacle. For plasma physics studies, this could be a way to study different plasma phenomena including a non-destructive diagnostic tool for plasma frequency and trapped particle number [163, 164]. For other experiments where the plasma is used to cool antiprotons [83, 165] or highly charged ions [16, 55], this could mean a

reduced performance of the trap as the orbit of the plasma and antiproton may not overlap at all. In that case a feasible way of damping the mode becomes a necessity.

It has long been known that the $m = 1$ mode of plasma oscillation has negative energy [157, 166], which implies that any power dissipation would increase the amplitude of that oscillation [156]. Experimental proof of this evolution of the mode is given in the work of White, Malmberg and Driscoll [166]. However, the energy of the $m = 1$ mode can also be positive if the plasma has enough axial energy [156]. The axial motion can generate a perturbative magnetic field, which in turn interacts with the trap field. Because of this interaction the energy of the system decreases and the amplitude of the $m = 1$ oscillation should decrease. A detailed theoretical description of the field produced by the plasma is discussed by Roberts and Rostoker in [156].

The ELTRAP group has shown that the motion could be damped by means of applying a non-resonant dipole frequency on radially split electrodes [137]. In other facilities an axial non-resonant field is applied [139] to damp the mode. In their detailed theoretical [167] and experimental work [168] Crooks and Cluggish were able to show how due to rotational pumping the mode is damped but the momentum is conserved. Work by Marler and Stoneking shows that the diocotron mode exists and the $m = 1$ mode decays even in a toroidal trap [169]. In the toroidal trap the electrostatic energy is dissipated through heat energy due to the collisions among the electrons. For the theory for the damping of $m = 1$ diocotron mode in a toroidal trap see [170]. These works together with the works reported in their references and the work of Roberts and Rostoker show a clear compatibility of the theory for Malmberg Penning traps and confinement in toroidal systems (trap or accelerator). On the other hand, Sarid, Gilson and Fajans in their work [171] were able to show that the $m = 1$ mode can decay because of the asymmetry of the trap where momentum is not conserved. They concluded that the damping is the result of the field misalignment and could be observable for small plasma potentials. There is no theory available to date to explain the energy dissipation mechanism for this damping. Roberts and Rostoker [156] showed that the motion could be auto-damped in a modified betatron. This damping mechanism is called magnetic damping and

requires the following condition to be met:

$$\left(\frac{v_z}{c}\right)^2 > \left(\frac{r_p}{r_T}\right)^2, \tag{6.1}$$

where, v_z is the axial velocity of the electron plasma, r_p the plasma radius, r_T is the trap's inner radius and c is the velocity of light.

From the above discussion it is clear that from a conservation of momentum point of view the auto damping can be of two types, one in which the momentum is conserved and one in which it is not. Both the work of Sarid, Gilson and Fajans (Penning trap) [171] and Roberts and Rostoker (modified betatron) [156] show the auto-damping of the mode where momentum is not conserved. While Sarid's experiment was performed in a Penning trap, in the work of Roberts, they used a modified betatron (axial motion) or a section of it (beam rotation). Due to the geometry of the modified betatron presented by Roberts and Rostoker, the setup can be considered very close to that of a Penning trap. In both setups (modified betatron and the cylindrical Penning trap) an axial magnetic field is present which causes the damping. The difference is the end potentials in the Penning trap that facilitate the trapping. Also, in a Penning trap the electric field could be a uniform one for rectangular wells [122] if the trapping length is significantly long (400 mm for CPET) relative to the trap radius (35 mm for CPET). This fact encouraged us to study the theory of Roberts and Rostoker. Despite this assumption of similarity, Sarid's work can not be tested against the theory proposed by Roberts and Rostoker as Sarid's experiment does not meet the axial velocity condition given in Eq. (6.1).

In their work, Roberts and Rostoker gave the formulation for two different kinds of magnetic damping [156]. The first is due to the axial motion of the plasma and the second is due to the rotation of the plasma. Fig. (6.2) shows the the two scenarios. In the first case (Fig. 6.2(a)), the axial motion generates a poloidal magnetic field which is perturbed by the betatron's field and also, the field generated induces current in the wall of the accelerator and thus an ohmic energy dissipation of the form I^2R occurs. In the second scenario (Fig. 6.2(b)), they accelerated the

electron plasma in a section of the accelerator with magnetic field gradients on both ends. The field gradient induces the mirror effect [130, 172] which causes the beam to rotate and thus produces the axial magnetic field which in turn interacts with the accelerator's magnetic field and the wall in a similar fashion. We are not interested in the second scenario as the Penning trap's trapping

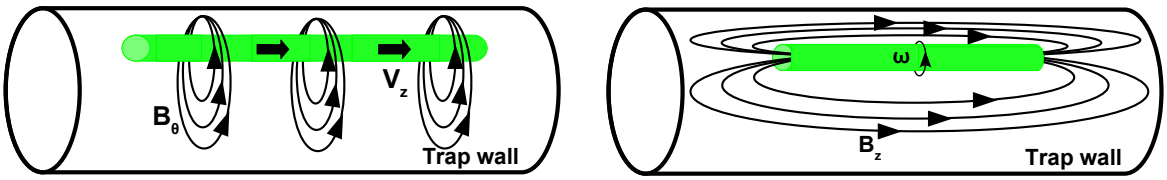

(a) Magnetic field generated by the axial motion of the plasma. This motion produces a poloidal field which interacts with the trap's strong field and also generates a resistive effect in the trap wall.

(b) Magnetic field generated due to the plasma rotation. CPET does not have any way to drive the plasma rotation and hence is not considered.

Figure 6.2: Two possible ways of perturbative fields generated by electron plasma. Modified figures from [156].

region has a predominantly uniform magnetic field and thus the magnetic mirror effect that is used to trigger the rotation of the beam is not present.

For a plasma with a very small radius compared to the confining wall, the damping rate in the work of Roberts and Rostoker is given by the following relation:

$$\Gamma \cong -\frac{2\omega(r_p/r_T)^2(\delta/r_T)}{[1-(r_p/r_T)^2(c/v_z)^2]}, \tag{6.2}$$

where, δ is the skin depth of the trap material (gold-plated copper for CPET) given by $\delta = (2/\mu_c\omega\sigma)^{1/2}$, σ is the conductivity of the plasma, and the plasma frequency ω is given by:

$$\omega = -\frac{2Nec}{B_z r_T^2}\left[1-\left(\frac{v_z}{c}\right)^2\right]. \tag{6.3}$$

To relate the work of Roberts and Rostoker to the tests in the Penning trap, the axial velocity or the center of mass mode oscillation has to be very high so that the condition in Eq. (6.1) is met. The details of the plasma oscillation mode is discussed thoroughly by Dubin [149] and Tinkle [153],

from which we find the axial oscillation of the plasma to be:

$$\omega_z = \left[\frac{qV_0}{md^2}\right]^{1/2}, \tag{6.4}$$

where, V_0 is the potential difference between trap electrodes and the axial confinement voltages, d is the characteristic constant of the trap (0.20 m for CPET). For more discussion on the axial oscillation of non-neutral plasma see [132] and the references therein. Using the above relation we find that the centre-of-mass mode axial oscillation (Fig. 6.1(a)) of electron plasma in CPET reaches the range of 100-106 MHz, which, when transformed into the axial velocity at the centre of the trap, does meet the damping condition given in Eq. (6.1) (so does the average velocity. However, given the length of CPET, the field inside the trap is far from being a quadratic field and the electrons are injected into the trap with a velocity which also meets the condition in Eq. (6.1). This could mean that the plasma maintains the initial velocity and oscillates in a field which is uniform over a significant length or alternatively, the oscillation frequency is high enough to induce the magnetic damping. We are not sure which mechanism plays the major role in damping the $m = 1$ mode.

6.2 Setup details

CPET's hot filament electron source floats at -1400V potential and produces a current of 10s of μA. Fig. (6.3) shows the loading, trapping and extraction potential setups. The trap is loaded continuously for about 300 ms and then the trap is closed. When closed the trapping potentials at both ends of the traps are at -2100 V. Although -1700 V completely blocks the beam, to be on the conservative side, we decided to make the trapping potential a safer -2100 V. During the loading process, the entrance gate is set at -850 V. The switching between -850 V and -2100 V might have some influence on giving the plasma an axial kick. The details of this effect are not studied yet. The trap itself floats at -620 V to -520 V allowing an overall trapping potential of 1480-1580 V. After trapping for a desired period of time, the electron plasma is extracted to a phosphor screen which also operates as a Faraday Cup. A CCD camera is triggered to capture the image on extraction. For

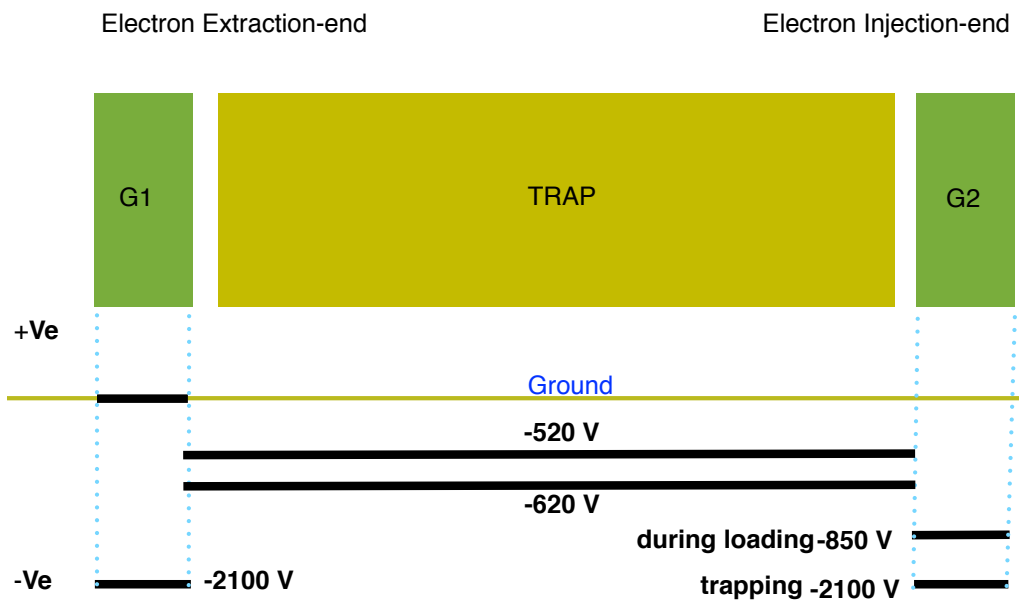

Figure 6.3: Trap potential scheme. During loading the entrance gate is kept at -850V. During extraction the extraction gate is switched to 0 V or to a small positive potential.

higher statistics, each trapping cycle is repeated about 100 times. With 880-780 eV electrons and the 7 T field of CPET, we were able to meets the condition 6.1 reported in the work of Roberts and Rostoker. Fig. (6.4) shows the damping of the $m = 1$ mode in CPET with half-second intervals.

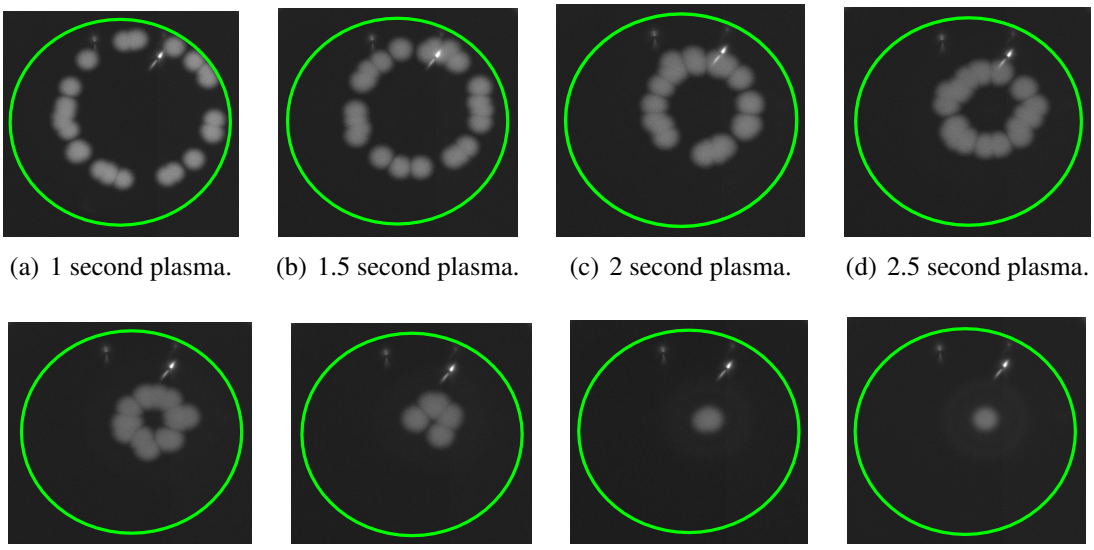

(a) 1 second plasma. (b) 1.5 second plasma. (c) 2 second plasma. (d) 2.5 second plasma.

(e) 3 second plasma. (f) 3.5 second plasma. (g) 4 second plasma. (h) 4.5 second plasma.

Figure 6.4: Damping of the $m = 1$ plasma mode in CPET. The green circle shows the circumference of the phosphor screen which is 22.22 mm in diameter. The trap depth for this data set was 780V.

6.3 Data analysis and results

Tests show that a high density plasma was formed in CPET and that within the observation period of 1-5 seconds the number of electrons does not change significantly. The plasma radius increases slightly over the same time period. Also the trapped electron numbers and radius of the plasma are significantly larger for the deeper trap (820 V). Fig. (6.5) shows the result of the tests. Fig. (6.6)

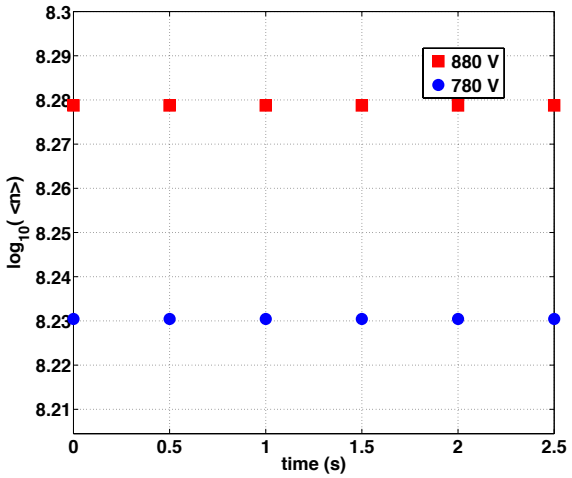

(a) Electron numbers for the two different trap depths (880 and 780 V). Electron numbers remain largely unchanged over the observations period. The first few observation showed slightly fewer electrons due to the large diocotron amplitudes which make the plasma miss the detector.

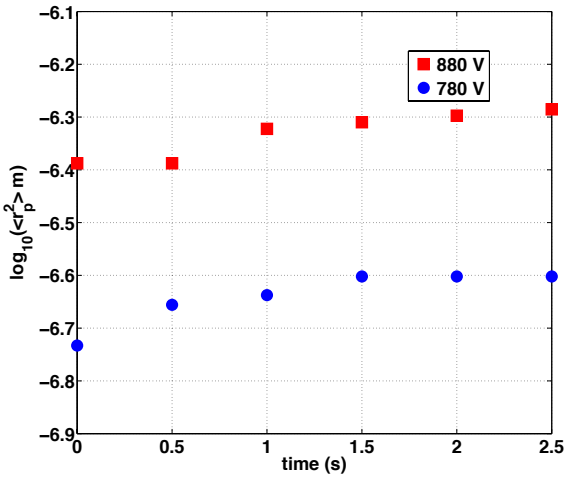

(b) Average plasma radius for the two setups. The plasma radius increased slightly with time but very little.

Figure 6.5: Electron number and individual plasma radius as a function of time.

shows that the plasma radius remains unchanged while the diocotron radius decreases. This infers that the momentum is not conserved. The damping rate is in good agreement with the work of Roberts and Rostoker [156]. In this thesis, for the first time it was shown directly, that the motion could be auto-damped inside a Malmberg Penning trap if the same conditions are fulfilled. Our analysis shows a very good agreement with the work of Roberts and Rostoker. However, plasma physics is not our field of expertise, and as a result, that the underlying cause of the damping is the interaction between the magnetic field produced by the plasma column following Ampère's law and the magnetic field of the trap itself [156], as it is shown by Roberts and Rostoker, can not be completely confirmed with certainty by us. None of the experiments earlier attempted plasma

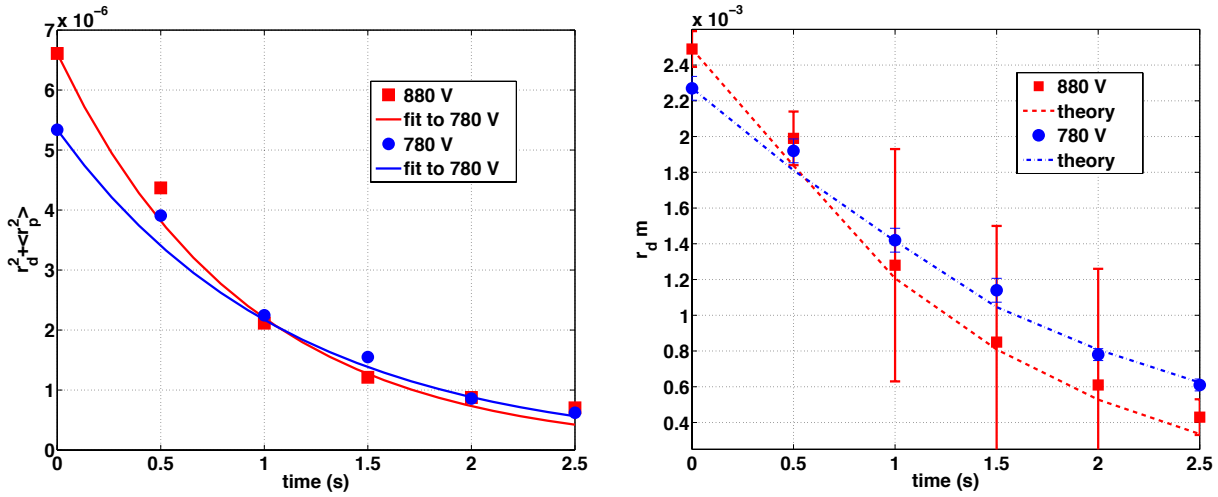

(a) Observation shows that the momentum is not conserved.

(b) Damping of the $m = 1$ mode and the theoretical fit.

Figure 6.6: Momentum study and the $m = 1$ diocotron mode damping in CPET.

	trap depth(1400-620)V 3rd April			**trap depth(1400-520) 4th April**		
Time (s)	plasma radius $\langle r_p \rangle$ mm	diocotron radius $\langle r_d \rangle$ mm	$r_d^2+\langle r_p^2 \rangle$ mm^2	plasma radius $\langle r_p \rangle$ mm	diocotron radius $\langle r_d \rangle$ mm	$r_d^2+\langle r_p^2 \rangle$ mm^2
1	0.43	2.27	5.34	0.57	2.49	6.61
1.5	0.47	1.92	3.91	0.57	1.99	4.37
2	0.48	1.42	2.25	0.60	1.28	2.12
2.5	0.50	1.21	1.72	0.57	0.85	1.07
3	0.50	0.78	0.86	0.57	0.61	0.70
3.5	0.51	0.61	0.62	0.57	0.43	0.51

Table 6.1: Times represent the duration of trapping in the trap.

confinement in the regime reported in our test. The trapping potential and electron beam used in this test are orders of magnitude higher than is reported in other efforts in which the diocotron mode is studied. Thanks to the 7T magnetic (which is much stronger than the magnets in most other similar facilities) field that kept the plasma radius small enough. Table (6.1) summarizes the data for the test we performed.

6.4 Summary

We have shown that the diocotron mode is damped in a previously unexplored parameter region that is similar in nature to that of the asymmetry driven damping reported by Sarid, which does not have any well established theory to date. The test results we have presented seem to agree with the theory provided by Roberts and Rostoker with the estimation of plasma conductivity and considering the Penning trap similar in action to their modified betatron. Roberts and Rostoker assumed Penning trap behaviour in their setup by relating it to experiments performed in Penning traps. This indicates that a reverse argument could be made, and their findings and theory might be applicable in Penning trap physics as well. However, we propose that further investigations be carried out in plasma research facilities where this $m = 1$ mode can be studied more throughly and different parameters can be controlled which are not possible to control in CPET.

Chapter 7

Mass measurement of ^{24}Al

The precise and accurate determination of the mass of ^{24}Al is important for two reasons. First to better understand the rate of explosive hydrogen burning [173] in supernova explosions [174] and second to help test the standard model (SM).

The nucleosynthesis and energy generation during explosive hydrogen burning in type-I supernovae [174] explosions, x-ray bursts [175] and accreting black holes is influenced by the rapid-capture reactions [176]. ^{24}Al is the product of the radiative proton capture reaction ^{23}Mg$(p,\gamma)^{24}$Al, which is a bridging reaction between the NeNa and MgAl cycles. The reaction rate is dependent on the resonance energy, $E_R = E_x - S_p$, where E_x and S_p are the excitation and proton separation energies respectively, and the reaction strength $\omega\gamma$. For a better understanding of the nucleosynthesis and power generation occurring in astronomical events involving ^{24}Al, a more precise and accurate S_p value is required which is derived from the ground state mass of ^{24}Al.

The isospin $T = 1$ nuclides continues to help test the standard model via the electron capture Q value, Q_{EC} by predicting the so-called ft-value. A Q_{EC} value with the precision of keV or better for the superallowed $0^+ \rightarrow 0^+\beta$ decay can contribute to the search of physics beyond the standard model for $T = 2$ nuclides as well. ^{24}Al is the daughter nuclide of one of those $T = 2$ nuclides, ^{24}Si. The development of an ion guide laser ion source (IG-LIS) by TRIUMF laser ion source group has facilitated suppressing the $A = 24$ isobaric background by orders of magnitude and allowed col-

lecting enough data for the mass measurement of ^{24}Al in a Penning trap for the first time. In this chapter we present the motivation and details of the mass measurement of ^{24}Al using TRIUMF's Measurement Penning Trap (MPET).

7.1 Astrophysical importance of ^{24}Al

The explosive hydrogen burning or rapid proton capture (rp-process) reaction takes place in high-density and/or high-temperature sites in the universe [173, 177]. This network of nuclear processes occurring on seed nuclei can produce heavier elements with A>20 [178]. The rp-process may be observed taking place in a number of stellar sites including novae with peak temperatures of $T_9(\equiv 10^9 K)$=0.2-0.4 [177], x-ray bursts typically at T_9 >0.4 [177] and accreting black holes where T_9 =1 or higher [179]. Initiated at the breakout of the HCNO cycle, the rp-process plays a major role in the synthesis of elements in the NeNa and MgAl cycles and beyond [173]. A quantitative understanding of rp-process is more challenging compared to the reactions in the HCNO cycle as the number of reactions is much larger. However, a systematic analysis of the reactions in terms of their Q-values can make the complex reaction networks more accessible [178, 180]. Being the breakout reaction from the NeNa cycle into the MgAl cycle, the rp-process reaction ^{23}Mg$(p,\gamma)^{24}$Al carries a particular importance also because a number of astrophysical γ-ray targets such as ^{22}Na($t_{1/2}$=2.6 yr) and ^{26}Al($t_{1/2}$=0.7 Myr) are produced through this reaction [181, 182]. Our understanding of the abundance of elements with A>20 in the universe depends on the reaction rate of the ^{23}Mg$(p,\gamma)^{24}$Al process [183].

In the NeNa cycle, the ^{23}Na decays into ^{20}Ne, and thus the NeNa cycle is created, which produces other elements in the NeNa mass range. In the temperature range $0.1 < T_9 < 1$, the reaction ^{23}Mg$(p,\gamma)^{24}$Al plays the major role in the production of A>20 nuclei. In this temperature range, the ^{23}Mg decay is dominated by the rapid proton capture reaction which breaks out of the NeNa cycle and starts synthesizing heavier elements in the MgAl cycle such as Si, S, and Ar depending on the density and temperature of the event and/or site [179]. For this reason the reaction ^{23}Mg$(p,\gamma)^{24}$Al is considered a bridging reaction between the NeNa and MgAl cycles [184].

The ^{23}Mg$(p,\gamma)^{24}$Al reaction rate becomes less important above the temperature of T_9 =1 since ^{21}Na$(p,\gamma)^{22}$Mg$(p,\gamma)^{23}$Al$(p,\gamma)^{24}$Si$(\beta^+,\nu)^{24}$Al bypasses the production of ^{23}Mg. At a temperature lower than $T_9 < 0.1$, synthesis of the ^{23}Mg isotope is dominated by β decay reactions in the NeNa cycle. At low temperature there is also a leak from the NeNa cycle through the ^{23}Na$(p,\gamma)^{24}$Mg reaction. Fig. (7.1) shows the two bridging reactions between the NeNa and MgAl cycles.

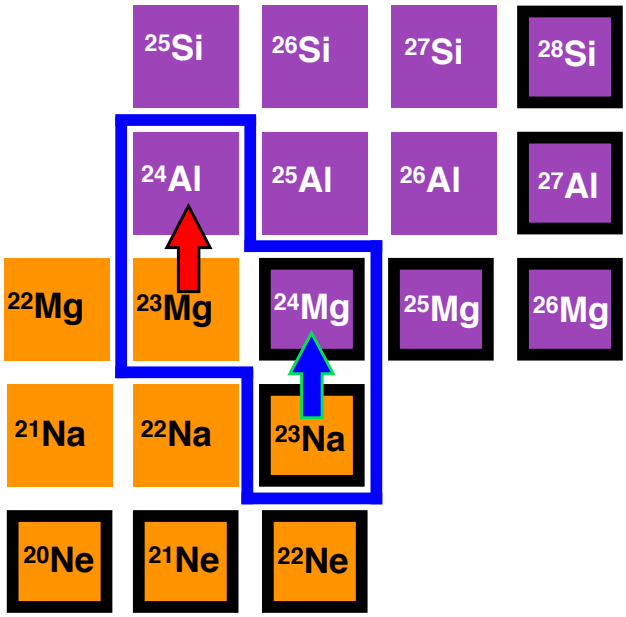

Figure 7.1: Isotopes in the Ne-Na (orange) and Mg-Al (purple) cycle. The blue border indicates the bridging reactions. Red and blue arrows show the high and low temperature cycle break points respectively. Black bordered isotopes are stable.

Now, the derivation of the reaction rate depends on the resonance energy $E_r = E_x - S_p$ and the reaction strength $\omega\gamma$ given by [180, 185]:

$$\omega\gamma = \frac{2J+1}{(2J_T+1)(2J_P+1)}\frac{\Gamma_p\Gamma_\gamma}{\Gamma_{\text{total}}}, \tag{7.1}$$

where, J_P and J_T are the spins of projectile and the target respectively. Γ_γ and Γ_p are the γ-ray and proton partial widths [178]. Clearly, the Q value (or S_p) does not have any direct effect on the reaction strength. However, as the partial widths are derived from the shell-model calculations, the ground state mass of the isotopes involved will effect the reaction strength through the partial

width values.

In the ^{23}Mg$(p,\gamma)^{24}$Al reaction, there are several predicted resonances that are of astrophysical interest, and correspond to states which are above the proton separation energy in ^{24}Al [181]. Of these, the lowest lying resonance (the so-called "473 keV" resonance) is considered to be the dominant contributor to the astrophysical reaction rate at relevant novae temperatures [179, 186]. Direct measurements of the reaction rates are difficult due to the very low cross-sections, and thus benefit from advanced knowledge of the resonance energies (E_r) to guide and constrain the search region. For ^{24}Al, the most precise measurement of the excitation energy of the 473 keV resonance is from a ^{10}B(^{16}O,$2n\gamma$) fusion evaporation reaction with GAMMASPHERE, and yields a value of $E_x = 2345.1(14)$ keV [183]. The proton separation energy is determined from differences in the mass excess values (Δ) for the constituent components in the reaction: ^{1}H, ^{23}Mg, and ^{24}Al.

In the past, the extraction of E_r from the above prescription was limited by the large relative uncertainties in the experimental mass values of ^{23}Mg and ^{24}Al [186]. Currently, the best indirect determination of $E_r = 482.1(20)$ keV is reported in [187], and results from an updated value for the ^{24}Al mass from (^{3}He,t) reactions using the Q3D spectrograph at the Maier-Leibnitz-Laboratorium in Garching, Germany. This single measurement also currently dominates the average for the most recent Atomic Mass Evaluation (AME12) [188]. At the time of its publication in 2010, this measurement reported a 3.2σ shift in the central value of the mass excess from the 2003 atomic mass evaluation [189], which translated to a 9 keV decrease in the measured ^{23}Mg(p,γ) Q value. When combined with the excitation energy in ^{24}Al from [183], a long-standing discrepancy between the indirect and direct measurement methods was resolved.

The only direct measurement of this reaction was performed using the DRAGON recoil spectrometer at TRIUMF, and yields a value for the resonance energy of $E_r = 485.7^{+1.3}_{-1.8}$ keV [186]. This value is in agreement with the indirect determination presented in [187], and is listed in Table (7.1). To confirm the revised ^{23}Mg(p,γ) Q value in [187], we present the first direct measurement of the ^{24}Al mass and report a new indirect determination of E_r.

Table 7.1: Resonance energy derivation methods for the ^{23}Mg(p,γ) ^{24}Al reaction. The energy was derived both directly and indirectly. This table shows the latest values from both methods.

Method	Experimental facility	Experimental process	Refference	E_r(keV)
Direct	DRAGON	^{23}Mg(p,γ) ^{24}Al	[186]	$485.7^{+1.3}_{-1.8}$
Indirect	Q3D	^{24}Mg$(^3$He$,t)$ ^{24}Al	[190]	482.1 (20)
Indirect	TITAN	Penning trap mass spectrometry	This work	480.8 (14)

7.2 The standard model importance of ^{24}Al

Quarks in the standard model (SM) can change from one type to another because of the weak interaction. The Cabbibo-Kobayashi-Maskawa (CKM) matrix is a unitary matrix that gives the probability of this change. It is also known as the quark-mixing matrix. According to weak-universality [5] in the SM, $\sum_{i/j}|V_{ij}|^2 = 1$, where, $i = u,c,t$ and $j = d,s,b$ are the quark flavours, and the sum is over either i or j [191]. This implies that $\sum_j |V_{uj}|^2 = 1$, with $j = d,s,b$, i.e. the sum of the squares of the elements in the first row of the CKM matrix must be equal to unity [191]. While the values of V_{us} and V_{ub} come from the high-energy physics [192], the value of V_{ud} can be calculated from nuclear physics experiments [191].

$T = 1$ nuclides have long been known for providing the most stringent way of testing the unitarity of the CKM matrix [191] via the superallowed $0^+ \rightarrow 0^+$ nuclear β-transitions. There are thirteen [193, 194] such nuclei that undergo β-decay and thus contribute towards the precise evaluation of V_{ud} through the ft-value [194]. According to the SM, the β-decay transition between $T = 1$ analogous states are mediated exclusively by the vector part of the weak interaction. The ft value for all such β-decay transitions is a fundamental constant and is the same for all such transitions (this condition is also known as the Conserved Vector Current (CVC) hypothesis). Additionally, a small ($\sim 1\%$) radiative and nuclear structure related correction needs to be considered [191]. As a result, a modified ft value is defined as:

$$\mathscr{F}t \equiv ft(1+\delta_R')(1+\delta_{NS}-\delta_c) = \frac{K}{2G_V^2(1+\Delta_R^V)}, \tag{7.2}$$

where $K/(\hbar)^6 = 2\pi^3\hbar\ln 2/(m_e c^2)^5$, G_v is the vector coupling constant for semileptonic weak interaction, δ_c is the isospin symmetry breaking correction, Δ_R^V is the transition dependent part of the radiative correction, and δ_R' and δ_{NS} are the transition-dependent part of the radiative correction. While δ_R' is only the function of electron energy and charge Z of the daughter nuclei, δ_{NS} is nuclear structure dependent correction. $V_{ud} = G_V/G_F$. So, in terms of $\bar{\mathcal{F}}t$ this V_{ud} is given by:

$$V_{ud} = \frac{K}{2G_F^2(1+\Delta_R^V)\bar{\mathcal{F}}t}. \tag{7.3}$$

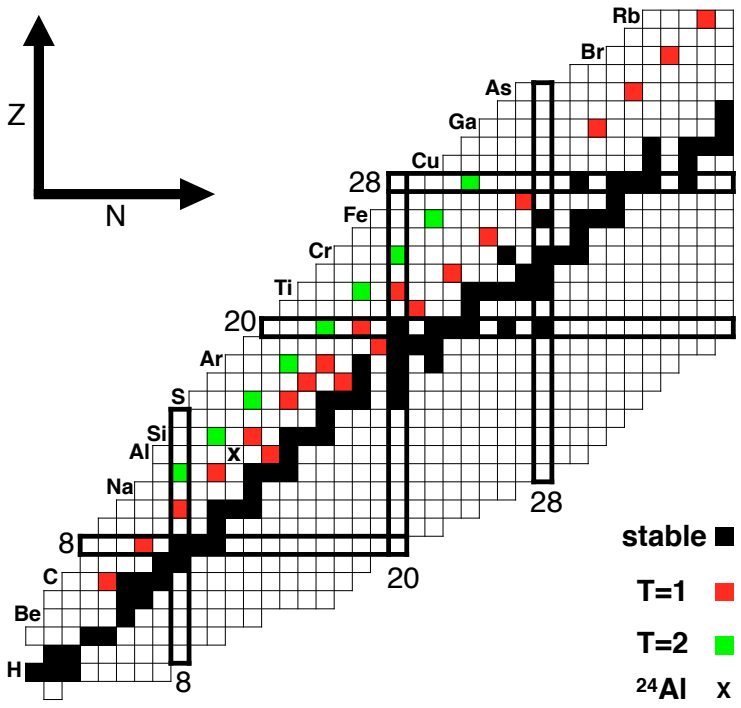

Figure 7.2: Superallowed beta decay candidates. $T = 1$ and $T = 2$ nuclide [195]. $T = 2$ nuclides are far from the stability compared to $T = 1$ nuclides.

The experimental values of Q_{EC} for $T = 1$ nuclides are known very precisely [190] and the major source of uncertainty is now theoretical [196]. On the other hand, $T = 2$ nuclides have a higher density of states near the daughter level which makes them contribute towards a more precise measurement of the isospin symmetry breaking term δ_c. This indicates that $T = 2$ nuclides undergoing superallowed β-decays can contribute to the precision measurement of V_{ud} and test

the SM [195]. The f_t value depends on three different parameters; the Q-value of the reaction involved, the branching ratio (denoted by R) and the half-life ($t_{1/2}$). The challenge imposed on the $T = 2$ Q_{EC} measurement is mainly due to the fact that the isotopes of interest are further away from stability compared to the $T = 1$ candidates as shown in Fig. (7.2). This also makes the branching ratio measurement very difficult. But, the electron capture is several orders of magnitude smaller than the β-decay, and the background is extremely high [46]. As a result, branching ratios are very challenging to measure compared to the Q-values. A successful measurement of the $T = 2$ β-decay branching ratio of ^{32}Ar has been done, and the effect of the measurement on testing the SM is being investigated [197]. Efforts are already underway for the study of all $T = 2$ nuclides [195, 198] which will look for the existence of scaler currents and thus any hint of physics beyond the standard model. Once the branching ratios are measured with a high level of precision, the ground-state mass of mother and daughter isotopes will help to calculate the f_t value and thus will facilitate testing of the SM. Any deviation in the f_t value for different isotopes will cause the breakdown of the CVC-hypothesis [5, 191, 199] and may be an indication of the presence of the scalar currents and new physics beyond the SM [200].

The SM also predicts that the β-decays are mediated exclusively by the exchange of $W^{\pm}$ bosons [5]. The SM imposes the condition that the left-handed fermions transform as $SU_L(2)$ doublets and the right-handed fermions transform as singlets [201]. The manifestation of this condition is known as parity violation. Introduction of a new gauge group of the form $SU_L(2) \otimes SU_R(2) \otimes U_1$ preserves the parity but introduces new gauge bosons [202] such as leptoquarks and a charged Higgs boson, which are parts of physics beyond the SM [203]. In the present structure of the standard model (obeying $SU_L(2)$ symmetry), the $\beta - \nu$ correlation coefficient $a_{\beta\nu}$ must be equal to 1. The parameter $a_{\beta\nu}$ could be experimentally measured from the angular distribution profile of the β-decay. In this manner, if the branching ratio and Q_{EC} values for $0^+ \rightarrow 0^+$ β-decay are measured with a high degree of precision, the existence of new particles or the validity of the SM can be tested [204]. To date the knowledge of $T = 2$ analog state β-decay is very limited. But the experimental progress in this area of low-energy physics will pave the way to test of the SM in this

relatively new manner. The mass of ^{24}Al will be necessary and have a significant impact on testing the SM once the β-decay branching ratio is measured with significant precision.

7.3 Experimental procedure

The basic underlying mechanism of the Penning trap measurement is to convert the magnetron motion (ω_-) into reduced cyclotron motion (ω_+) as discussed in section 2.2.3. A stable reference ion of closer mass is always used to minimize the systematic errors [205] in mass measurement. If HCIs are measured, the A/q for the ion of interest and the reference ion are maintained as close as possible for the same reason [47]. To do this, a measurement of the reference ions is done before and after the measurement of the ion of interest. In this manner, by taking the ratio of the cyclotron frequencies, most of the common parameters cancel out and systematic uncertainties due to trap imperfections [33] are minimized [205]. Fig. (7.3) shows the resonances for ^{23}Na and ^{24}Al. A linear interpolation of the changing magnetic field between consecutive reference ion's

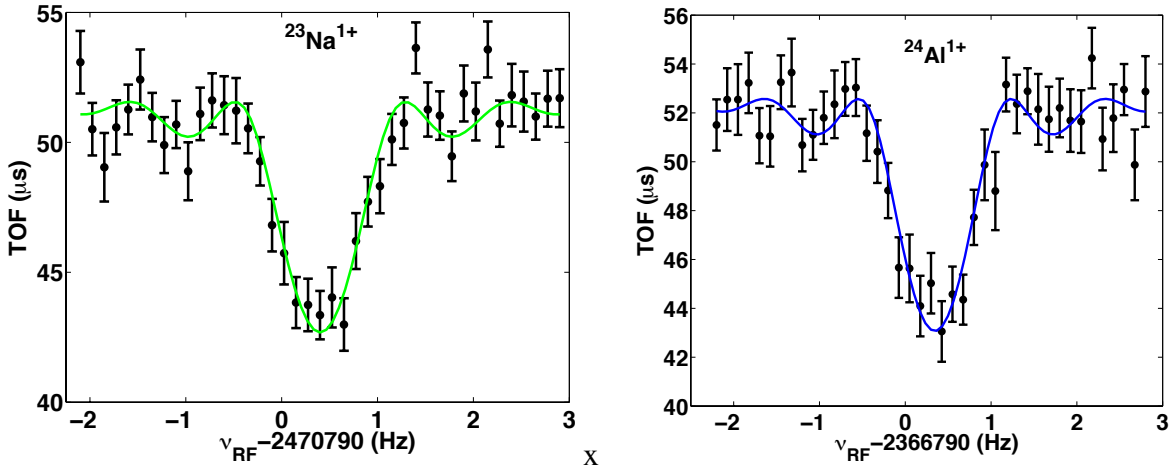

(a) ^{23}Na resonance. (b) ^{24}Al resonance.

Figure 7.3: Resonances for ^{23}Na and ^{24}Al measurements.

cyclotron frequencies is used to estimate the field during the measurement. Although the trap-dependent systematics are minimized by a proper choice of reference ions, the trap-independent systematics can not be eliminated by means of the reference ion measurement. Ion-ion interaction inside the trap is one such source of systematic uncertainties. To take into account the shifts

in the cyclotron frequency due to ion-ion interactions, a count-class analysis is done [53]. The count-class analysis extrapolates the frequency ratios to single ion trapping. The relativistic effect [27] in the cyclotron frequency measurement is another trap-independent source of systematic error [205]. The relativistic effect in the ion's cyclotron frequency for TITAN was extensively studied in reference [28]. The result shows that for heavier ions (A$\sim$10) the relativistic uncertainty contribution is in the range of ppb [28, 37, 206]. The relativistic contribution gets increasingly smaller for heavier ions. As a result, in the ^{24}Al mass measurement we can ignore the effect. A number of successful mass measurements were accomplished at TITAN [207] using the TFCR-ICR method which continue to date.

7.4 ^{24}Al mass measurement and result

The extraction of some isotopes from the target is extremely challenging due to the chemical constraints involved [43]. For some isotopes a laser is used to ionize the isotopes of interest and extract them from the target. This is done by the TRILIS group at TRIUMF [43, 208]. For other isotopes the background is too high to do a successful measurement and hence a method was developed to filter the ion of interest. This is done by an ion guide-laser ion source (IG-LIS) that was used for the first time to suppress the background by several orders of magnitude and is reported in other measurements [12]. The background was suppressed by a factor of $\sim 10^6$ in the mass measurement of of ^{24}Al using IG-LIS [18].

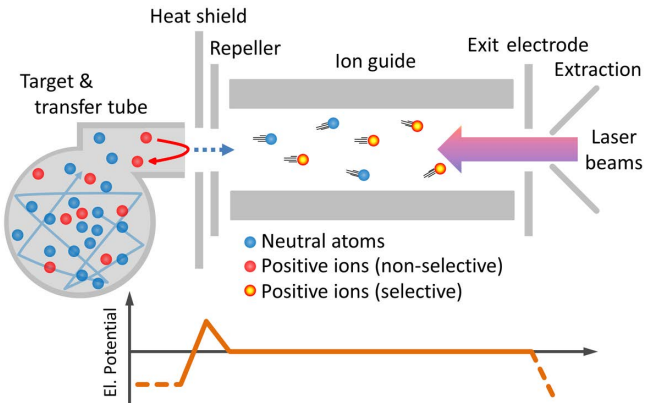

Figure 7.4: IG-LIS ion source schematic. A laser is used to ionize only the ions of interest.

The use of IG-LIS yielded ∼160 ^{24}Al ions per second and we were able to perform a total of five measurements for ^{24}Al. All five are very satisfactory in terms of the resonances. To take these resonances, a quadrupolar RF field was applied for 975 ms inside the MPET while the two contaminant ions were forced to hit the trap wall applying their corresponding dipole frequencies for 20 ms with a peak-to-peak amplitude of 1V. A Daly detector [42, 209] with 70% efficiency was used to detect the ions while a precision atomic clock was used to measure the time of flight from extraction to the detection at the Daly detector. The mass of ^{39}K was measured to confirm the system's accuracy.

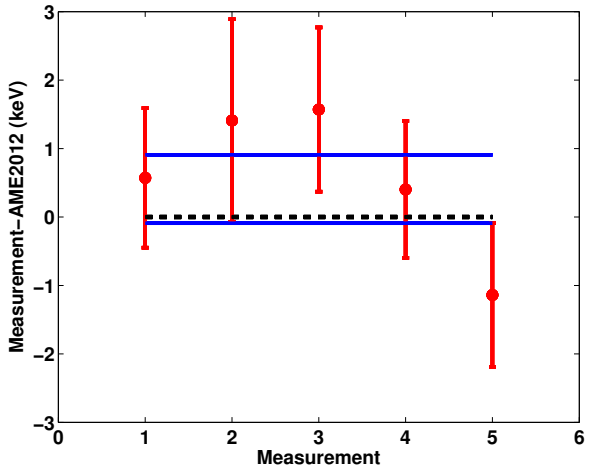

Figure 7.5: ^{39}K measurements for accuracy check. The blue lines give the 1σ statistical uncertainty while the dashed lines are for AME2012. The AME2012 uncertainty is too small to be visible in this graph (and hence appears to be a single line) as expected for an ideal reference.

This confirmed that the system did not shift from its stable operational mode. Fig. (7.5) shows that the results of the accuracy check agree with the AME2012 value of the ^{39}K mass [188]. A thorough study of the systematic uncertainty due to relativistic effects, non-linear magnetic field fluctuations, and trap imperfections was performed [54] and shows that the total uncertainty is well below the statistical uncertainty in this experiment. Regardless, the systematic uncertainty of the system was added in quadrature to the statistical uncertainty to find the total uncertainty. The mass

of the ion of interest can be calculated using the following relation:

$$m = \frac{q}{q_{ref}} \times \overline{R} \times (m_{ref} - q_{ref} \times m_e + B_{e,ref}) + q \times m_e - B_e. \tag{7.4}$$

The binding energy of electrons, B_e, for both the ion of interest and the reference ions is $\simeq$ 5eV and hence is ignored in the calculation. For any future improvements in the mass measurement of ^{24}Al the masses are represented in the ratio $\overline{R}$. Of the five measurements done for ^{24}Al, four measurements agree with the previous measurement within 1σ and one measurement slightly disagrees. However, the mass excess shifts by $\sim$ 1 keV and the precision is improved $\sim$5 times compared to the previous measurement. Fig. (7.6) shows the ^{24}Al measurements together with the AME2012 result. Table (7.2) summarizes the measurement. Fig. (7.7) shows the proton separation energy

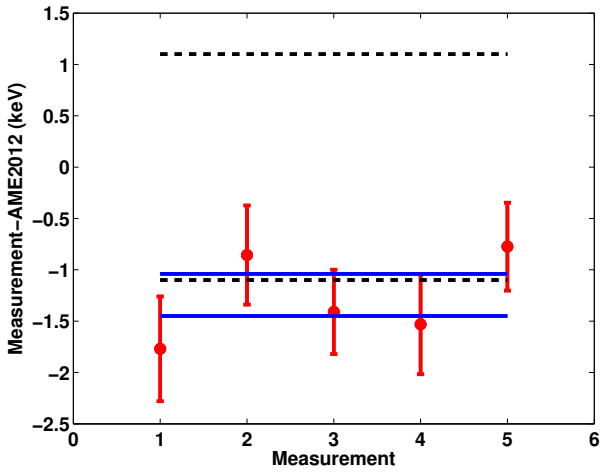

Figure 7.6: ^{24}Al measurements. Total five measurements were performed. The blue lines give the 1σ statistical uncertainty while the dashed lines are for AME2012 uncertainty.

calculated using our value, Q3D [210] and the previous best known value [188].

7.5 The effect of the ^{24}Al mass on the ^{23}Mg$(p,\gamma)^{24}$Al reaction rate

The best known reaction rate for ^{23}Mg$(p,\gamma)^{24}$Al is extracted from the experiments [186] and [187]. Both used the Q value obtained from the ground state mass measurement of ^{24}Al from

Table 7.2: Summary of the ^{24}Al mass measurement. Details of the two ion species used for this experiment. ^{23}Na was used as reference for the mass measurement of ^{24}Al (975 ms RF excitation) and also for the system's accuracy check (995 ms RF excitation). A total of 5 measurements were done for ^{24}Al. Statistical uncertainties are given in the (parentheses) while the total uncertainty is in the [square bracket].

Nuclide	$\overline{R} = \nu/\nu_{\text{ref}}$	ME_{TITAN} (keV)	$\text{ME}_{\text{AME2012}}$ (keV)	Δ ME (keV)
^{24}Al	0.957 908 1847(87)[97]	-48.856(0.205)[0.227]	-47.614[1.104]	-1.242

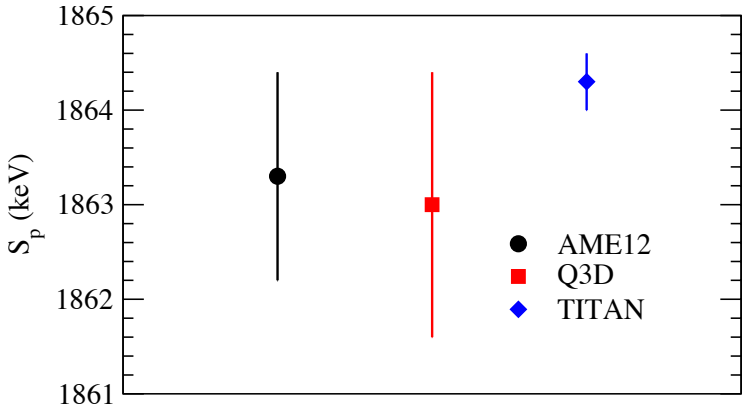

Figure 7.7: Proton separation energy calculated using our value, the previously know best value from AME2012 [188] and the Q3D.

the ^{24}Mg(^{3}He, t)^{24}Al reaction. We have measured the ^{24}Al mass using the Penning trap TOF-ICR method which will better constrain the reaction rate value. This will improve theoretical calculations of the abundance of the A>20 isotopes as well as the those of the energy generation in the celestial events discussed above. The reaction rate calculated from our evaluation of ^{24}Al shows a 2σ mismatch with the reaction rate measurement done by DRAGON. As a result of the significant improvement in precision for both the ^{24}Al (this work) and ^{23}Mg [9] masses, a new indirect determination of the ^{23}Mg(p,γ) resonance energy is extracted as $E_r = 480.8(14)$ keV. This value agrees with previous indirect extractions of E_r, but deviates from the direct measurement by more than 2σ. The agreement in S_p between this work and the AME12 implies that this difference results from either a discrepancy in the direct measurement or the excitation-energy measurement in [183]. A comparison of the extracted resonance energies through the different measurements and methods is shown in Fig. (7.8). The indirect extractions of E_r presented in Fig. (7.8) all require the

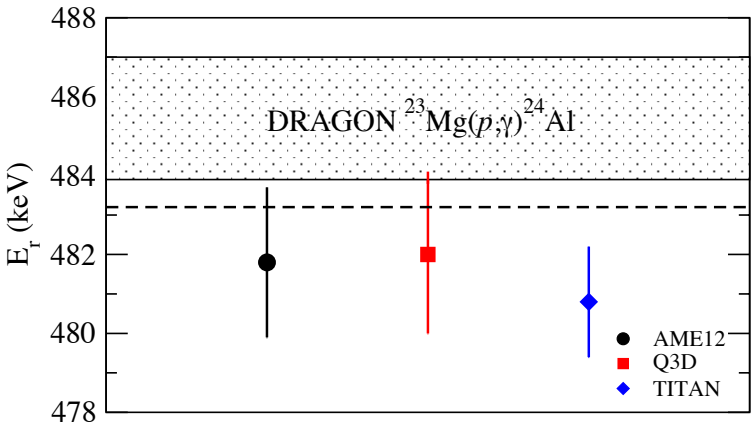

Figure 7.8: Comparison of the resonance value directly measured by DRAGON and the calculated value using our measurement. There is a 2σ discrepency.

^{24}Al excitation energy measurement from [183] for the extraction of E_r. Therefore, a discrepancy in this single measurement could lead to the observed difference with the direct measurement. The absolute difference in the central value of E_r between this work and DRAGON is nearly 5 keV, and represents the shift in the excitation energy from [183] that would have to be present for exact agreement between the two methods. The improvement in uncertainty on the atomic masses from this work and [9] therefore provides an increased motivation for confirmation of the 2345 keV state energy in ^{24}Al.

For the direct measurement, possible systematic effects in the DRAGON setup have been well studied, and are presented in [211]. Although the uncertainties quoted in [186] are relatively large, DRAGON has been calibrated to a variety of well known proton-capture resonances over the course of several years. A systematic reduction of 0.15% in the value used for their magnet constant was, however, recently suggested [211]. This shift would lead to a decrease in the recommended resonance energy from the direct ^{23}Mg(p,γ) measurement in [186]. When this prescription is applied, the slightly revised value of $E_r = 485.0^{+1.3}_{-1.8}$ keV from the direct DRAGON measurement moves closer to agreement with the result presented here, but still presents a discrepancy. Although this adjustment is a good estimate of the revised value, it is slightly misleading since [186] gives a probability distribution function for the resonance strength, which is directly tied to the extraction of E_r. Therefore, the result presented here also increases the motivation for a new direct measurement

of the ^{23}Mg$(p,\gamma)^{24}$Al reaction.

7.6 Conclusion

A precise and accurate determination of the mass of ^{24}Al is of very important physical interest for both astrophysics and the SM. For the first time, we have measured the mass of this isotope directly using the TITAN Penning trap. This measurement was made possible through the use of TRIUMFs new ion-guide laser ion source for isobaric purification of the delivered ion beam. The measured mass excess was found to be in agreement with the most recent atomic mass evaluation, but five times more precise. When combined with the excitation energy of the 473 keV resonance state in ^{24}Al, and a recent measurement of the ^{23}Mg mass, the astrophysical ^{23}Mg(p, γ)^{24}Al reaction resonance energy is extracted as E_r= 480.8(14) keV, which disagrees with the only direct measurement of this quantity using the DRAGON recoil spectrometer at TRIUMF. With the significant increase in precision on the constituent masses, the limiting uncertainty on the indirect extraction of E_r now rests with the excitation energy measurement. In addition to this discrepancy, the direct measurement of the resonance strength $\omega\gamma$ remains the limiting factor for improving the uncertainty on nova-produced ^{26}Al and ^{22}Na. Therefore, the result presented here further increases the motivation for a new direct measurement of the ^{23}Mg(p, γ)^{24}Al reaction. This will help calculate the complex network of element synthesis and their abundance in the universe. At the same time, as the branching-ratio value improves through γ-ray spectroscopy, the ground state mass of ^{24}Al will help test the standard model through f_t value evaluation.

Chapter 8

Summary and outlook

From the microscopic world of quarks and gluons to the creation of galaxies and galaxy clusters, the beauty of physics is that the same physical laws govern everything. And a major portion of this understanding of the universe is through nuclear physics. The journey of understanding the nature that started with Ernest Rutherford's gold foil experiment is nowadays propelled by the virtue of powerful accelerators and reactor facilities worldwide. Each of the thousands of isotopes on the nuclear landscape is unique and plays a role on our understanding of the universe. However, while only about 200 of the isotopes are stable, the remaining are unstable and some of them are difficult to produce. Scientists are building newer, and more powerful accelerators to explore those uncharted territories. The Advanced Rare IsotopE Laboratory (ARIEL) in Canada, the Facility for Rare Isotope Beam (FRIB) in the USA, the Radio Isotope Beam Factory (RIBF) in Japan, and the Rare Isotope Science Project (RISP) in South Kore are some of the newer facilities that will continue the journey in the coming years to answer the outstanding questions regarding nuclear structure, abundance of elements in the universe, existence of a better theory beyond the Standard Model (SM) and so on.

This thesis has discussed how TITAN's unique charge breeding method facilitates the mass measurement of isotopes with a very high precision and how the energy spread introduced during the charge-breeding process causes a significant loss of valuable isotopes. We also discussed the

way CPET will provide MPET with a better quality beam for mass measurement. The precondition for successful cooling is to have a cold and dense electron plasma that can interact with the HCIs. Because of their low mass, the electrons have the tendency of following the magnetic field-lines and very difficult to steer by the static electric fields, which makes the loading, extraction and the detection very challenging. The plasma life-time varies significantly with the alignment of the trap axis with respect to the magnetic field axis. We demonstrated that a large number of electrons can be accumulated at high density in CPET for the cooling of HCIs. This is the confirmation of a functioning system and a sufficiently good alignment and an overall success of the project to date. During the offline tests of CPET with electrons, we also observed the damping of the $m = 1$ diocotron mode of plasma oscillation. We believe that we are observing the damping of this mode in a different parameter regime.

In this thesis we have discussed the importance of the precise value of the ^{24}Al mass in astrophysics, and also how the value can contribute towards the test of the SM. We have for the first time measured the mass of ^{24}Al using a Penning trap. The result is five times more precise than the previous AME (AME2012) value [188]. This new result improves the indirectly calculated rate of the Ne-Na cycle break-out reaction ^{23}Na$(p,\gamma)^{24}$Al by 2σ and found to disagree with the direct observation by 2σ. This is a significant discrepancy.

In conclusion, the work presented in this thesis is important for a number of reasons. Firstly, the development of CPET will prevent the loss of valuable radioactive beam and increase the precision of mass mass measurement with HCIs. This will be done by reducing the width of the energy distribution of the ions after charge breeding in the EBIT and also by cleaning the beam containing ions of similar mass-over-charge ratio (m/q).

Secondly, the damping of the $m = 1$ mode in a different parameter regime was observed. Further tests with electron plasma and ions will be carried out in the next step to successfully cool the HCIs in the CPET.

Thirdly, the first Penning trap mass measurement of ^{24}Al will help re-evaluate the reaction rates and thus the abundance of elements to follow in the cycles involved. A direct measurement

of the ^{23}Na$(p,\gamma)^{24}$Al reaction rate will be required to confirm the validity or any deficiency in the calculation.

Lastly, we hope that in the near future the electron capture branching ratio of the isospin $T = 2$ nuclides will be determined precisely enough, and the ground state mass of ^{24}Al will play a major role in evaluating the f_t-value more precisely and thus help test the SM.

Bibliography

[1] K. A. Olive and Particle Data Group. Review of particle physics. *Chinese Physics C*, 38(9):090001, 2014. → pages 1

[2] Glenn Elert. The physics hyper text book, 1999. → pages 1, 2

[3] D. Jackson. *Classical Electrodynamics*. John Wiley & Sons, Inc., 1999. → pages 1, 14, 24

[4] D. A. Greenwood W. N. Cottingham. *An Introduction to the Standard Model of Particle Physics*. Cambridge University Press, 2007. → pages 1

[5] Cliff Burgess and Guy Moore. *The Standard Model: A Primer*. Cambridge University Press, 2007. → pages 1, 108, 110

[6] G. Aad, T. Abajyan, and B. Abbott. Observation of a new particle in the search for the Standard Model Higgs boson with the ATLAS detector at the LHC. *Physics Letters B*, 716:1–29, 2012. → pages 2

[7] S. Chatrchyan et al. Observation of a new boson at a mass of 125 GeV with the CMS experiment at the LHC. *Physics Letters, Section B: Nuclear, Elementary Particle and High-Energy Physics*, 716(1):30–61, 2012. → pages 2

[8] David H Weinberg, James S Bullock, Fabio Governato, Rachel Kuzio de Naray, and Annika HG Peter. Cold dark matter: controversies on small scales. *Proceedings of the National Academy of Sciences*, page 201308716, 2015. → pages 2

[9] B. E. Schultz, M. Brodeur, C. Andreoiu, A. Bader, A. Chaudhuri, U. Chowdhury, A. T. Gallant, A. Grossheim, R. Klawitter, A. A. Kwiatkowski, K. G. Leach, A. Lennarz, T. D. Macdonald, J. Lassen, H. Heggen, S. Raeder, A. Teigelhöfer, and J. Dilling. Precision QEC-value measurement of 23Mg for testing the Cabibbo-Kobayashi-Maskawa matrix unitarity. *Physical Review C*, 90:012501, 2014. → pages 3, 115, 116

[10] S. Ettenauer et al. First Use of High Charge States for Mass Measurements of Short-Lived Nuclides in a Penning Trap. *Physical Review Letters*, 107(27):272501, December 2011. → pages 3, 14

[11] A. Chaudhuri et al. Evidence for the extinction of the N=20 neutron-shell closure for ^{32}Mg from direct mass measurements. *Physical Review C*, 88(5):054317, November 2013. → pages 3

[12] A. T. Gallant, M. Brodeur, C. Andreoiu, A. Bader, A. Chaudhuri, U. Chowdhury, A. Grossheim, R. Klawitter, A. A. Kwiatkowski, K. G A. Leach, A. Lennarz, T. D. Macdonald, B. E. Schultz, J. Lassen, H. Heggen, S. Raeder, A. Teigelhöfer, B. A. Brown, A. Magilligan, J. D. Holt, J. Menéndez, J. Simonis, A. Schwenk, and J. Dilling. Breakdown of the Isobaric Multiplet Mass Equation for the A=20 and 21 Multiplets. *Physical Review Letters*, 113(8):082501, August 2014. → pages 112

[13] T. D. Macdonald, B. E. Schultz, J. C. Bale, A. Chaudhuri, U. Chowdhury, D. Frekers, A. T. Gallant, A. Grossheim, A. A. Kwiatkowski, A. Lennarz, M. C. Simon, V. V. Simon, and J. Dilling. Precision Penning-trap measurement to investigate the role of the ^{51}Cr(e^-, ν_e)^{51}V Q-value in the gallium anomaly. *Physical Review C*, 89(4):044318, April 2014. → pages 3

[14] V. V. Simon et al. Penning-trap mass spectrometry of highly charged, neutron-rich Rb and Sr isotopes in the vicinity of A≈100. *Physical Review C*, 85(6):064308, June 2012. → pages 3

[15] K. S. Fine and C. F. Driscoll. The finite length diocotron mode. *Physics of Plasmas (1994-present)*, 5(3):601–607, 1998. → pages 4, 71, 76, 95

[16] U. Chowdhury, M. Good, B. Kootte, D. Lascar, B. E. Schultz, J. Dilling, and G. Gwinner. A cooler Penning trap for the TITAN mass measurement facility. *AIP Conference Proceedings*, 120:120–123, 2015. → pages 4, 47, 94, 95

[17] U. Chowdhury, K. G. Leach, C. Andreoiu, A. Bader, M. Brodeur, A. Chaudhuri, A. T. Gallant, A. Grossheim, G. Gwinner, R. Klawitter, A. A. Kwiatkowski, A. Lennarz, T. D. Macdonald, J. Pearkes, B. E. Schultz, and J. Dilling. First direct mass measurement of the neutron-deficient nucleus ^{24}Al. *Physical Review C*, 92(4):045803, Oct 2015. → pages 4

[18] Sebastian Raeder et al. An ion guide laser ion source for isobar-suppressed rare isotope beams. *The Review of scientific instruments*, 85(3):033309, March 2014. → pages 4, 11, 112

[19] Professor E. Rutherford F. R. S. The scattering of α and β particles by matter and the structure of the atom. *Philosophical Magazine Series 6*, 21(125):669–688, 1911. → pages 5

[20] C. Davisson and L. H. Germer. Diffraction of electrons by a crystal of nickel. *Phys. Rev.*, 30:705–740, Dec 1927. → pages 5

[21] Günther Werth Fouad G. Major, Viorica N. Gheorghe. *Charged Particle Traps: Physics and Techniques of Charged Particle Field Confinement*. Springer Series on Atomic, Optical, and Plasma Physics, 2005. → pages 5, 22, 23

[22] Hans Dehmelt. Experiments with an isolated subatomic particle at rest. *Rev. Mod. Phys.*, 62:525–530, Jul 1990. → pages 5

[23] J. Eschner, Giovanna Morigi, F. Schmidt-Kaler, and Rainer Blatt. Laser cooling of trapped ions. *JOSA B*, 20(5), 2003. → pages 6, 35

[24] L. S. Brown and Gerald Gabrielse. Geonium theory: Physics of a single electron or ion in a Penning trap. *Reviews of Modern Physics*, 193(4), 1986. → pages 6

[25] V.V. Simon. *Penning-Trap Mass Spectrometry of Radioactive, Highly Charged Ions: Measurements of neutron-rich Rb and Sr nuclides for nuclear astrophysics and the development of a novel Penning trap for cooling highly charged ions*. PhD thesis, Ruperto-Carola University of Heidelberg,, 2012. → pages 7, 43, 44, 48

[26] Günther Werth, Viorica N. Gheorghe, and Fouad G. Major. *Charged Particle Traps II*, volume 54 of *Springer Series on Atomic, Optical, and Plasma Physics*. Springer Berlin Heidelberg, Berlin, Heidelberg, 2009. → pages 8, 22, 95

[27] L. S. Brown and G. Gabrielse. Geonium Theory: Physics of a single electron or ion in a Penning trap. *Reviews of Modern Physics*, 58(1):233, 1986. → pages 8, 16, 112

[28] M. Brodeur. *First direct mass measurement of the two and four neutron halos ^{6}He and ^{8}He using the TITAN Penning trap mass spectrometer*. PhD thesis, University of British Columbia, 2009. → pages 10, 14, 15, 38, 46, 47, 112

[29] J. R. Danielson and D. H. E. Dubin. Plasma and trap-based techniques for science with positrons. *Reviews of Modern Physics*, 87(March), 2015. → pages 10, 39, 95

[30] M. C. Fujiwara et al. Particle Physics Aspects of Antihydrogen Studies with ALPHA at CERN. *AIP Conference Proceedings*, 1037:208–220, 2008. → pages 10

[31] F. Herfurth et al. HITRAP Heavy , highly charged Ions at Rest : Status and experimental Opportunities. *Journal of Physics: Conference Series*, 388(14):142009, November 2012. → pages 11

[32] S. Fedotova, E Boulton, N. P. M. Brantjes, F. Herfurth, N. Kotovskiy, C. Krantz, D. Neidherr, J. Steinmann, and G. Vorobjev. Cooling of highly charged ions–the HITRAP facility and Cooler trap. *Physica Scripta*, T156:014095, September 2013. → pages 11, 39

[33] G. Bollen, S. Becker, and H. J. Kluge. ISOLTRAP: a tandem Penning trap system for accurate on-line mass determination of short-lived isotopes. *Nuclear Instruments and Methods in Physics Research A*, 368:675–697, 1996. → pages 11, 15, 111

[34] G. Savard, R. C. Barber, and D. Beeching. Canadian Penning trap mass spectrometer. *Nuclear Physics A*, 626(1997):353–356, 1997. → pages 11

[35] J. Hakala, V.-V. Elomaa, T. Eronen, U. Hager, A. Jokinen, and J. Äystö. The JYFLTRAP control and measurement system. *Nuclear Instruments and Methods in Physics Research Section B: Beam Interactions with Materials and Atoms*, 266(19-20):4628–4631, October 2008. → pages 11

[36] M. Block, D. Ackermann, and D. Beck. The ion-trap facility SHIPTRAP. *EPJ A*, 50:49–50, 2005. → pages 11

[37] R. Ringle, G. Bollen, a. Prinke, J. Savory, P. Schury, S. Schwarz, and T. Sun. The LEBIT 9.4T Penning trap mass spectrometer. *Nuclear Instruments and Methods in Physics Research Section A: Accelerators, Spectrometers, Detectors and Associated Equipment*, 604(3):536–547, June 2009. → pages 11, 112

[38] J. Dilling, P. Bricault, M. Smith, and H. J. Kluge. The proposed TITAN facility at ISAC for very precise mass measurements on highly charged short-lived isotopes. *Nuclear Instruments and Methods in Physics Research Section B: Beam Interactions with Materials and Atoms*, 204:492–496, May 2003. → pages 11

[39] J. Dilling, R. Baartman, P. Bricault, M. Brodeur, L. Blomeley, F. Buchinger, J. Crawford, J.R. Crespo López-Urrutia, P. Delheij, M. Froese, G.P. Gwinner, Z. Ke, J.K.P. Lee, R.B. Moore, V. Ryjkov, G. Sikler, M. Smith, J. Ullrich, and J. Vaz. Mass measurements on highly charged radioactive ions, a new approach to high precision with TITAN. *International Journal of Mass Spectrometry*, 251(2-3):198–203, April 2006. → pages 11

[40] A. Lapierre, M. Brodeur, T. Brunner, S. Ettenauer, A. T. Gallant, V. Simon, M. Good, M. W. Froese, J. R. Crespo López-Urrutia, P. Delheij, S. Epp, R. Ringle, S. Schwarz, J. Ullrich, and J. Dilling. The TITAN EBIT charge breeder for mass measurements on highly charged short-lived isotopesFirst online operation. *Nuclear Instruments and Methods in Physics Research Section A: Accelerators, Spectrometers, Detectors and Associated Equipment*, 624(1):54–64, December 2010. → pages 12

[41] M. Dombsky, D. Bishop, P. Bricault, D. Dale, A. Hurst, K. Jayamanna, R. Keitel, M. Olivo, P. Schmor, and G. Stanford. Commissioning and initial operation of a radioactive beam ion source at ISAC. *Review of Scientific Instruments*, 71(2):978, February 2000. → pages 11

[42] Stephan Ettenauer. *First Mass Measurement of Highly Charged, Short-lived Nuclides in a Penning Trap and the mass of Rb-74*. PhD thesis, University of British Columbia, May 2012. → pages 13, 113

[43] J. Lassen et al. Resonant Ionization Laser Ion Source Project at TRIUMF. *Hyperfine Interactions*, 162(1-4):69–75, March 2006. → pages 11, 112

[44] T. Brunner, M. J. Smith, and M. Brodeur. TITAN's digital RFQ ion beam cooler and buncher, operation and performance. *Nuclear Instruments and Methods in Physics Research A*, 676:32–43, June 2012. → pages 12

[45] A. T. Gallant, M. Brodeur, T. Brunner, S. Ettenauer, M. Good, A. Lapierre, R. Ringle, V. V. Simon, P. Delheij, and J. Dilling. TITAN-EBIT charge breeding of radioactive isotopes for high precision mass measurements. *Journal of Instrumentation*, 5(08):C08009–C08009, August 2010. → pages 13, 14

[46] T. Brunner, M. Brodeur, C. Champagne, D. Frekers, R. Krücken, A. Lapierre, P. Delheij, R. Ringle, V. Ryjkov, M. Smith, I. Tanihata, and J. Dilling. Electron capture branching ratio measurements in an ion trap for double beta decay experiments at TITAN. *Nuclear Instruments and Methods in Physics Research Section B: Beam Interactions with Materials and Atoms*, 266(19-20):4643–4646, October 2008. → pages 13, 110

[47] M. C. Simon et al. The on-line charge breeding program at TRIUMF's Ion Trap For Atomic and Nuclear Science for precision mass measurements. *The Review of scientific instruments*, 83(2):02A912, February 2012. → pages 13, 111

[48] A. Lennarz et al. In-Trap Spectroscopy of Charge-Bred Radioactive Ions. *Physical Review Letters*, 113(8):082502, August 2014. → pages 14

[49] T. Brunner et al. In-trap decay spectroscopy for $2\nu\beta\beta$ decay experiments. *Hyperfine Interactions*, 199(1-3):191–199, April 2011. → pages 14

[50] R. Klawitter. TITAN EBIT personal communication. → pages 14

[51] Martin Kretzschmar. Theoretical investigations of different excitation modes for Penning trap mass spectrometry. *International Journal of Mass Spectrometry*, 2013. → pages 16

[52] S. Ettenauer, M. Brodeur, T. Brunner, A. T. Gallant, A. Lapierre, R. Ringle, M. R. Pearson, P. Delheij, J. Lassen, D. Lunney, and J. Dilling. Precision ground state mass of ^{12}Be and an isobaric multiplet mass equation (IMME) extrapolation for 2^+ and 0_2^+ states in the T=2, A=12 multiplet. *Physical Review C*, 81(2):024314, February 2010. → pages 16

[53] A. Kellerbauer, K. Blaum, G. Bollen, F. Herfurth, H.-J. Kluge, M. Kuckein, E. Sauvan, C. Scheidenberger, and L. Schweikhard. From direct to absolute mass measurements: A study of the accuracy of ISOLTRAP. *The European Physical Journal D-Atomic, Molecular and Optical Physics*, 22(1):53–64, January 2003. → pages 16, 112

[54] M. Brodeur, T. Brunner, C. Champagne, S. Ettenauer, M. Smith, A. Lapierre, R. Ringle, V. L. Ryjkov, G. Audi, P. Delheij, D. Lunney, and J. Dilling. New mass measurement of ^{6}Li and ppb-level systematic studies of the Penning trap mass spectrometer TITAN. *Physical Review C*, 80(4):044318, October 2009. → pages 17, 113

[55] V. V. Simon, U. Chowdhury, P. Delheij, J. Dilling, B. Eberhardt, and G. Gwinner. A cooler penning trap for the titan on-line trapping facility. *Journal of Physics: Conference Series*, 312(5):052024, sep 2011. → pages 19, 28, 38, 95

[56] E. A. Cornell and C. E. Wieman. Nobel Lecture: Bose-Einstein condensation in a dilute gas, the first 70 years and some recent experiments. *Reviews of Modern Physics*, 74(July), 2002. → pages 19, 31

[57] D. Kielpinski, C. Monroe, and D. J. Wineland. Architecture for a large-scale ion-trap quantum computer. *Nature*, 417(June):709–711, 2002. → pages 19, 37

[58] J. Bergquist, Randall Hulet, Wayne Itano, and D. Wineland. Observation of Quantum Jumps in a Single Atom. *Physical Review Letters*, 57(14):1699–1702, 1986. → pages 19

[59] C. Monroe, D. M. Meekhof, and B. E. King. Resolved-sideband Raman Cooling of a bound atom to the 3D zero-point energy. *Physical Review Letters*, 1995. → pages 19, 34

[60] E. RIIS C. S. Adams. Laser cooling and trapping of neutral atoms. *Physics, 1996-2000*, 21(1):1–79, 2002. → pages 20

[61] H. Goldstein, C. P. Poole, and J. L. Safko. *Classical Mechanics*. Addison Wesley, 2002. → pages 20

[62] W. Greiner. *Classical Mechanics, System of Particles and Hamiltonian Dynamics*. Springer, Heidelberg, 2007. → pages 20

[63] W. Petrich, M. Grieser, R. Grimm, and A. Gruber. Laser cooling of stored high-velocity ions by means of the spontaneous force. *Physical Review A*, 48(3), 1993. → pages 20, 34

[64] Claus Zimmermann (Editor) Matthias Weidemller (Editor). *Interactions in Ultracold Gases: From Atoms to Molecules*. Wiley-VCH, 2003. → pages 20

[65] E. M. Lifshitz L. D. Landau. *Statistical Physics, Third Edition, Part 1: Volume 5*. Pergamon Press, 1980. → pages 20

[66] H. Higaki, N. Kuroda, T. Ichioka, K. Franzen, Z. Wang, K. Komaki, Y. Yamazaki, M. Hori, N. Oshima, and A. Mohri. Electron cooling of high-energy protons in a multiring trap with a tank circuit monitoring the electron-plasma oscillations. *Physical Review E*, 65(4):046410, April 2002. → pages 22

[67] R. J. Fonck. Plasma ion temperature measurements via charge exchange recombination radiation. *Applied Physics Letters*, 42(3):239, 1983. → pages 22

[68] P. Beiersdorfer, V. Decaux, and K. Widmann. Measurement of the temperature of cold highly charged ions produced in an electron beam ion trap. *Nuclear Instruments and Methods in Physics Research B*, 98:566–568, 1995. → pages 22

[69] W. M. Itano and J. C. Bergquist. Cooling methods in ion traps. *Physica Scripta*, 106, 1995. → pages 23, 24, 25, 26, 27, 30, 38

[70] S. L. Rolston and G. Gabrielse. Cooling antiprotons in an ion trap. *Hyperfine Interactions*, 44:233–245, 1989. → pages 25, 40

[71] G. Maero. *Cooling of highly charged ions in a Penning trap for HITRAP*. PhD thesis, Rupertus-Carola University of Heidelberg, Germany, 2008. → pages 25

[72] Anna A. Kwiatkowski et al. Mass measurements of singly and highly charged radioactive ions at TITAN: A new Q_{EC}-value measurement of ^{10}C. *Annalen der Physik*, 525(7):529–537, July 2013. → pages 25

[73] F. Herfurth, J. Dilling, and A. Kellerbauer. A linear radiofrequency ion trap for accumulation, bunching, and emittance improvement of radioactive ion beams. *Nuclear Instruments and Methods in Physics Research A*, 469:254–275, 2001. → pages 26

[74] Klaus Blaum. High-accuracy mass spectrometry with stored ions. *Physics Reports*, 425(1):1–78, March 2006. → pages 26

[75] F. Herfurth. Segmented linear RFQ traps for nuclear physics. *Nuclear Instruments and Methods in Physics Research B*, 204:587–591, May 2003. → pages 26

[76] M. König, G. Bollen, and H. J. Kluge. Quadrupole excitation of stored ion motion at the true cyclotron frequency. *International Journal of Mass Spectrometry and Ion Processes*, 142:95–116, 1995. → pages 26

[77] Mathew Smith, Laura Blomeley, Paul Delheij, and Jens Dilling. First tests of the TITAN digital RFQ beam cooler and buncher. *Hyperfine Interactions*, 173(1-3):171–180, June 2007. → pages 26

[78] F. Ames, G. Bollen, and P. Delahaye. Cooling of radioactive ions with the Penning trap REXTRAP. *Nuclear Instruments and Methods in Physics Research A*, 538(1-3):17–32, February 2005. → pages 27, 28, 29

[79] G. Gabrielse, R. Kalra, W. S. Kolthammer, R. McConnell, P. Richerme, D. Grzonka, W. Oelert, T. Sefzick, M. Zielinski, D. W. Fitzakerley, M. C. George, E. a. Hessels, C. H. Storry, M. Weel, a. Müllers, and J. Walz. Trapped Antihydrogen in Its Ground State. *Physical Review Letters*, 108(11):113002, March 2012. → pages 27

[80] C. Amole, M. D. Ashkezari, M. Baquero-Ruiz, W. Bertsche, E. Butler, A. Capra, C. L. Cesar, M. Charlton, A. Deller, S. Eriksson, J. Fajans, T. Friesen, M. C. Fujiwara, D. R. Gill, A. Gutierrez, J. S. Hangst, W. N. Hardy, M. E. Hayden, C. A. Isaac, S. Jonsell, L. Kurchaninov, A. Little, N. Madsen, J. T. K. McKenna, S. Menary, S. C. Napoli, K. Olchanski, A. Olin, P. Pusa, C. O. Rasmussen, F. Robicheaux, E. Sarid, C. R. Shields, D. M. Silveira, C. So, S. Stracka, R. I. Thompson, D. P. van der Werf, J. S. Wurtele, A. Zhmoginov, and L. Friedland. Experimental and computational study of the injection of antiprotons into a positron plasma for antihydrogen production. *Physics of Plasmas*, 20(4):043510, 2013. → pages

[81] N. Kuroda et al. A source of antihydrogen for in-flight hyperfine spectroscopy. *Nature communications*, 5:3089, January 2014. → pages 27, 81

[82] D. S Hall and G. Gabrielse. Electron Cooling of Protons in a Nested Penning Trap. *Physical Review Letters*, 77(10):1962–1965, September 1996. → pages 28, 75

[83] R. G. Greaves and C. M. Surko. Antimatter plasmas and antihydrogen. *Physics of Plasmas*, 4(November 1996), 1997. → pages 28, 95

[84] V.S. Kolhinen, S. Kopecky, T. Eronen, U. Hager, J. Hakala, J. Huikari, a. Jokinen, A. Nieminen, S. Rinta-Antila, J. Szerypo, and J. Äystö. JYFLTRAP: a cylindrical Penning trap for isobaric beam purification at IGISOL. *Nuclear Instruments and Methods in Physics Research Section A: Accelerators, Spectrometers, Detectors and Associated Equipment*, 528(3):776–787, August 2004. → pages 28

[85] R. G. Greaves and C. M. Surko. Inward transport and compression of a positron plasma by a rotating electric field. *Physical Review Letters*, 85(9):1883–1886, August 2000. → pages 29, 92

[86] S. Bharadia, M. Vogel, D. M. Segal, and R. C. Thompson. Dynamics of laser-cooled Ca+ ions in a Penning trap with a rotating wall. *Applied Physics B*, 107(4):1105–1115, March 2012. → pages 29

[87] G. Gabrielse, X. Fei, L. A. Orozco, and R. L. Tjoelker. cooling and slowing of trapped antiprotons below 100 meV. *Physical Review*, 63(13):1360–1363, 1989. → pages 29, 43, 94

[88] Hiroyuki A. Torii. Production of ultra-slow antiproton beams. *AIP Conference Proceedings*, 793:293–306, 2005. → pages 29

[89] N. Beverini, V. Lagomarsino, and G. Manuzio. Stochastic cooling in Penning traps. *Physical Review A*, 38(1), 1988. → pages 30

[90] N. Beverini, V. Lagomarsino, and G. Manuzio. Stochastic cooling in multiring traps. *Hyperfine Interactions*, 44:247–255, 1989. → pages 30

[91] N. Beverini, V. Lagomarsino, G. Manuzio, F. Scuri, G. Testera, and G. Torelli. Experimental Verification of Stochastic Cooling in a Penning Trap. *Physica Scripta*, T22:238–239, January 1988. → pages 30

[92] P. J. J. Tol, Wim Hogervorst, and Wim Vassen. Theory of evaporative cooling with energy-dependent elastic scattering cross section and application to metastable helium. *Physical Review A*, 70(1):013404, July 2004. → pages 31, 32

[93] K. B. Davis, M. O. Mewes, and M. R. Andrews. Bose-Einstein Condensation in a Gas of Sodium Atoms K. *Physical Review Letters*, 75(November), 1995. → pages 31

[94] T. Kinugawa, F. J. Currell, and S. Ohtani. Pulsed evaporative cooling of ion cloud in an electron beam ion trap. *Physica Scripta*, pages 102–104, 2001. → pages 31

[95] M. Hobein, A. Solders, M. Suhonen, Y. Liu, and R. Schuch. Evaporative cooling and coherent axial oscillations of highly charged ions in a Penning trap. *Physical Review Letters*, 106(1):013002, January 2011. → pages 31, 32, 39

[96] G. B. Andresen, M. D. Ashkezari, M. Baquero-Ruiz, W. Bertsche, P. D. Bowe, E. Butler, C. L. Cesar, S. Chapman, M. Charlton, J. Fajans, T. Friesen, M. C. Fujiwara, D. R. Gill, J. S. Hangst, W. N. Hardy, R. S. Hayano, M. E. Hayden, a. Humphries, R. Hydomako, S. Jonsell, L. Kurchaninov, R. Lambo, N. Madsen, S. Menary, P. Nolan, K. Olchanski, a. Olin, a. Povilus, P. Pusa, F. Robicheaux, E. Sarid, D. M. Silveira, C. So, J. W. Storey, R. I. Thompson, D. P. van der Werf, D. Wilding, J. S. Wurtele, and Y. Yamazaki. Evaporative cooling of antiprotons to cryogenic temperatures. *Physical Review Letters*, 105(1):013003, July 2010. → pages 31

[97] A. Schliesser, R. Rivière, and G. Anetsberger. Resolved-sideband cooling of a micromechanical oscillator. *Nature Physics*, 4(5):415–419, April 2008. → pages 34, 35

[98] David J. Wineland and Wayne M. Itano. Laser cooling of atoms. *Physical Review A*, 20(4):1521, 1979. → pages 35, 36

[99] P.D. Lett, R.N. Watts, and C.I. Westbrook. Observation of Atoms Laser cooled below the doppler limit. *Physical Review Letters*, 61(2):169–173, 1988. → pages 36

[100] J. Dalibard and C. Cohen-Tannoudji. Laser cooling below the Doppler limit by polarization gradients: simple theoretical models. *JOSA B*, 6(11), 1989. → pages 36

[101] J.I. Cirac, R. Blatt, P. Zoller, and W.D. Phillips. Laser cooling of trapped ions in a standing wave. *Physical Review A*, 46(5), 1992. → pages 36, 37

[102] Yongqing Li and K. Mø lmer. Sisyphus laser cooling of trapped ions: The transition from optical molasses to the Lamb-Dicke regime. *Laser Physics*, 4(5):829–834, 1994. → pages 36, 37

[103] G. Birkl and J. A. Yeazell. Polarization gradient cooling of trapped ions. *Europhysics Letters*, 197, 1994. → pages 37

[104] K. Ravi, Seunghyun Lee, Arijit Sharma, G. Werth, and S. A. Rangwala. Cooling and stabilization by collisions in a mixed ion-atom system. *Nature communications*, 3:1126, January 2012. → pages 37

[105] Peter F. Herskind, Aurélien Dantan, Joan P. Marler, Magnus Albert, and Michael Drewsen. Realization of collective strong coupling with ion Coulomb crystals in an optical cavity. *Nature Physics*, 5(7):494–498, June 2009. → pages 37

[106] Zunjian Ke, W Shi, G Gwinner, K Sharma, S Toews, J Dilling, VL Ryjkov, TITAN Collaboration, et al. A cooler ion trap for the titan on-line trapping facility at triumf. *Hyperfine Interactions*, 173(1-3):103–111, 2006. → pages 38

[107] Zunjian Ke. *A cooler ion trap for the TITAN on-line trapping facility at TRIUMF*. PhD thesis, University of Manitoba, 2008. → pages 38, 43

[108] J. R. Danielson, T. R. Weber, and C. M. Surko. Plasma manipulation techniques for positron storage in a multicell trap. *Physics of Plasmas*, 13(12):123502, 2006. → pages 39

[109] J. H. Malmberg and C. F. Driscoll. Long time containment of a pure electron plasma. *Physical Review Letters*, 1980. → pages 39

[110] N. Oshima, M. Niigaki, M. Lebois, a. Mohri, K. Komaki, and Y. Yamazaki. Simultaneous cooling of highly charged ions with electrons and positrons. *Nuclear Instruments and Methods in Physics Research Section B: Beam Interactions with Materials and Atoms*, 235(1-4):504–508, July 2005. → pages 39

[111] Lukas Gruber, Joe P Holder, and Dieter Schneider. Formation of Strongly Coupled Plasmas from Multi Component Ions in a Penning Trap. *Physica scripta*, 60:60–107, 2005. → pages 39

[112] J. Bernard, J. Alonso, T. Beier, M. Block, S. Djekić, H.-J. Kluge, C. Kozhuharov, W. Quint, S. Stahl, T. Valenzuela, J. Verdú, M. Vogel, and G. Werth. Electron and positron cooling of highly charged ions in a cooler Penning trap. *Nuclear Instruments and Methods in Physics Research Section A: Accelerators, Spectrometers, Detectors and Associated Equipment*, 532(1-2):224–228, October 2004. → pages 40

[113] B. Möllers, C. Toepffer, M. Walter, G. Zwicknagel, C. Carli, and H. Nersisyan. Cooling of ions and antiprotons with magnetized electrons. *Nuclear Instruments and Methods in Physics Research Section A: Accelerators, Spectrometers, Detectors and Associated Equipment*, 532(1-2):279–284, October 2004. → pages 41

[114] C. Toepffer H. Nersisyan and G. Zwicknagel. *Interactions Between Charged Particles in a Magnetic Field*. Springer, Heidelberg, 2007. → pages 40

[115] Z. Ke, W. Shi, G. Gwinner, K. Sharma, S. Toews, J. Dilling, and V. L. Ryjkov. A cooler ion trap for the TITAN on-line trapping facility at TRIUMF. *Hyperfine Interactions*, 173(1-3):103–111, June 2007. → pages 40, 41, 42

[116] Spitzer L. *Physics of Fully Ionized Gases*. Interscience Publishers, New York, 1956. → pages 41

[117] D. J. Berkeland, J. D. Miller, J. C. Bergquist, W. M. Itano, and D. J. Wineland. Minimization of ion micromotion in a Paul trap. *Journal of Applied Physics*, 83(10):5025, 1998. → pages 43

[118] B. E. Schultz et al. Cooling of highly-charged, short-lived ions for precision mass spectrometry at TRIUMF's Ion Trap for Atomic and Nuclear Science. *Physica Scripta*, T156:014097, September 2013. → pages 43

[119] U. Chowdhury et al. A Cooler Penning Trap to cool highly charged and short-lived isotopes at TITAN. *accelconf.web.cern.ch*, pages 206–209, 2013. → pages 43, 47, 94

[120] C. F. Driscoll and J. H. Malmberg. Length-Dependent containment of a pure electron Plasma column. *Physical Review Letters*, 167(January), 1983. → pages 44, 71, 95

[121] C. M. Surko and R. G. Greaves. A multicell trap to confine large numbers of positrons. *Radiation Physics and Chemistry*, 68:419–425, 2003. → pages 44, 95

[122] T. Mohamed, A. Mohri, and Y. Yamazaki. Comparison of non-neutral electron plasma confinement in harmonic and rectangular potentials in a very dense regime. *Physics of Plasmas (1994)*, 20(1):0–6, 2013. → pages 44, 56, 57, 75, 88, 90, 97

[123] J. Repp. *Setup of a non-destructive ion detection system and magnetic field investigations for precision mass measurements at TRIGA-TRAP*. PhD thesis, Johannes Gutenberg-University at Mainz, 2008. → pages 44, 47

[124] Anna A. Kwiatkowski. *High Precision Mass Measurement of Si-32 and Developments at the LEBIT Facility*. PhD thesis, Michigan State University, 2011. → pages 47

[125] C. Benvenuti and P. Chiggiato. Vacuum properties of TiZrV non-evaporable getter films. *Vacuum*, 60:57–65, 2001. → pages 48, 49, 51, 52

[126] Aerospace Fabrication, http://www.aerospacefab.com. → pages 50

[127] Cryomagnetics, http://www.cryomagnetics.com. → pages 50

[128] Edward H. Chao, Ronald C. Davidson, Stephen F. Paul, and Kyle A. Morrison. Effects of background gas pressure on the dynamics of a nonneutral electron plasma confined in a MalmbergPenning trap. *Physics of Plasmas*, 7(3):831, March 2000. → pages 57, 71

[129] J. R. Danielson and C. M. Surko. Radial compression and torque-balanced steady states of single-component plasmas in Penning-Malmberg traps. *Physics of Plasmas*, 13(5):055706, 2006. → pages 57

[130] Robert T. McIver. Trajectory calculations for axial injection of ions into a magnetic field: overcoming the magnetic mirror effect with an r.f. quadrupole lens. *International Journal of Mass Spectrometry and Ion Processes*, 98(1):35–50, 1990. → pages 59, 98

[131] Matthew Redshaw, Anne L. Benjamin, Georg Bollen, Rafael Ferrer, David L. Lincoln, Ryan Ringle, Stefan Schwarz, and Adrian a. Valverde. Fabrication and characterization of field emission points for ion production in Penning trap applications. *International Journal of Mass Spectrometry*, pages 1–7, 2015. → pages 60, 61, 62

[132] M. Amoretti et al. Complete nondestructive diagnostic of nonneutral plasmas based on the detection of electrostatic modes. *Physics of Plasmas*, 10(8):3056, 2003. → pages 68, 99

[133] R. H. Levy. Diocotron Instability in a Cylindrical Geometry. *Physics of Fluids*, 8(7):1288, 1965. → pages 71, 76, 95

[134] J. J. Bollinger. Non-neutral ion plasmas and crystals, laser cooling, and atomic clocks. *Physics of Plasmas*, 1(May 2003):1403–1414, 1994. → pages 71, 95

[135] Vladimir Gorgadze, Thomas A. Pasquini, Joel Fajans, and Jonathan S. Wurtele. Injection into electron plasma traps. *Report from Lawrence Berkeley National Laboratory*, 2003. → pages 71, 92, 95

[136] G. Bettega, F. Cavaliere, M. Cavenago, A. Illiberi, R. Pozzoli, and M. Romé. Experimental investigation of the ion resonance instability in a trapped electron plasma. *Plasma Physics and Controlled Fusion*, 47(10):1697–1708, October 2005. → pages 71

[137] G. Maero, B. Paroli, R. Pozzoli, and M. Rome. Stabilizing effect of a nonresonant radio frequency drive on the m=1 diocotron instability. *Physics of Plasmas*, 18(3):032101, 2011. → pages 71, 96

[138] C. Amole et al. In situ electromagnetic field diagnostics with an electron plasma in a Penning-Malmberg trap. *New Journal of Physics*, 16(1):013037, January 2014. → pages 75, 94

[139] B. Paroli, F. De Luca, G. Maero, R. Pozzoli, and M. Romé. Broadband radio frequency plasma generation in a PenningMalmberg trap. *Plasma Sources Science and Technology*, 19(4):045013, August 2010. → pages 75, 84, 96

[140] M. Hori and J. Walz. Physics at CERNs Antiproton Decelerator. *Progress in Particle and Nuclear Physics*, 72:206–253, September 2013. → pages 81

[141] B. R. Beck, J. Fajans, and J. H. Malmberg. Measurement of Collisional Anistropic Temperature Relaxation in a Strongly Magnetized Pure Electron Plasma. *Physical Review Letters*, 1992. → pages 82

[142] B. R. Beck, J. Fajans, and J. H. Malmberg. Temperature and anisotropic-temperature relaxation measurements in cold, pure-electron plasmas. *Physics of Plasmas*, 3(4):1250, 1996. → pages 82

[143] Kuroda Naofumi. *Accumulation of a large number of antiprotons and production of an ultra-slow antiproton beam*. PhD thesis, University of Tokyo, 2003. → pages 82

[144] A. Mohri, H. Higaki, and H. Tanaka. Confinement of nonneutral spheroidal plasmas in Multi-ring electrode traps. *Japan Journal of Applied physics*, 37(2):664–670, 1998. → pages 82

[145] T. Mohamed, H. Imao, N. Oshima, A. Mohri, and Y. Yamazaki. Fast electron accumulation and its mechanism in a harmonic trap under ultrahigh vacuum conditions. *Physics of Plasmas*, 18(3):032507, 2011. → pages 83, 92

[146] Tarek Mohamed. Successful production of non-neutral electron plasma of high density in the multi-ring trap. *Plasma Devices and Operations*, 16(3):181–188, September 2008. → pages 86

[147] J. J. Bollinger, D. J. Heinzen, and F. L. Moore. Electrostatic modes of ion-trap plasmas. *Physical Review A*, 48(1), 1993. → pages 91, 94, 95

[148] L. Gruber, J. P. Holder, J. Steiger, B. R. Beck, H. E. DeWitt, J. Glassman, J. W. McDonald, D. A. Church, and D. Schneider. Evidence for highly charged ion Coulomb crystallization in multicomponent strongly coupled plasmas. *Physical Review Letters*, 86:636–639, 2001. → pages 91

[149] D. H. E. Dubin. Theory of Electrostatic Fluid Modes in a Cold Spheroidal Non-Neutral Plasma. *Physical Review Letters*, 66(16):2076–2079, 1991. → pages 92, 98

[150] R. G. Greaves, M. D. Tinkle, and C. M. Surko. Modes of a pure ion plasma at the Brillouin limit. *Physical Review Letters*, 74(1):90–93, January 1995. → pages

[151] E. Yu. Backhaus, J. Fajans, and J. S. Wurtele. Stability of highly asymmetric non-neutral plasmas. *Physics of Plasmas*, 6(1):19, 1999. → pages 92

[152] Ross L. Spencer and S. Neil Rasband. Damped diocotron quasi-modes of non-neutral plasmas and inviscid fluids. *Physics of Plasmas*, 4(1):53, 1997. → pages 93

[153] M. D. Tinkle, R. G. Greaves, and C. M. Surko. Low-order longitudinal modes of single-component plasmas. *Physics of Plasmas*, 2(8):2880, 1995. → pages 94, 98

[154] M. D. Tinkle, R. G. Greaves, and C. M. Surko. Modes of spheroidal ion plasmas at the Brillouin limit. *Physics of Plasmas*, 3(October 1995):749–758, 1996. → pages 94, 95

[155] D. L. Eggleston and T. M. O'Neil. Theory of asymmetry-induced transport in a non-neutral plasma. *Physics of Plasmas*, 6(7):2699, 1999. → pages 94

[156] G. A. Roberts and N. Rostoker. Magnetic damping of l=1 diocotron mode. *Physics of Fluids*, 28(8):2547, August 1985. → pages 94, 96, 97, 98, 101

[157] R. J. Briggs, J. D. Daugherty, and R. H. Levy. Role of Landau damping in crossed-field electron beams and inviscid shear flow. *Physics of fluids*, 421(1970), 1970. → pages 95, 96

[158] D. L. Eggleston, C. F. Driscoll, B. R. Beck, A. W. Hyatt, and J. H. Malmberg. Parallel energy analyzer for pure electron plasma devices. *Physics of Fluids B: Plasma Physics*, 4(10):3432, 1992. → pages 95

[159] J. Fajans, E. Gilson, and L. Friedland. Autoresonant (Nonstationary) Excitation of the Diocotron Mode in Non-neutral Plasmas. *Physical Review Letters*, 82(22):4444–4447, May 1999. → pages 95

[160] Nicholas A. Krall, Alvin W. Trivelpiece, and Robert A. Gross. Principles of plasma physics. *American Journal of Physics*, 41(12):1380–1381, 1973. → pages 95

[161] Mark David Tinkle. *Electronstatic Oscillations of Spheroidal Single-Component Plasmas*. PhD thesis, University of California, San Diego, 1994. → pages 95

[162] G. Bettega. Diocotron Instability in ELTRAP. *AIP Conference Proceedings*, 692:50–54, 2003. → pages 95

[163] Hiroyuki Higaki and Akihiro Mohri. Experiment on diocotron oscillations of spheroidal non-neutral electron plasmas in a multi-ring-electrode trap. *Physics Letters A*, 235(5):504–507, 1997. → pages 95

[164] C. M. Surko and R. G. Greaves. Emerging science and technology of antimatter plasmas and trap-based beams. *Physics of Plasmas*, 11(5):2333, 2004. → pages 95

[165] N. C. Hurst, J. R. Danielson, C. J. Baker, and C. M. Surko. Electron Plasma Orbits from Competing Diocotron Drifts. *Physical Review Letters*, 113(2):025004, July 2014. → pages 95

[166] W. D. White, J. H. Malmberg, and C. F. Driscoll. Resistive-wall destabilization of diocotron waves. *Physical Review Letters*, 49(25), 1982. → pages 96

[167] S. M. Crooks and T. M. ONeil. Rotational pumping and damping of the m= 1 diocotron mode. *Physics of Plasmas (1994-present)*, 2(2):355–364, 1995. → pages 96

[168] B. P. Cluggish and C. F. Driscoll. Transport and Damping from Rotational Pumping in Magnetized Electron Plasmas. *Physical Review Letters*, 74(21):4213–4216, 1995. → pages 96

[169] J. P. Marler and M. R. Stoneking. Confinement Time Exceeding One Second for a Toroidal Electron Plasma. *Physical Review Letters*, 100(15):155001, April 2008. → pages 96

[170] S. M. Crooks and T. M. O'Neil. Transport in a toroidally confined pure electron plasma. *Physics of Plasmas*, 3(7):2533, 1996. → pages 96

[171] Eli Sarid, Erik Gilson, and Joel Fajans. Decay of the Diocotron Rotation and Transport in a New Low-Density Asymmetry-Dominated Regime. *Physical Review Letters*, 89(10):105002, August 2002. → pages 96, 97

[172] Francis F. Chen and A. W. Trivelpiece. Introduction to plasma physics. *Physics Today*, 29:54, 1976. → pages 98

[173] R. K. Wallace and S. E. Woosley. Explosive hydrogen burning. *The Astrophysical Journal Supplement Series*, 45:389–420, 1981. → pages 104, 105

[174] P. Murdin and L. Murdin. *Supernovae*. Cambridge University Press, 1985. → pages 104

[175] Walter H. G. Lewin, J. Van Paradijs, and Ronald E. Taam. X-Ray bursts. *Space Science Reviews*, 62:223–389, 1993. → pages 104

[176] E. Margaret Burbidge, G. R. Burbidge, William a. Fowler, and F. Hoyle. Synthesis of the elements in stars. *Reviews of Modern Physics*, 29(4):547–650, 1957. → pages 104

[177] F. K. Thielemann and F. Brachwitz. Element Synthesis in Stars. *Progress in Particle and Nuclear Physics*, 46:5–22, 2001. → pages 105

[178] C. Iliadis and P. M. Endt. Explosive hydrogen burning of ^{27}Si, ^{31}S, ^{35}Ar, and ^{39}Ca in novae and x-ray bursts. *The Astrophysical Journal*, 10:434–453, 1999. → pages 105, 106

[179] H. Herndl et al. Thermonuclear reaction rate of ^{23}Mg$(p,\gamma)^{24}$Al. *Physical Review C*, 58(3):1798–1803, 1998. → pages 105, 107

[180] O. Straniero et al. impact of a revised ^{25}Mg(p , γ) ^{26}Al reaction rate on the operation of the Mg-Al cycle. *The Astrophysical Journal*, 763(2):100, February 2013. → pages 105, 106

[181] D. Visser, C. Wrede, J. Caggiano, J. Clark, C. Deibel, R. Lewis, A. Parikh, and P. Parker. Measurement of ^{23}Mg(p,γ)^{24}Al resonance energies. *Physical Review C*, 76(6):065803, December 2007. → pages 105, 107

[182] Christian Iliadis and Art Champagne. The effects of thermonuclear reaction-rate variations on nova nucleosynthesis: A sensitivity study. *The Astrophysical Journal. Supplement Series*, pages 105–137, 2002. → pages 105

[183] G. Lotay, P. Woods, D. Seweryniak, M. Carpenter, N. Hoteling, R. Janssens, D. Jenkins, T. Lauritsen, C. Lister, A. Robinson, and S. Zhu. First in-beam γ-ray spectroscopy study of ^{24}Al and its implications for the astrophysical ^{23}Mg(p,γ)^{24}Al reaction rate in ONe novae. *Physical Review C*, 77(4):042802, April 2008. → pages 105, 107, 115, 116

[184] S. Kubono and T. Kajino. Structure of ^{24}Al for the stellar reaction rate of ^{23}Mg$(p,\gamma)^{24}$Al. *Nuclear physics A*, 588:521–536, 1995. → pages 105

[185] M. Wiescher et al. The proton capture reactions on ^{21}Na and ^{22}Na under hydrogen burning conditions. *Zeitschrift für Physik A Atomic Nuclei*, 315:309–315, 1986. → pages 106

[186] L. Erikson, C. Ruiz, F. Ames, P. Bricault, L. Buchmann, A. A. Chen, J. Chen, H. Dare, B. Davids, C. Davis, C. M. Deibel, M. Dombsky, S. Foubister, N. Galinski, U. Greife, U. Hager, A. Hussein, D. A. Hutcheon, J. Lassen, L. Martin, D. F. Ottewell, C. V. Ouellet, G. Ruprecht, K. Setoodehnia, A. C. Shotter, A. Teigelhöfer, C. Vockenhuber, C. Wrede, and A. Wallner. First direct measurement of the ^{23}Mg(p,γ)^{24}Al reaction. *Physical Review C*, 81(4):045808, April 2010. → pages 107, 108, 114, 116

[187] C. Wrede, J. A. Clark, C. M. Deibel, T. Faestermann, R. Hertenberger, A. Parikh, H. Wirth, S. Bishop, A. A. Chen, K. Eppinger, B. M. Freeman, R. Krücken, O. Lepyoshkina, G. Rugel, and K. Setoodehnia. Properties of ^{20}Na, ^{24}Al, ^{28}P, ^{32}Cl, and ^{36}K for studies of explosive hydrogen burning. *Physical Review. C*, 035805:1–8, 2010. → pages 107, 114

[188] M. Wang et al. The Ame2012 atomic mass evaluation. *Chinese Physics C*, 36 (12):1603–2014, 2012. → pages 107, 113, 114, 115, 119

[189] G. Audi, A.H. Wapstra, and C. Thibault. The Ame2003 atomic mass evaluation. *Nuclear Physics A*, 729(1):337–676, December 2003. → pages 107

[190] C. Wrede, J. A. Clark, C. M. Deibel, T. Faestermann, R. Hertenberger, A. Parikh, H. Wirth, S. Bishop, A. A. Chen, K. Eppinger, A. Garcia, and R. Krücken. Toward precise Q_{EC} values for the superallowed $0^+ \rightarrow 0^+$ β decays of T= 2 nuclides: The masses of ^{20}Na, ^{24}Al, ^{28}P, and ^{32}Cl. *Physical Review C*, 81:1–9, 2010. → pages 108, 109

[191] I. S. Towner and J. C. Hardy. Improved calculation of the isospin-symmetry-breaking corrections to superallowed Fermi β decay. *Physical Review C*, 025501(2):1–15, February 2008. → pages 108, 110

[192] S. Eidelman et al. Review of Particle Physics. *Physics Letters B*, 592(1-4):1–5, July 2004. → pages 108

[193] I. S. Towner and J. C. Hardy. The evaluation of V_{ud} and its impact on the unitarity of the Cabibbo-Kobayashi-Maskawa quark-mixing matrix. *Reports on Progress in Physics*, 73(4):046301, April 2010. → pages 108

[194] John C. Hardy et al. CKM unitarity normalization tests, present and future. *Annalen der Physik*, 525(7):443–451, July 2013. → pages 108

[195] Dan Melconian. Nuclear β-decay measurements and V_{ud}. In *Proceedings of CKM2010, the 6th International Workshop on the CKM Unitarity Triangle*, 2011. → pages 109, 110

[196] J. Hardy and I. Towner. Superallowed $0^+ \rightarrow 0^+$ nuclear β decays: A new survey with precision tests of the conserved vector current hypothesis and the standard model. *Physical Review C*, 79(5):055502, May 2009. → pages 109

[197] M. Bhattacharya, D. Melconian, A. Komives, S. Triambak, A. García, E. G. Adelberger, B. A. Brown, M. W. Cooper, T. Glasmacher, V. Guimaraes, P. F. Mantica, A. M. Oros-Peusquens, J. I. Prisciandaro, M. Steiner, H. E. Swanson, S. L. Tabor, and M. Wiedeking. f_t value of the $0^+ \to 0^+$ β^+-decay of ^{32}Ar: A measurement of isospin symmetry breaking in a superallowed decay. *Physical Review C*, 77(6):065503, June 2008. → pages 110

[198] M. Mehlman et al. Design of a unique open-geometry cylindrical Penning trap. *Nuclear Instruments and Methods in Physics Research Section A: Accelerators, Spectrometers, Detectors and Associated Equipment*, 712:9–14, June 2013. → pages 110

[199] G. A. Miller and A. Schwenk. Isospin-symmetry-breaking corrections to superallowed Fermi β decay: Radial excitations. *Physical Review C*, 80(6):064319, December 2009. → pages 110

[200] W. Satuła, J. Dobaczewski, Witold Nazarewicz, and T. R. Werner. Isospin-breaking corrections to superallowed fermi β decay in isospin-and angular-momentum-projected nuclear density functional theory. *Physical Review C*, 86(5):054316, 2012. → pages 110

[201] S. Profumo et al. Supersymmetric contributions to weak decay correlation coefficients. *Physical Review D*, 75(7):075017, April 2007. → pages 110

[202] M. A. B. Beg et al. Manifest left-right symmetry and its experimental consequences. *Physical Review Letters*, 38(22):1252–1255, 1977. → pages 110

[203] P. Herczeg. Beta Decay Beyond the Standard Model. *Progress in Particle and Nuclear Physics*, 6410(01), 2001. → pages 110

[204] Nathal Severijns, Marcus Beck, and Oscar Naviliat-Cuncic. Tests of the standard electroweak model in nuclear beta decay. *Reviews of Modern Physics*, 78(3):991–1040, September 2006. → pages 110

[205] A. Kellerbauer, G. Audi, D. Beck, K. Blaum, G. Bollen, C. Guénaut, F. Herfurth, A. Herlert, H.-J. Kluge, D. Lunney, S. Schwarz, L. Schweikhard, C. Weber, and C. Yazidjian. High-precision masses of neutron-deficient rubidium isotopes using a Penning trap mass spectrometer. *Physical Review C*, 76(4):045504, October 2007. → pages 111, 112

[206] A. T. Gallant et al. Highly charged ions in Penning traps: A new tool for resolving low-lying isomeric states. *Physical Review C*, 85(4):044311, April 2012. → pages 112

[207] A. Chaudhuri et al. TITAN: an ion trap for accurate mass measurements of ms-half-life nuclides. *Applied Physics B*, 114(1-2):99–105, August 2013. → pages 112

[208] Alan Shotter. Advances at ISOL facilities. *Nuclear Instruments and Methods in Physics Research, Section B: Beam Interactions with Materials and Atoms*, 204:17–19, 2003. → pages 112

[209] N. R. Daly. Scintillation type mass spectrometer ion detector. *Review of Scientific Instruments*, 31(3):264–267, 1960. → pages 113

[210] Manfred Löffler, H. J. Scheerer, and Herbert Vonach. The ion optical properties of the munich q3d-spectrograph investigated by means of a special experimental ray tracing method. *Nuclear Instruments and Methods*, 111(1):1–12, 1973. → pages 114

[211] D. A. Hutcheon, C. Ruiz, J. Fallis, J. M. D'Auria, B. Davids, U. Hager, L. Martin, D. F. Ottewell, S. Reeve, and A. Rojas. Measurement of radiative capture resonance energies with an extended gas target. *Nuclear Instruments and Methods in Physics Research Section A: Accelerators, Spectrometers, Detectors and Associated Equipment*, 689:70–74, 2012. → pages 116

Appendix A

Standard tune for CPET

For any given test, CPET tunes were found to be highly reproducible. The day-to-day shift of the tune was insignificant. In this appendix we provide the basic tunes for CPET operations.

A.1 Potential setting

In the following figure CPET's beamline optics are shown.

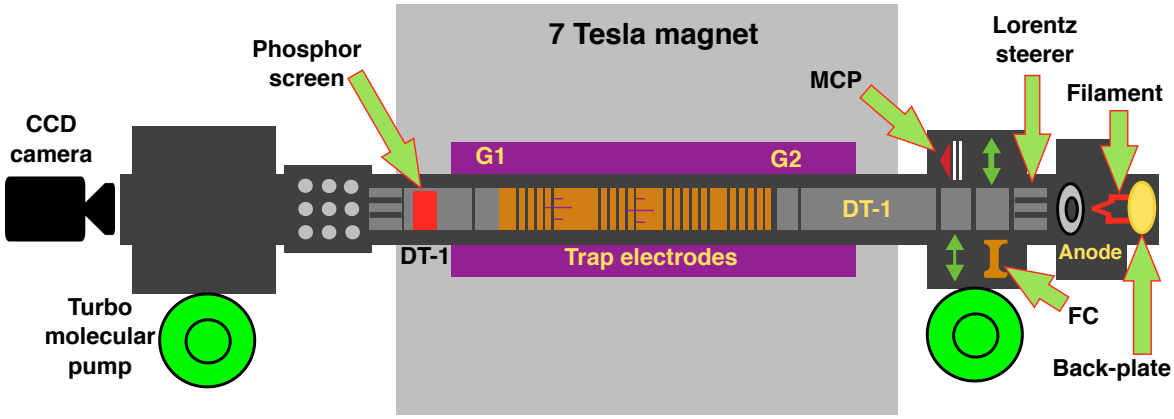

Figure A.1: CPET beamline. Elements on the left of phosphor screens are not used as we need elements only up to the phosphor screen for plasma loading, trapping and detection cycles.

The table summarizes the tune and a range of potentials applied to the CPET optics which provide good test results and are also very highly reproducible.

Table A.1: CPET tune values. The negative values are highlighted with green and the positives with red.

Electrode		Range of applied potential		Best values for plasma studies	Function
		Minimum (V)	Maximum (V)		
Electron source back-plate		-1400	-1400	-1400	Electron beam tune
Electron source float		-1400	-1400	-1400	Electron beam energy control
Anode		-1349	-1349	-1349	Electron extraction potential
Filament bias		4.1	5	4.2 to 4.96	Bias to generate electron
Lorentz-Steerer	+Y	+400	+1000	+800	Electron beam steering and focusing
	-Y, +X, -X	-200	-1000	+400	
MCP/MCP -DT		+200	+400	+380	Electron beam focusing
FC/FC-DT		+200	+500	+275	Electron beam focusing
Drift tube-2		+200	+600	+380	Electron beam focusing
Gate-2	High	-400	-1399	-2100	Electron beam focusing, loading, and trapping of electron
	Low	-2100	-2100	-800	
Trap		-180	-1399	-200 to -800	Trap bias
Gate-1	High	0	+200	+100	Electron beam focusing, loading, trapping, and extraction of plasma
	Low	-2100	-2100	-2100	
Drift tube-1		+100	+5000	+3100	Plasma focusing
Phosphor screen		0	+5000	+200 to +3500	Plasma detection

A.2 Programmable Pulse Generator (PPG) setting

The timing sequence for the PPG is shown in Fig. (A.2). For the electron plasma loading, trapping and extraction cycle, a simple setting of three PPG signals is sufficient. One TTL signal controls the loading of the electron. A second signal controls the extraction and a third is used to trigger the CCD camera for the plasma image. A more complex PPG configuration is required to trap the plasma for longer than 40 seconds.

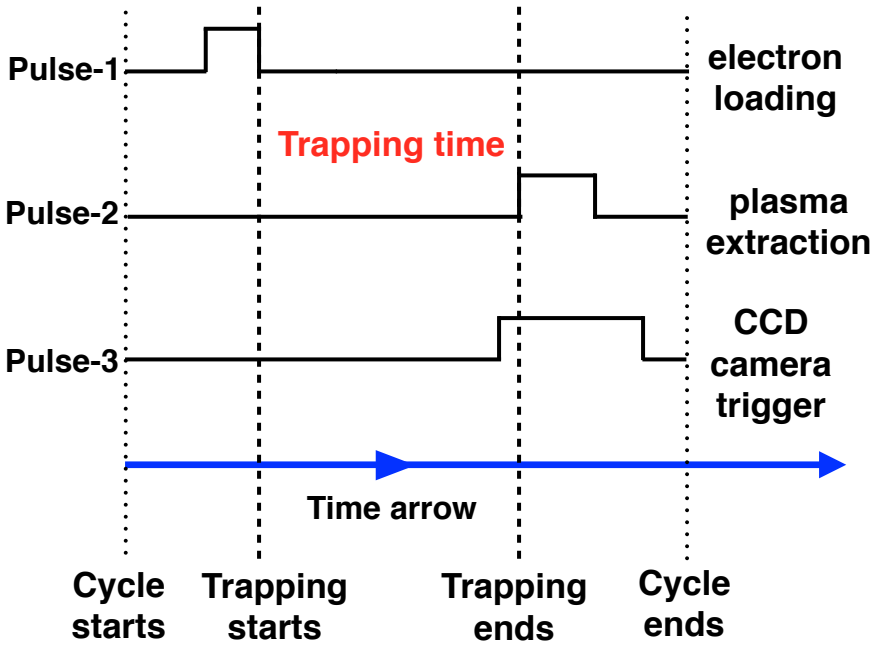

Figure A.2: PPG setting for CPET.

Table (A.2) summarizes the PPG pulse details.

Table A.2: Programmable Pulse Generator (PPG) setting details. At present, three major components are controlled by the PPG for precision timing.

Pulse number	device controlled	pulse delay	pulse width (ms)
1	electron loading gate	0	300
2	electron extraction gate	trapping time+loading time	10
3	CCD camera	trapping time+loading time	2

A.3 Camera setting

The tune of the CCD camera was optimized to reduce the background and enhance the plasma image. The following image shows the best tune for plasma detection.

The software FlyCapture2 (version 2.6.3.4) captures and saves individual frames to a PC.

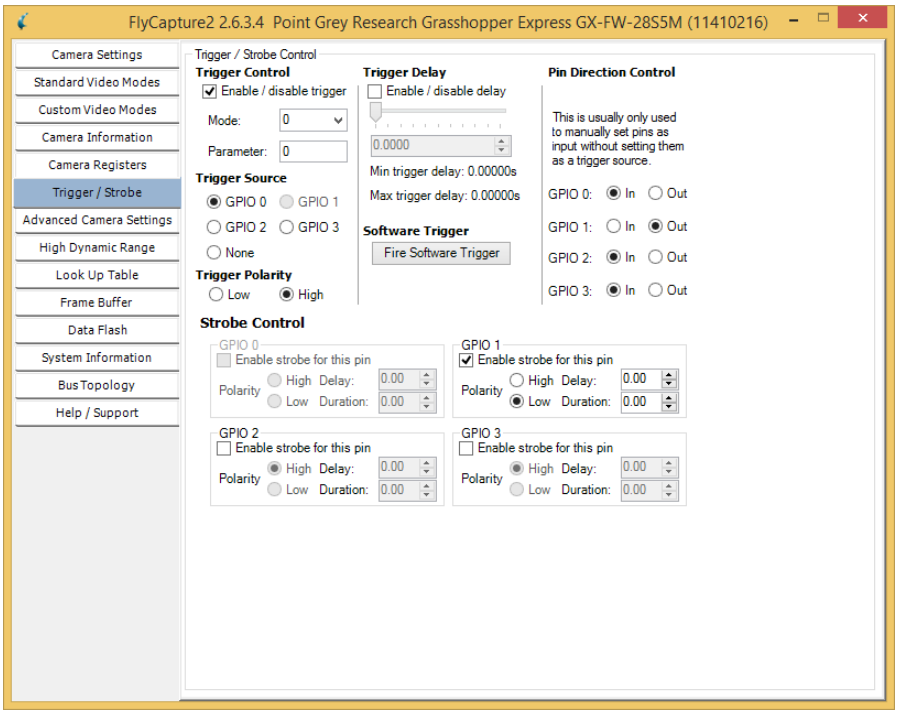

(a) Trigger setting for best image quality.

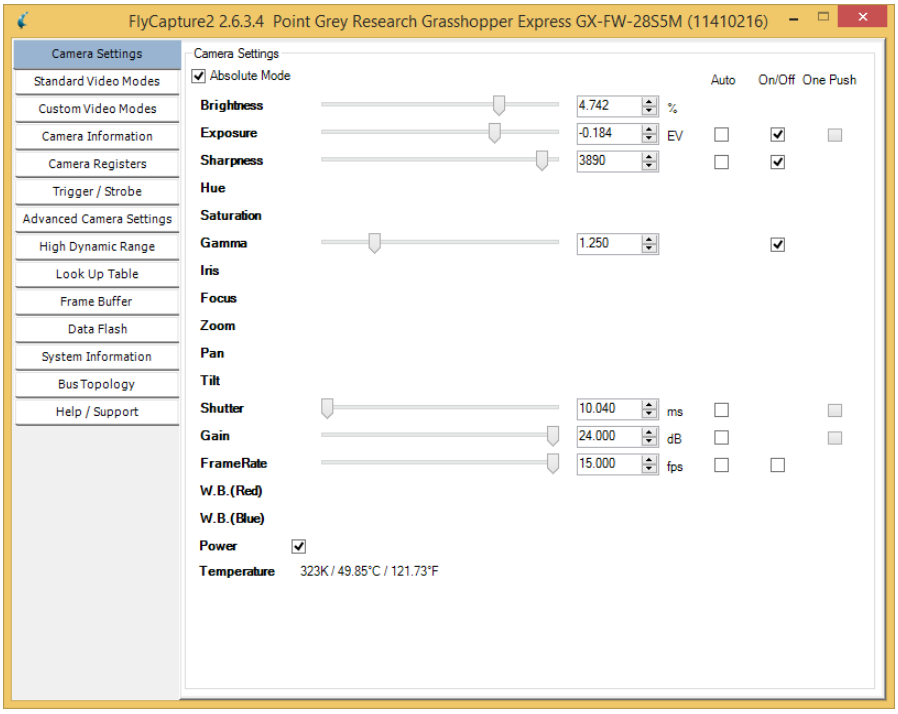

(b) Other settings for CCD.

Figure A.3: CCD camera trigger and other settings for optimal image quality for recording electron plasma spots.